Charge Radii of Zn and Ni Isotopes Measured by Collinear Laser Spectroscopy

A thesis submitted to the University of Manchester for the degree
of Doctor of Philosophy in the Faculty of Science and Engineering

2018

Liang Xie

School of Physics and Astronomy
University of Manchester

The remainder of this page was intentionally left blank.

Contents

The remainder of this page was intentionally left blank.

List of Figures

List of Tables

The remainder of this page was intentionally left blank.

Abstract

The hyperfine structures and isotopes shifts have been measured for isotope chains of zinc (Z=30) and nickel (Z=28) using collinear laser spectroscopy on atom beams provided by the on-line isotope separator facility, ISOLDE, at CERN.

The isotopes $^{62-80}$Zn were measured on the 481 nm transition from a metastable $^3P_2$ state at 32,890.35 cm^{-1} to a $^3S_1$ state at 53,672.28 cm^{-1}. One isomer was also observed for each of the odd isotopes $^{69-79}$Zn.

The ground states of $^{58-68,70}$Ni where measured on the 352 nm transition from a metastable $^3D_3$ state at 204.79 cm^{-1} to a $^3P_2$ state at 28,569.20 cm^{-1}.

The mean square charge radii of these Zn and Ni isotopes were deduced using atomic factors extracted from King plots. The results, together with previous data of Cu (Z=29) and Ga (Z=31), depict the evolution of the debated N=40 sub-shell as the proton number moves away from the Z=28 closed shell. Effects of the proton occupation number of orbitals above Z=28 and nuclear deformation were also explored on the Zn isotopes showing the charge radii of nuclei are determined by various factors in a complicated combination.

The remainder of this page was intentionally left blank.

Declaration of Authorship

I, Liang Xie, confirm that no portion of the work referred to in the thesis has been submitted in support of an application for another degree or qualification of this or any other university or other institute of learning.

The remainder of this page was intentionally left blank.

Copyright Statement

i. The author of this thesis (including any appendices and/or schedules to this thesis) owns certain copyright or related rights in it (the “Copyright”) and s/he has given The University of Manchester certain rights to use such Copyright, including for administrative purposes.

ii. Copies of this thesis, either in full or in extracts and whether in hard or electronic copy, may be made **only** in accordance with the Copyright, Designs and Patents Act 1988 (as amended) and regulations issued under it or, where appropriate, in accordance with licensing agreements which the University has from time to time. This page must form part of any such copies made.

iii. The ownership of certain Copyright, patents, designs, trade marks and other intellectual property (the “Intellectual Property”) and any reproductions of copyright works in the thesis, for example graphs and tables (“Reproductions”), which may be described in this thesis, may not be owned by the author and may be owned by third parties. Such Intellectual Property and Reproductions cannot and must not be made available for use without the prior written permission of the owner(s) of the relevant Intellectual Property and/or Reproductions.

iv. Further information on the conditions under which disclosure, publication and commercialisation of this thesis, the Copyright and any Intellectual Property and/or Reproductions described in it may take place is available in the University IP Policy (see `http://documents.manchester.ac.uk/DocuInfo.aspx?DocID=24420`), in any relevant Thesis restriction declarations deposited in the University Library, The University Library’s regulations (see `http://www.library.manchester.ac.uk/about/regulations/`) and in The University’s policy on Presentation of Theses

The remainder of this page was intentionally left blank.

Acknowledgements

Throughout my PhD study, I have been incredibly fortunate to work with many wonderful people who offered me great support. Firstly I'd like to send my particular gratitude to my supervisor Jon as the teaching received from him is far beyond just knowledge itself.

I am very grateful to all the ISOLDE Staff and Users for their hard work ensuring the success of the experiments. It was a great pleasure to receive the training from Mark, my co-supervisor. Also many thanks to Xiaofei who often kindly share her knowledge and experience. It is such a precious memory working with everyone in the COLLAPS collaboration group.

At the end, I want to express the appreciation to my family - my dear wife, parents and grandparents for the support and sacrifice they made.

The remainder of this page was intentionally left blank.

Chapter 1

Introduction

The hyperfine structure of an atomic transition was first discovered by Michelson in 1892 [1]. The phenomenon was interpreted by Pauli [2] as the result of different couplings between the spin of the nucleus and the total angular moment of the outer electrons. The theoretical description of the splittings on spectral lines was firmly shaped in the paper by Hermann Schüler [3] in 1931. Now the study of atomic hyperfine structures is a recognised method to measure nuclear moments.

The isotope shift is the shift in the energy of a spectral line between two different isotopes. It was first discovered in 1912 by A. Russell and R. Rossi [4]. The first theoretical explanation was proposed by Bohr as the differences in the nuclear recoil kinetic energy due to the different nuclear masses [5]. The discrepancy between this theory and experimental measurement [6] was later explained by the contribution of the nuclear charge distribution [7]. Now the two effects are known as the mass shift and the field shift. Although nuclear charge radii of stable isotopes can be measured by electron scattering and muonic x-ray energies, the isotope shift measurement is the only method available to study charge radii of radioactive nuclei.

The collinear laser spectroscopy method is used in this thesis to study isotopes of zinc and nickel. In this method accelerated atom beams are resonantly excited by a collinearly-overlapped laser [8, 9]. The work was carried out at the on-line radioactive ion beam facility at ISOLDE, CERN where the beams available enabled the study to be extended far from the valley of stability. The Doppler broadening due to the thermal motion of the atoms in the direction of the laser beam can be compressed to a tolerable level by the acceleration of the ion beam. The thermal energy spread from the ion source δE determines the velocity spread, δv:

$$\delta E = mv\delta v$$

where m is the mass and v the velocity of the ion. Since δE is constant in the acceleration process, the increase of v reduces δv and hence the Doppler broadening. The collinear geometry also ensures a high fluorescence efficiency of the method due to the very high spatial overlap between the atomic sample and the laser beam. Because the experiment measured the atomic transitions (for both zinc and nickel), the ion beams were neutralised by sodium vapour in a charge exchange cell (CEC) prior to the resonant excitation region.

This thesis describes collinear laser spectroscopy measurements on Zn and Ni isotopic chains. In Chapter 2 the physics theory of isotope shifts and hyperfine structures is presented. Chapter 3 describes the general experimental details of the ISOLDE facility and the laser systems used. Chapters 4 and 5 describe the measurements and data analysis of zinc isotopes and nickel isotopes respectively. Chapter 6 discusses the results in terms of the nuclear structure and suggests some future work.

Some of the results from these experiments have been published. The zinc magnetic and quadrupole moments were the subject of a PhD thesis of Calvin Wraith (Liverpool) and have been published [10]. Two papers reported interesting shape properties of isomers in ^{73}Zn [11] and ^{79}Zn [12]. The charge radii results for zinc reported here have been prepared for publication.

Chapter 2

Physics Theory

In the simplest picture of atomic structure, the nucleus is treated as a point with a charge of $+Ze$. The electron energy levels can be well predicted using the electric field generated by the point charge. A finite size and any internal structure of the nucleus could cause a shift to the atomic level. The energy shift is small and can be treated as a perturbation to the atomic fine structure. By using the high-resolution laser, the perturbation energy shift can be measured providing a probe into the structure of nuclei. This chapter is dedicated to the physics explored in laser spectroscopy and explains the equations to be used in the analysis in the following chapters.

2.1 The Isotope Shift

The energy of a certain atomic transition shifts from one isotope to another. The phenomenon is called the isotope shift. For two isotopes with mass number A and A', the shift in frequency $\Delta\nu^{A,A'}$ is

$$\Delta\nu^{A,A'} = \nu^{A'} - \nu^{A} \tag{2.1}$$

where ν is the centroid of the atomic transition. The isotope shift is made of two contributions: the mass shift due to change in the nuclear mass, and the field shift due to change in the nuclear charge distribution.

2.1.1 The Mass Shift

The nucleus has a finite mass and acquires a recoil energy due to the electrons that orbit it. According to [9], the recoil energy E_{MS} should fulfil the conservation of momentum for a stationary atoms:

$$\boldsymbol{p_n} = -\sum \boldsymbol{p_i} \tag{2.2}$$

where $\boldsymbol{p_n}$ is the momentum of nucleus and $\boldsymbol{p_i}$ is the momentum of an individual electron. The nuclear recoil energy is thus given by

$$E_{MS} = \frac{1}{2m_A}\big(\sum_i \boldsymbol{p_i}\big)^2 = \frac{1}{2m_A}\sum_i \boldsymbol{p_i^2} + \frac{1}{2m_A}\sum_{i>j}(2\boldsymbol{p_i}\cdot\boldsymbol{p_j}) \tag{2.3}$$

where m_A is the mass of nucleus. For a certain element, the different masses of different isotopes give rise to different recoil energies. The difference of the recoil energy is

$$\delta E_{MS}^{A',A} = \frac{1}{2}\big(\frac{m_{A'} - m_A}{m_A m_{A'}}\big)\big(\sum_i \boldsymbol{p_i^2} + \sum_{i>j}(2\boldsymbol{p_i}\cdot\boldsymbol{p_j})\big). \tag{2.4}$$

Although the recoil energy can not be measured directly, the shift in the energy of an atomic transition has a contribution from the mass shift. The Equation 2.4 leads to the following expression for the mass shift

$$\delta\nu_M = \delta\nu_{NM} + \delta\nu_{SM} = \big(\frac{m_{A'} - m_A}{m_A m_{A'}}\big)(N_M + S_M) = \big(\frac{m_{A'} - m_A}{m_A m_{A'}}\big)K \tag{2.5}$$

The first term arises from the change in the reduced mass of the electron and is exactly calculable. It is known as the normal mas shift (N_M). The second term is the specific mass shift (S_M) due to correlations in electron motion and is much more difficult to calculate reliably. The N_M factor can be easily calculated as $N_M = m_e \nu_0$ where m_e is the mass of an electron and ν_0 is the transition frequency in the infinitely heavy system [9]. The S factor is difficult to estimate by theoretical calculation. Instead, the value can be determined experimentally by a King plot analysis which will be introduced later.

2.1.2 The Field Shift

The second part to the isotope shift is due to the fact that the nuclear charge has an extended distribution. The shift is called field shift and calculated from

$$\delta E_{FS} = e \int_0^\infty \psi_e^*(r) \delta V(r) \psi_e(r) d^3 r \tag{2.6}$$

where $\delta V(r)$ is the difference of the nuclear Coulomb potential between two isotopes and ψ is the wavefunction of the electron. Assuming the wavefunction can be approximated as $\psi(r = 0)$ and constant across the volume of nucleus, the field shift can be approximately given by

$$\delta \nu_{FS} = \frac{Ze^2}{6h\epsilon_0} \Delta |\psi_e(0)|^2 \delta \langle r^2 \rangle^{A,A'} = F \delta \langle r^2 \rangle^{A,A'} \tag{2.7}$$

where $\Delta |\psi_e(0)|^2$ is the difference in the electron density at the nucleus between the upper and lower atomic states of the transition and $\delta \langle r^2 \rangle^{A,A'}$ is the difference of mean square charge radii between the two isotopes. F is called field shift factor.

This approximation is good enough for light and medium nuclei while for heavy ones the effect of non-uniform electron density needs to be considered ($\psi(r)$ varies across the nucleus). In that case, $\delta \langle r^2 \rangle^{A,A'}$ should be replaced by $\lambda^{A,A'}$:

$$\delta \nu_{FS}^{AA'} = F \lambda^{AA'} \tag{2.8}$$

where

$$\lambda^{AA'} = \delta \langle r^2 \rangle^{AA'} + \frac{C_2}{C_1} \delta \langle r^4 \rangle^{AA'} + \frac{C_3}{C_1} \delta \langle r^6 \rangle^{AA'} + \dots$$

The values of the coefficients C_i are tabulated in [13] which are extracted from electron scattering experiments. The value of $\langle r^i \rangle^{A,A'}$ can be calculated from the Barrett equivalent radius obtained from electron scattering and muonic experiments listed in [13].

The combination of Equation 2.5 and Equation 2.8 gives the isotope shift

$$\delta\nu^{A,A'} = \nu^{A'} - \nu^{A} = F\delta\langle r^2 \rangle^{A,A'} + K\frac{m_{A'} - m_A}{m_{A'}m_A}. \tag{2.9}$$

2.2 The Hyperfine Structure

For a nucleus with spin $I \neq 0$, higher multipole electromagnetic moments (the field shift can be regarded as part of the monopole moment) need to be included in the interaction with the atomic electrons. The additional shifts to the atomic energy levels splits an atomic transition into multiple transitions called the hyperfine structure. Due to the rapid drop in magnitude of energy shifts caused by the higher moments, only the magnetic dipole and the electric quadrupole moments are included in this analysis.

2.2.1 The Magnetic Dipole Moment

Some conventions need to be made. $\boldsymbol{I}$ and $\boldsymbol{J}$ are vectors representing the spins of the nucleus and the overall electron system respectively. I and J are the quantum numbers of the maximum components of $\boldsymbol{I}$ and $\boldsymbol{J}$ along the quantization axis and are either integer or half-integer. Nuclei with spin $I \geq 1/2$ posses magnetic moments given by

$$\mu_I = g_I \mu_N I \tag{2.10}$$

where g_I is the g-factor of the nucleus of spin I and μ_N is the nuclear magneton. Assuming the magnetic field generated by the electrons at the position of nucleus is $\boldsymbol{B_J}$, the energy of the magnetic dipole interaction is simply

$$\begin{aligned} \Delta E_M &= -\boldsymbol{\mu_I} \cdot \boldsymbol{B_J} \\ &= \frac{g_I \mu_N B_j}{J} \langle \boldsymbol{I} \cdot \boldsymbol{J} \rangle. \end{aligned} \tag{2.11}$$

By introducing $\boldsymbol{F}$ as the vector sum of $\boldsymbol{I}$ and $\boldsymbol{J}$, the Equation 2.11 can be expressed in the form

$$\Delta E_M = \frac{1}{2} A \big[F(F+1) - I(I+1) - J(J+1) \big] = \frac{1}{2} AC \tag{2.12}$$

where we have used

$$\langle \boldsymbol{I} \cdot \boldsymbol{J} \rangle = \frac{1}{2} \langle \boldsymbol{F} \cdot \boldsymbol{F} - \boldsymbol{I} \cdot \boldsymbol{I} - \boldsymbol{J} \cdot \boldsymbol{J} \rangle$$

and where the hyperfine A factor is given by

$$A = \frac{g_I \mu_N B}{J}.$$

F takes all values between $|I - J|$ and $I + J$ in integer steps so the atomic state is split into $2J + 1$ or $2I + 1$ levels, whichever is the smaller, these are labelled by F (see Figure 2.1).

2.2.2 The Electric Quadrupole Moment

For $I \geq 1$ and $J \geq 1$ the second contribution to the hyperfine structure is due to the interaction energy between the nuclear quadrupole moment and the electric field gradient at the the nucleus:

$$E_Q = eQ_s(\frac{\partial^2 V}{\partial z^2}) P_2(cos\theta) \tag{2.13}$$

where Q_s is the spectroscopic quadrupole moment, θ the angle between $\boldsymbol{I}$ and $\boldsymbol{J}$ and $\frac{\partial^2 V}{\partial z^2}$ is the gradient of the electric field generated by electrons at the nucleus.

The equation can be reduced to

$$\Delta E_Q = B\frac{3C(C+1) - 4I(I+1)J(J+1)}{8I(2I-1)J(2J-1)} \tag{2.14}$$

where the hyperfine B factor is given by

$$B = eQ_s\langle\frac{\partial^2 V}{\partial z^2}\rangle. \tag{2.15}$$

Q_s is the projection of the intrinsic quadrupole moment Q_0 along the quantization axis (the laboratory z-axis for example) and they can be connected by the following expression in an well-deformed nucleus.

$$Q_s = \frac{3\Omega^2 - I(I+1)}{(I+1)(2I+3)}Q_0 \tag{2.16}$$

where Ω is the projection of I on the intrinsic axis. For a well-deformed nucleus, Ω is equal to I for the ground state.

2.2.3 The Hyperfine Structure

The hyperfine structure is the result of the splitting and shift of spectral line discussed above. The allowed electric dipole transitions should follow the selection rules:

1. $\Delta L = 0, \pm 1$ $(0 \not\to 0)$;
2. $\Delta F = 0, \pm 1$ $(0 \not\to 0)$;
3. $\Delta S = 0$;
4. the states should have opposite parities.

The transition coefficient is strongly hindered if one of the conditions is not fulfilled. According to selection rule, a transition from F_i to F_f is allowed $|F_i -$

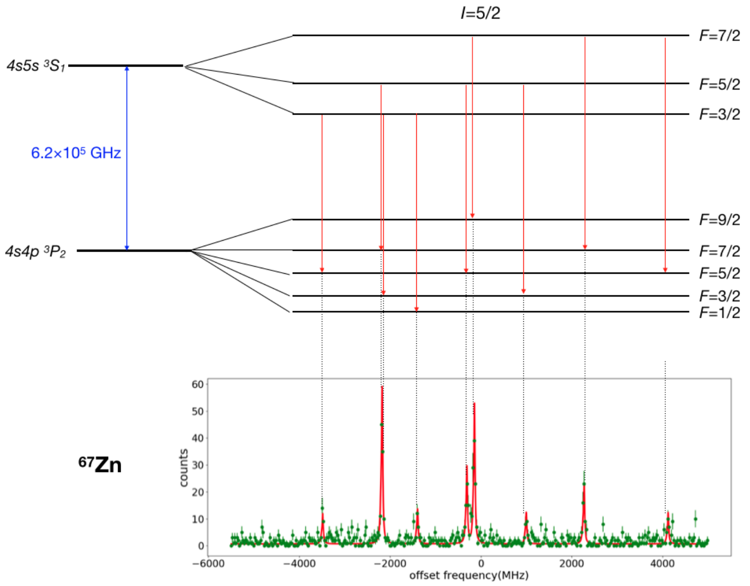

FIGURE 2.1: Illustration of the hyperfine structure of the ground state of ^{67}Zn. The energy shift due to nuclear electric quadrupole moment is not shown because the value is only the order of 10 MHz. The spectrum shown is taken from the experiment which is going to be introduced in the Chapter 4.

$F_f| \leq 1$ and the states have opposite parity. Note $F_i = 0$ to $F_f = 0$ is forbidden. One example is shown in Figure 2.1.

The relative intensities of the transitions in a hyperfine structure can be written as a Wigner $6-j$ symbol describing the coupling of angular momenta involved in the transition [14].

$$\mathcal{I}(f,i) \propto (2F_i+1)(2F_f+1)\begin{Bmatrix} J_f & F_f & I \\ F_i & J_i & 1 \end{Bmatrix}^2 \tag{2.17}$$

where i and f symbolise the initial and final state respectively. In laser spectroscopy, due to the repeated interaction with a laser, the occupation intensities of the F_i are changed. Therefore the measured intensities do not strictly follow the prediction of Equation 2.17.

2.3 Line Shapes in Atomic Laser Spectroscopy

2.3.1 Broadening Mechanisms

When a laser is resonantly tuned to excite an atomic transition between a lower and excited state, the resonance signal is not a sharp line. There are several broadening mechanisms which determine the linewidth.

2.3.1.1 Natural Broadening

There is an intrinsic uncertainty in the energy of atomic excited states. According to Heisenberg's uncertainty principle, $\Delta E \Delta t \geq \hbar$. To convert the energy into the frequency of emitted photon,

$$\Delta\nu = \frac{1}{2\pi\tau} = \Gamma_0, \tag{2.18}$$

where τ is the mean lifetime for the atom/ion to decay to a lower level. The broadening, called natural broadening, is in the shape of a Lorentz profile as

$$L(\nu) = \frac{\frac{\Gamma_0}{2\pi}}{(\Gamma_0/2)^2 + (\nu - \nu_0)^2} \tag{2.19}$$

where Γ_0 is the full width at half maximum(FWHM) of the Lorentz profile. Γ_0 can be evaluated from the rates of all spontaneous decays from the upper state, labelled n to all available lower states labelled n'.

$$\Gamma_0 = \frac{\sum_{n'} A_{nn'}}{2\pi} \tag{2.20}$$

2.3.1.2 Power Broadening

Alongside spontaneous decay, the ions/atoms also experience stimulated emission, when they interact with a laser at resonant frequency. The process reduces the effective lifetime in Equation 2.18 hence introducing the power broadening to further widen the linewidth. The line shape is still a Lorentz profile but with modified FWHM given by

$$\Gamma = \Gamma_0 \sqrt{1 + I/I_s} \tag{2.21}$$

where I is the intensity of laser and I_s the saturating intensity of laser defined by:

$$I_s = \frac{h\pi\nu_0^3\Gamma_0}{3c^2}. \tag{2.22}$$

2.3.1.3 Doppler Broadening

The thermal motions of ions/atoms cause the laser to be observed in a shifted frequency due to the Doppler effect. Because the spread of the thermal energy follows the Maxwell-Boltzmann distribution, the Doppler broadening can be described by a Gaussian profile

$$G(\nu) = \frac{1}{\sqrt{2\pi\sigma^2}} e^{-\frac{(\nu-\nu_0)^2}{2\sigma^2}} \tag{2.23}$$

where

$$\sigma = \frac{\nu_0}{c}\sqrt{\frac{kT}{m}}. \tag{2.24}$$

The collinear beams method used in this work eliminates the bulk of the normal Doppler broadening but there can still be a residual contribution.

2.3.1.4 The Voigt Profile

Combining all the broadening mechanisms above, the measured line shape is the convolution of a Lorentz profile and a Gaussian profile, namely, a Voigt profile given by

$$V(\nu) = \int_{-\infty}^{\infty} G(\nu')L(\nu - \nu')d\nu'. \tag{2.25}$$

For practical purposes, a pseudo-Voigt profile was used as an approximation to reduce the time of calculation.

$$V_{pseudo}(\nu) = \eta L(x, \Gamma) + (1 - \eta)G(x, \Gamma) \quad \text{with } 0 < \eta < 1 \tag{2.26}$$

The pseudo-Voigt is a linear combination of Lorentz and Gaussian profiles which share the same Γ, the FWHM.

2.3.2 Asymmetric Line Shape

In collinear spectroscopy, the line shape is often found to be asymmetric. For the collinear overlapping of ion/atom beam and laser, a 'tail' often appears on the low frequency side of the peak. The explanation is that part of the ion/atom beam lose some kinetic energy in the interaction with the particles in its passage. And extra co-propagating acceleration voltage is needed for Doppler tuning to reach the resonant point. In collinear laser spectroscopy, higher voltage corresponds to lower frequency.

One possible mechanism is the collisional excitation caused by ions/atoms colliding with particles within the beamline. The particles could be either the residual gas, or the charge exchange vapour in the case of the atom beam. Partial kinetic energy is lost to the excitation of ions/atoms to higher states. The fraction of excited ions/atoms decaying back to the state of interests would produce satellite resonance peaks shifted by a voltage corresponding to the excitation energy in eV. The probability of multiple collisional excitations follows a Poison distribution

$$P(k) = e^{-\lambda} \frac{\lambda^k}{k!}, \tag{2.27}$$

where λ is the average number of collisional excitations which increases if the density of beamline particles increases.

The typical energy spread of an ion source at ISOLDE is about 3 eV while the energy of collisional excitation is the same order. It is difficult to resolve the satellite peaks. In some early work on Na of low energy spread [16], the satellite peaks were well observed (see Figure 2.2) and their intensity confirmed the expectation in Equation 2.27.

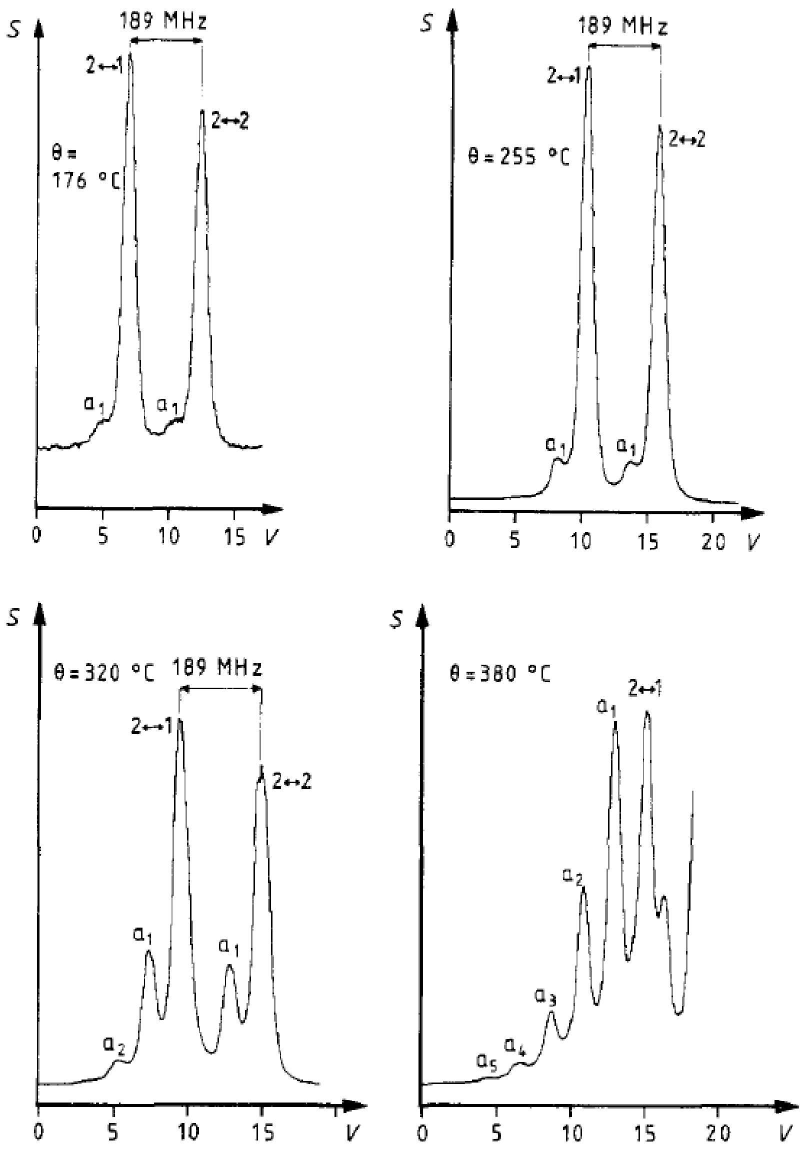

FIGURE 2.2: Satellite peaks observed in a Na on Na experiment [16]. θ is the temperature of the charge exchange. The higher temperature increases the density of the charge exchange vapour hence higher satellite peaks a_i.

The other possible mechanism only applies to an atomic transition following the neutralization. In the process of charge exchange, higher states could be populated and later decay to the state of interest. The energy needed is again compensated by the kinetic energy.

The situation could be more complicated if multiple higher states are populated and decay to the level of interest. When the satellite peaks can not be well resolved, the asymmetry can only be determined empirically using the measurement of strong resonances (most of time the single resonance of even-A isotopes) of high statistics. And the result is more phenomenological than determinant.

2.4 Nuclear Models

There are numerous nuclear models with which one can explore the structure of nuclei. Each model is established under different assumptions and approximations.The approximations used are made to simplify the nuclear many-body problem and to focus a model's predictive power on certain aspects of the nuclear structure or on particular nuclear observables. Although each have their own limitations, good predictive power can be achieved in restricted regions of Z and N.

Broadly speaking, the nuclear models can be classified into two groups: macroscopic and microscopic. Examples which use a macroscopic approach are the liquid drop model, droplet model and some deformed shell models. Such models are often used to predict how nuclear size or deformation evolve as Z and N vary. The microscopic methods, including shell model and *ab initio* calculation, establish a theoretical description based on (modelled) interaction among individual nucleons. Successful predictions can often be made for properties such as the magnetic dipole moment and the spin with these determined by a single or few nucleons (outside and inert core).

2.4.1 Nuclear Charge Radii Predicted by the Droplet Model

The droplet model is an extension to the liquid drop model. Both models study the nucleus using a macroscopic approach considering the average properties of nuclei. In the droplet model, extra terms are added to the semi-empirical mass formula to describe the variation of nucleon density. Compared to the liquid drop model, parameter $\overline{\delta}$ is introduced as the asymmetry parameter (defined later in this section) which acts to separate the distribution of neutrons and protons in the model (and permits the two to have different mean square radii).

$$\begin{aligned} E(N, Z; shape) =& [a_1 + J\overline{\delta}^2 - \frac{1}{2}K\overline{\epsilon}^2 + \frac{1}{2}M\overline{\delta}^4]A \\ &+ [a_2 + \frac{9}{4}(J^2/Q)\overline{\delta}^2]A^{2/3}B_s \\ &+ a_3A^{1/3}B_k + c_1Z^2A^{-1/3}B_c \\ &- c_2Z^2A^{1/3}B_r - c_3Z^2A^{-1} \\ &- c_4 2^{-1/3} - c_5Z^2B_w \end{aligned} \tag{2.28}$$

In Equation 2.28, $\overline{\epsilon}$ is the dilatation parameter. It is defined and calculated by

$$\overline{\epsilon} = \frac{1}{3}\frac{\rho_\infty - \overline{\rho}}{\rho_\infty} = [-2a_2A^{-1/3}B_s + L\overline{\delta}^2 + c_1Z^2A^{-4/3}B_c]/K \tag{2.29}$$

where ρ_∞ is the saturation density and $\overline{\rho}$ is the average density of nuclear matter. $\overline{\epsilon}$ is based on the variation of the density of nucleons especially at the surface of nucleus.

The $\overline{\delta}$ is the asymmetry parameter, defined and calculated by

$$\overline{\delta} = \frac{\overline{\rho}_n - \overline{\rho}_p}{\overline{\rho}} = \frac{I + \frac{3}{16}(c_1/Q)ZA^{-2/3}B_v}{1 + \frac{9}{4}(J/Q)A^{-1/3}B_s} \tag{2.30}$$

where $\overline{\rho}_n$ and $\overline{\rho}_p$ are the average neutron and proton densities and $\overline{\rho} = \overline{\rho}_n + \overline{\rho}_p$, and $I = (N - Z)/A$. Other parameters appearing in Equation 2.28, 2.29 and 2.30 are going to be mentioned later.

The droplet model calculates the contribution of volume (i.e. the average properties) to the nucleus size. The radius of nuclear matter R is calculated by

$$R = r_0A^{1/3}(1 + \overline{\epsilon}). \tag{2.31}$$

The $\bar{\epsilon}$ is defined in Equation 2.29. The B_i in Equations 2.29 and 2.30 are the various shape dependencies, which can be calculated by expansions as

$$B_s = 1 + \frac{2}{5}\alpha_2^2 - \frac{4}{105}\alpha_2^3 - \frac{66}{175}\alpha_2^4 - \frac{4}{35}\alpha_2^2\alpha_4 + \alpha_4^2 + \cdots \tag{2.32}$$

$$B_c = 1 - \frac{1}{5}\alpha_2^2 - \frac{4}{105}\alpha_2^3 + \frac{51}{245}\alpha_2^4 - \frac{6}{35}\alpha_2^2\alpha_4 - \frac{5}{27}\alpha_4^2 + \cdots \tag{2.33}$$

$$B_v = 1 - \frac{1}{5}\alpha_2^2 - \frac{2}{105}\alpha_2^3 - \frac{253}{1225}\alpha_2^4 - \frac{4}{105}\alpha_2^2\alpha_4 + \frac{4}{9}\alpha_4^2 + \cdots \tag{2.34}$$

Higher terms are neglected in calculation. The α_i are related to the deformation of the nucleus and can be derived from deformation coefficients β_i: $\alpha_i = \sqrt{\frac{5}{4\pi}}\beta_i$.

The mean square charge radii of nuclei in the droplet model can be divided into three parts:

$$\langle r^2 \rangle = \langle r^2 \rangle_u + \langle r^2 \rangle_r + \langle r^2 \rangle_d. \tag{2.35}$$

$\langle r^2 \rangle_u$ is the contribution of from the uniform distribution and the shape of nucleus,

$$\langle r^2 \rangle_u = \frac{3}{5}R^2(1 + \alpha_2^2 + \frac{10}{21}\alpha_2^3 - \frac{27}{35}\alpha_2^4 + \frac{10}{7}\alpha_2^2\alpha_4 + \frac{5}{9}\alpha_4^2 + \cdots). \tag{2.36}$$

$\langle r^2 \rangle_r$ is the contribution of redistribution. It contains the effects from non-uniformities such as the asymmetry of density between proton and neutron,

$$\langle r^2 \rangle_r = \frac{12}{175}C'R^2(1 + \frac{14}{5}\alpha_2^2 + \frac{28}{15}\alpha_2^3 - \frac{29}{5}\alpha_2^4 + \frac{116}{15}\alpha_2^2\alpha_4 + \frac{70}{26}\alpha_4^2 + \cdots), \tag{2.37}$$

where

$$C' = \frac{1}{2}\Big(\frac{9}{2K} + \frac{1}{4J}\Big)\frac{Ze^2}{R_Z}, \tag{2.38}$$

and R_z is the effective sharp radius for the proton distribution (the charge radius).

The final part $\langle r^2 \rangle_d$ is the contribution from the diffuseness of the nuclear surface:

$$\langle r^2 \rangle_d = 3b^2. \tag{2.39}$$

The assumption is the diffuseness is constant regardless of the shape and different nuclei.

The values of the parameters are obtained by minimizing the macroscopic potential energy (Equation 2.28). Names of the coefficients appearing in the droplet model equations are listed as below and the values used in this work were quoted from [15]:

$r_0 = 1.18$ fm, the nuclear radius constant,

$b = 0.99$fm, the nuclear diffuseness,

$a_1 = 15.96$ MeV, the volume-energy coefficient,

$a_2 = 20.69$ MeV, the surface energy coefficient

$a_3 = 0$, curvature-correction coefficient,

$J = 36.8$ MeV, the symmetry energy coefficient,

Q =17 MeV, the effective surface stiffness,

$K = 240$ MeV, the compressibility coefficient,

$L = 100$ MeV, the density symmetry coefficient,

$R_z = r_0(2Z)^{1/3}(1 + \bar{\epsilon} + \frac{1}{3}\bar{\delta})$, the charge radius,

$c_1 = \frac{3}{5}(e^2/r_0) = 0.7322$ MeV, the Coulomb energy coefficient,

$c_2 = (c_1^2/336)(1/J + 18/K) = 0.00016302$ MeV, the volume-redistribution coefficient,

$c_3 = \frac{5}{2}c_1(b/r_0)^2 = 1.28846$ MeV, the diffuseness-correction coefficient,

$c_4 = \frac{5}{4}\left(\frac{3}{2\pi}\right)^{2/3} c_1 = 0.55911$ MeV, exchange-correction coefficient,

$c_5 = \frac{1}{64}(c_1^2/Q)$ =0.00049274 MeV, the surface-redistribution coefficient.

2.4.2 The Shell Model

The nuclear shell model was first proposed by Mayer [17] and Jensen [18] in 1949 as an analogy to the atomic electron configuration. The model, nowadays referred as single particle shell model, approximates the interactions among nucleons as a phenomenological mean potential such as an Harmonic Oscillator or Woods-Saxon potential. It was realised later a spin-orbit potential and orbit-orbit term are necessary. Taking the Harmonic Oscillator as an example, the overall potential can be expressed as [19]

$$\boldsymbol{U}(r) = \frac{1}{2}mw^2r^2 + D\boldsymbol{l}^2 + C\boldsymbol{l}\cdot\boldsymbol{s} \tag{2.40}$$

Each nucleon interacts independently with the potential resulting in a group of discrete states which are occupied by nucleons according to the Pauli exclusion principle. The wavefunction of the nucleus can be described by a Slater determinant ϕ_i where i stands for different nuclear configurations of the calculated states. The prediction was successful in theoretically reproducing the magic numbers and explaining the properties of the stable nuclei close to closed shells. For nuclei with several valence nucleons or far away from the valley of stability, the residual interaction which is regarded as nucleon-nucleon correlations becomes indispensable.

Although the single particle shell model has limited application, further improvements retained the shell concept and the Slater determinants. The shell model Hamiltonian can be written in two terms [19]

$$\boldsymbol{H} = \sum_{\alpha} \epsilon_\alpha a_\alpha^\dagger a_\alpha + \frac{1}{2}\sum_{\alpha\beta\gamma\delta} V_{\alpha\beta\gamma\delta} a_\alpha^\dagger a_\beta^\dagger a_\delta a_\gamma. \tag{2.41}$$

where a and $a^\dagger$ are fermion annihilation and creation operators, ϵ the single particle energy, and V the matrix element for two-body interaction. The Hamiltonian matrix element can be expressed by all possible Slater determinants as

$$\begin{pmatrix} \langle\phi_1|H|\phi_1\rangle & \langle\phi_1|H|\phi_2\rangle & \cdots & \langle\phi_1|H|\phi_n\rangle \\ \langle\phi_2|H|\phi_1\rangle & \langle\phi_2|H|\phi_2\rangle & \cdots & \langle\phi_2|H|\phi_n\rangle \\ \vdots & \vdots & \cdots & \vdots \\ \langle\phi_n|H|\phi_1\rangle & \langle\phi_n|H|\phi_2\rangle & \cdots & \langle\phi_n|H|\phi_n\rangle \end{pmatrix} \tag{2.42}$$

The diagonalization of the matrix generates the eigenvalues. The final wavefunction of the nucleus can be expressed in the basis of the Slater determinants as

$$\Psi = \sum_{i}^{n} c_i\phi_i. \tag{2.43}$$

In order to simplify the calculation, a truncated model space is usually employed as only selected states are allowed with a dynamic nucleon distribution. As shown in Figure 2.3, the states below the model space are regarded as a fully occupied core and the states above always empty.

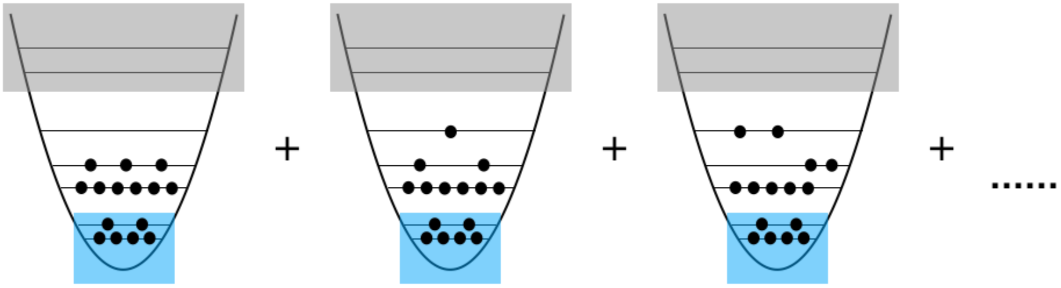

FIGURE 2.3: The grey shaded states which form the external space are always empty. The blue shaded states are fully occupied acting as an inert core. The rest of the states are called the model space which has a dynamic nucleon distribution.

The remainder of this page was intentionally left blank.

Chapter 3

Collinear Laser Spectroscopy at ISOLDE, CERN

The collinear laser spectroscopy experiments reported in this work use laser light to resonantly excite isotopes produced by the isotope separator on-line facility (ISOLDE at CERN). The spectra obtained depend upon the nuclear properties of ground and isomeric states. These properties: the mean square charge radii, magnetic-dipole moments, electrostatic-quadrupole moments and nuclear spin, provide a sensitive test of nuclear structure theory.

3.1 The Isotope Separator On-line Facility, ISOLDE

As defined in [20], an ISOL instrument is the combination of target, ion source and electromagnetic mass analyser, used to produce intense isobaric radioactive ion beams. At ISOLDE a 1.4 GeV proton beam hits the target to produce radioactive nuclei. This proton beam, delivered from the PS booster, has a pulsed structure with a period of 1.2 s. Individual proton pulses are delivered to each of the experiments at CERN, as required. The intensity of the proton pulses and specific sequence to be delivered to ISOLDE are tuned to give optimal experimental conditions for the specific case. An average proton intensity of up to 2μA is routinely used by ISOLDE.

A number of different target materials are employed at ISOLDE. For each experiment a target material is selected to maximise the production of the isotopes of interest and minimize the time required for the radioactive atoms to effuse from the target. Heating of the target material minimizes the effusion time for the atoms of interest, but also reduces the usable lifetime of the target due to sintering. Here a temperature must be selected to minimize the release time while maintaining an acceptable target lifetime. In both the Zn and Ni experiments reported in this thesis a uranium carbide (UC_x) target was used.

Once the radioactive atoms have escaped from the target material they must be ionized prior to mass separation. Surface, plasma and laser ion sources are used depending on the element to be ionized. The laser ion source at ISOLDE is called RILIS (Resonance Ionization Laser Ion Source.) It employs tunable-pulsed lasers to achieve multi-step resonant ionization. Due to the unique sequence of atomic energy levels for each element, the element of interest can be selectively ionized.

Spallation, fission and fragmentation reactions contribute to the production of radioactive nuclei. The neutron-rich isotopes of interest tend to be produced by proton-induced fission of the uranium. The isobaric contaminations from higher atomic number elements (for example Ga(Z=31) and Rb(Z=37) in the experiments on Ni(Z=28) and Zn(Z=30)) tend to be from fragmentation reactions. These contaminations can be suppressed by using a proton-neutron converter to restrict reaction in the uranium to neutron-induced fission only. To do this, a tungsten rod was installed next to the target (see Figure 4.1). The proton beam was focussed on the rod and the target was hit by spallation neutrons. Since the kinetic energy of neutron is the order of MeV, much less than than the primary proton beam, this method also reduces the ‘thermal pulse’ caused by the heat deposited in the target which affects the chemical properties of the target [21]. This method has a disadvantage that the neutrons travel in all directions reducing the effective intensity of the primary beam. Therefore when the measurement moves to the neutron deficient isotopes, the proton beam is usually moved to hit the target directly.

There are two isotope separators at ISOLDE, the General Purpose Separator (GPS) and the High Resolution Separator (HRS). The GPS has one bending magnet while HRS is composed of two magnets to achieve a higher mass resolving power.

3.2 The Ion Cooler-buncher (ISCOOL)

After mass separation, the ion beam is injected in to ISCOOL which is a gas-filled radio-frequency quadrupole cooler and buncher. The typical pressure of the helium gas is between 0.01 mbar and 0.1 mbar. The ion beam is slowed down by a DC potential to about 100 eV and thermalised by collisions with the helium gas. In order to confine the scattered ions, the radio-frequency potential is generated by a quadrupole structure made of four parallel rods. The rods at opposite positions are coupled with voltages of the same phase. While ions are confined at the centre of the transverse plain, they are guided through ISCOOL by 25 DC segmented electrodes. The longitudinal potential is shown in Figure 3.1. ISCOOL is capable of working in both continuous beam and ion bunch modes. In bunch mode, the last DC electrode is held at a +50 V trapping potential, and ions are accumulated with a small spatial and energetic distribution. The typical release time is of the order of 10 μs when the trapping potential is reduced to zero. As the ions are released an extraction electrodes focuses the ion beam through the step-down insulation to ground potential. The difference between cooler platform and ground is referred as the cooler voltage,the value of which is fixed at the beginning of the experiment (and monitored for any drift).

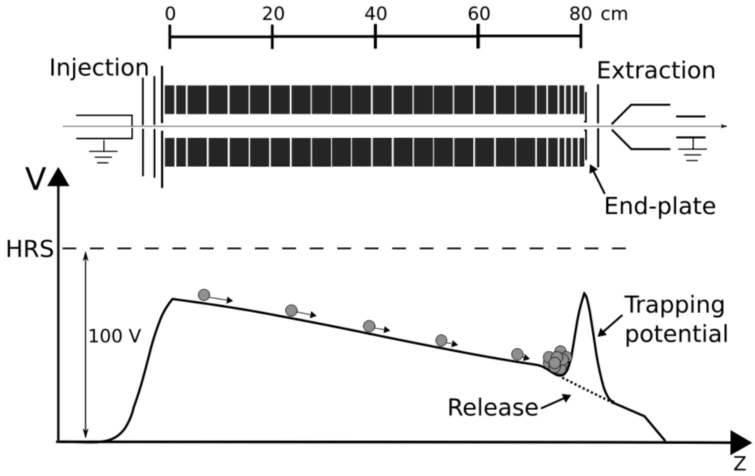

FIGURE 3.1: ISCOOL trapping and rejection potential [22].

3.3 The Charge Exchange Cell

If the object of an experiment is a transition in the neutral atom, the ions need to be neutralized prior to the detection region by passing them through a charge exchange cell (CEC). As shown in Figure 3.2, the CEC which is installed in a metallic vacuum chamber is a tube wrapped in a coaxial heating cable. The heating vaporises the alkali metal within the tube. Cooling oil circulates through copper blocks at the ends of the CEC to reduce the alkali vapour escaping to other part of the beamline. The ions are neutralized through the collisions with atoms in the alkali vapour.

Before the CEC there is the last group of post-acceleration electrodes. The voltage applied on the CEC is a combination of a Fluke high voltage supply and a variable DAC (digital to analogue converter) voltage amplified by a Kepco fast linear-voltage amplifier. The Fluke voltage is adjustable to compensate for the kinematic shift due to the different masses of isotopes. The DAC is controlled by the data acquisition computer and provides the Doppler tuning for the frequency scanning of the hyperfine structure. The Kepco amplification factor is determined from calibration scans using a precision voltmeter.

FIGURE 3.2: CEC tube.

3.4 Fluorescence Detection

The layout of the COLLAPS beamline is shown in Figure 3.3. Before the CEC, the ion beam is bent 10° by two deflector plates and overlapped with the laser. The laser resonantly excites the atoms or ions. The photons released from the decay are detected by four photomultiplier tubes (PMT) installed in two rows on opposite sides of the beam line after the CEC. In front of each PMT a pair of 100 mm diameter spherical lenses are installed to focus photons onto the PMTs, increasing the detection efficiency.

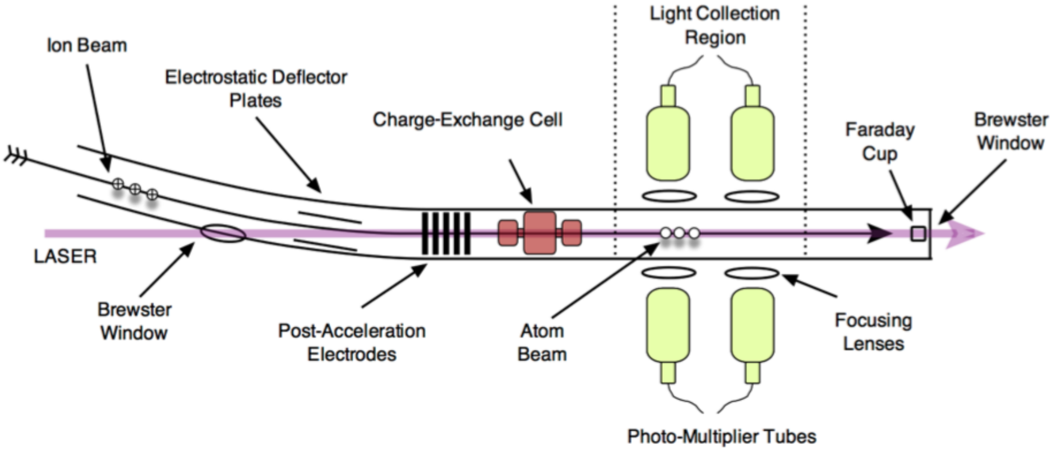

FIGURE 3.3: COLLAPS beamline [23].

3.5 Data Dcquisition

The data acquisition cycle can be proton pulse triggered or non-proton triggered. If the element has a long release time and the half life is also long, the beam intensity will be approximately constant between two adjacent proton pulses, and so the accumulation-release period repeats automatically without the proton trigger. The DAC voltage increases one step after one accumulation-release period. For elements with a short release time, the extracted ions concentrate within a short time after the proton pulse. The data acquisition is triggered by a proton pulse and several accumulation-release periods covering only that short time are used to collect data. In this mode the DAC voltage increases by one step for each proton pulse. The process is illustrated in Figure 3.4.

In both modes, the accumulation time is set to prevent overfilling of ISCOOL. Overfilling the cooler would result in the ions not beginning from the bottom of the potential well, but from some point higher up the well, which would be determined by the number of ions in the bunch.

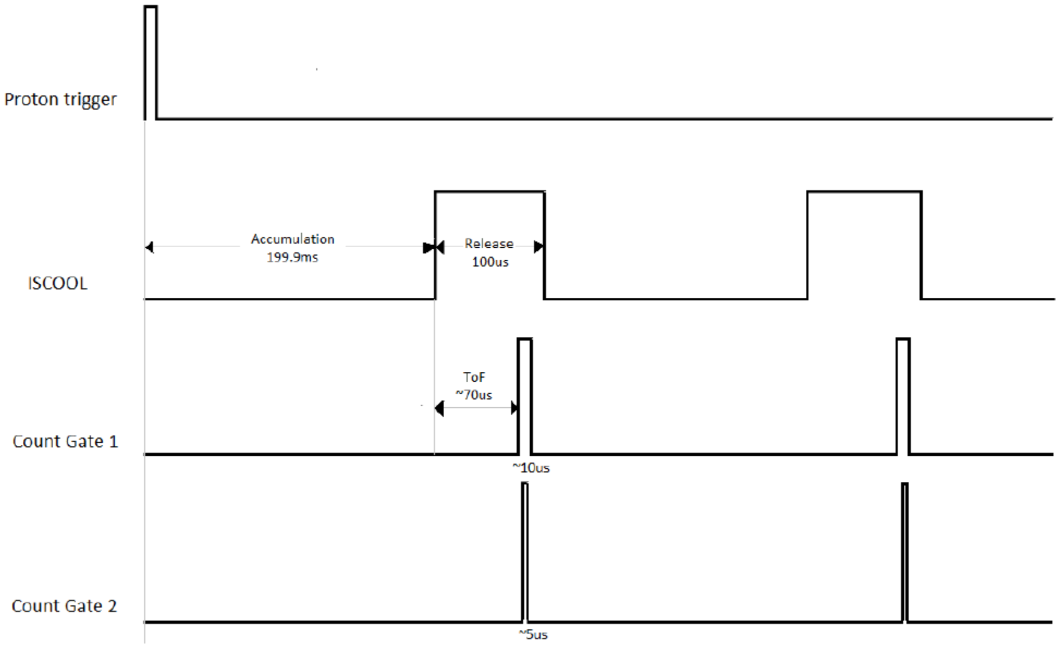

FIGURE 3.4: Example of signals sent to the data acquisition system. The count gate corresponds to the time when the bunched beam is passing through the detection region.

3.6 The Laser System

When an excited atom decays to a lower energy state it emits a photon (spontaneous emission). For stimulated emission, a photon with the specific energy of the transition causes an excited atom to decay to a lower level. The emitted photon has the same phase, energy, polarization and direction of propagation as the incoming photon. The process is demonstrated in Figure 3.5. A laser device employs the stimulated emission process to generate spatially and temporally coherent, single-frequency light. A population inversion between the upper and lower states is necessary and usually involves a pumping mechanism.

In laser spectroscopy, a frequency-tunable laser is necessary to match the chosen transition frequency. The laser used in this work was a Matisse continuous wave (CW) laser produced by Spectra-Physics. The gain material was a Titanium-doped Sapphire (Ti:Sa) which could cover a wavelength range from under 700 nm to over 1000 nm. In both the Zn and Ni experiments, a WaveTrain external cavity was used to double the laser frequency. The following section will introduce some properties of the devices and the frequency stabilization methods used in the experiments.

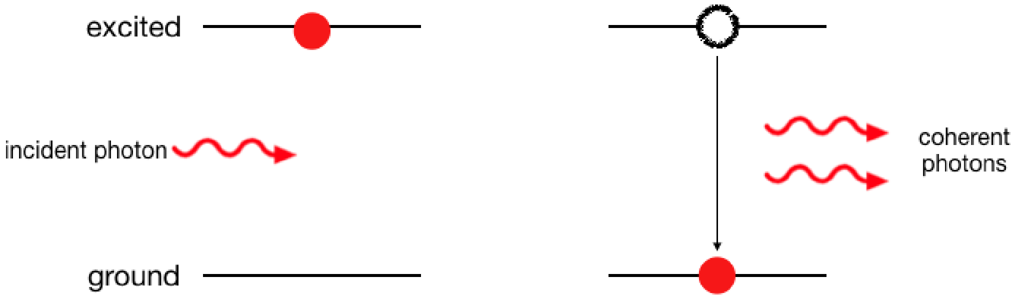

FIGURE 3.5: Illustration of stimulated emission.

3.6.1 The Matisse Laser

The Matisse laser is a continuous wave (CW) laser. It uses either Titanium-doped Sapphire (Ti:Sa) or various dyes as the amplification medium. Most models can be converted between the two versions by some modifications to the layout. The resonator is a ring-shape formed by a set of mirrors. One mirror is attached to an actuator (fast piezo in Figure 3.6) to modulate the cavity length. The Matisse laser works with a Millenia eV pumping laser emitting up to 15W of 532 nm light. Since only the Ti:Sa was used in the work described in this thesis, the following text will focus on the crystal version.

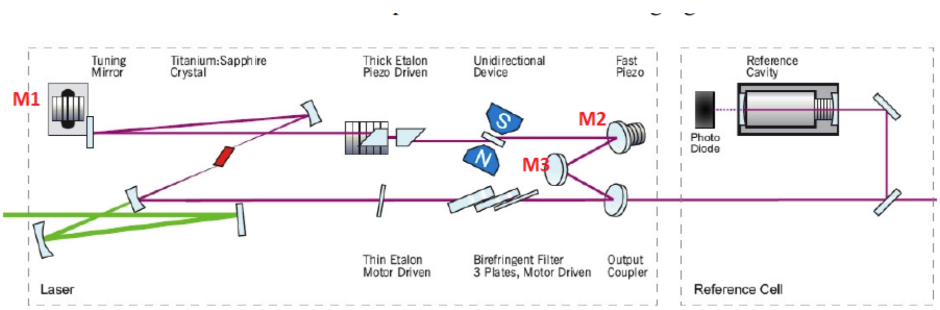

FIGURE 3.6: The layout of the Matisse TS laser [24] for the Ti:Sa version.

The emission spectrum of Ti:Sa covers a range from below 700 nm to over 1000 nm. Various frequency selective elements enable the Matisse to operate on a single cavity mode. Figure 3.6 demonstrates the layout of the elements in the Matisse laser. The frequency selection mechanism involves the following components:

1. Mirror coatings. The mirrors (M1, M2 and M3 marked in Figure 3.6) which form the resonator have high reflection coefficients only for a certain range of wavelength. For instance, the MOS-2 mirrors set used in this experiment works for the range between 750 nm to 870 nm.

2. Birefringent filter (BiFi). It consists of three quartz plates stacked and oriented at Brewster's angle. The quartz plates are birefringent. Light passing through the BiFi is divided into two components with polarization parallel and perpendicular to the optical axis. The two components travel with different speeds and therefore become out of phase resulting in a rotation to the polarization of the emerging light. The Brewster's angle acts as a filter to suppress all frequencies with a polarization component perpendicular to the plane of the cavity. As the angle of rotation is decided by the frequency

and the angle between the incident light and the optical axis, the variation of frequency is achieved by rotation of the set of quartz plates. The stack of three quartz plates which have parallel optical axes enhances the filtering efficiency. The BiFi narrows the range of frequency to approximate 50 GHz.

3. A solid state Fabry-Perot etalon called the Thin Etalon (TE). It is held by a mount controlled by a motor which modulates the relative position of the TE to change the frequency of laser.The free-spectral range is 250 GHz.

4. Piezo Etalon (PE) also called Thick Etalon. The PE is formed by two prisms with an air gap in-between functioning as a Fabry-Perot interferometer. One prism is mounted to a piezo-electric actuator to control the thickness of the air gap and hence the transmission spectrum. The free-spectral range is 20 GHz. Compared to TE, PE has higher Finesse (about 3) and narrower selection of frequency.

   The mode of the PE coincides with the mode of the resonator. The frequency of the mode of the resonator is determined by

$$\nu = \frac{nc}{L} \tag{3.1}$$

   where L is the length of the resonator, c the speed of light and n an integer.

3.6.2 The WaveTrain Cavity

When light travels through a transparent medium, the electric field of the light induces an electric polarization of the medium. If the polarization has a $\chi^{(2)}$ non-linear term, light with twice the frequency of the incident light is generated. The process is called Second Harmonic Generation (SHG), and is used to exactly double the frequency of the laser. The power of the frequency doubled light P_2 is proportional to square of power of the fundamental light P_1 as

$$\mathrm{P}_2 = \gamma {\mathrm{P}_1}^2$$

where γ is the conversion coefficient. Because the power of CW laser is usually of the order of a watt, an external resonator is required to store the light of many round trips to provide sufficient power by coherent superposition of the light. The WaveTrain produced by Sirah is such a passive resonator in which the path of light forms a triangle as shown in Figure 3.7. The typical conversion efficiency in the Zn and Ni experiments reached about 10%.

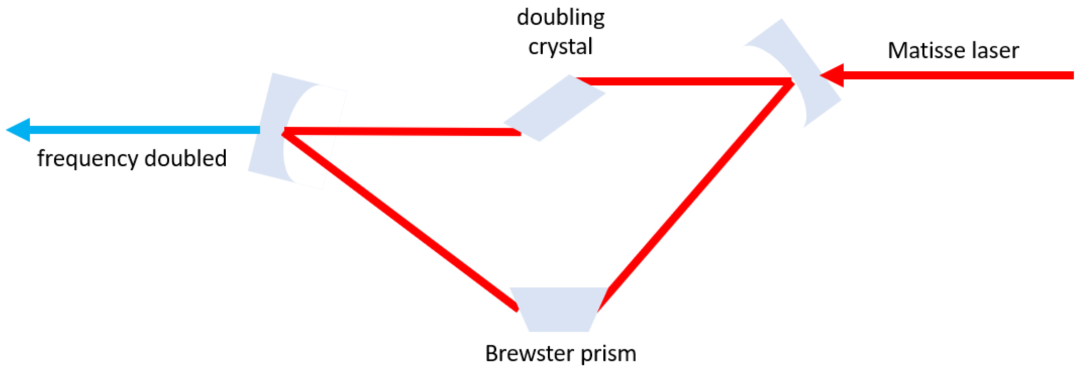

Figure 3.7: Layout of the WaveTrain cavity.

3.6.3 Stabilization Scheme

Due to variations of operation conditions such as temperature and atmospheric pressure of elements, the frequency of the laser drifts and sometimes even jumps from one mode to another. In order to compensate the effects of unexpected changes and to stabilize the frequency, several stabilization mechanisms were used to actively control the elements of the Matisse laser. A range of systems are employed to simultaneously correct for both short-term fluctuations and long-term drift.

3.6.3.1 Locking to the 'Side of Fringe'

This method involves a confocal resonator which is included in the Matisse system as an auxiliary component. Part of the output light is directed into the external resonator and the transmission of light is detected by a photodiode (shown in

Figure 3.6). The tuning mirror shown in Figure 3.6 is mounted on a long-stroke piezo actuator. The length of the resonator is adjusted to a position where the frequency of the laser is approximately at the 50% transmission point of fringe (‘side of fringe’). The deviation of the laser frequency would result in a change of transmission intensity detected by the photodiode which can be sent as an error signal to the control loop of the Matisse laser. The positions of the tuning mirror and fast piezo mirror in Figure 3.6 are adjusted to bring the laser back to the required frequency.

3.6.3.2 External Frequency Reference

For long term stabilization, an external frequency reference is used as a reference. One of the setups shown in Figure 3.8 uses a confocal interferometer (CFI). Light from both the Matisse laser and a helium-neon (HeNe) laser are overlapped and directed through the CFI. The two lasers are divided after the CFI by a cubic beam splitter because they have perpendicular polarizations. The transmission intensities of the two laser beams are detected by two separate photodiodes. The HeNe laser has a stable wavelength (±3MHz over 24 hours) of 632.8 nm. Therefore it is used to calibrate the cavity length of the CFI. Any deviation of the frequency of the Matisse laser results in a change of transmission intensity detected by the other photodiode. The signal is sent as an error signal to the Matisse laser to compensate for the frequency drift.

The HeNe laser can be replaced by a compact saturation spectroscopy system (CoSy) which is able to provide an accurate Doppler-free transition frequency [25]. Since the frequency of the atomic transition is not affected by the environment such as the temperature and humidity, it can be used as the reference to calibrate the CFI. The hyperfine transitions of rubidium, caesium and sodium are commonly used frequency references.

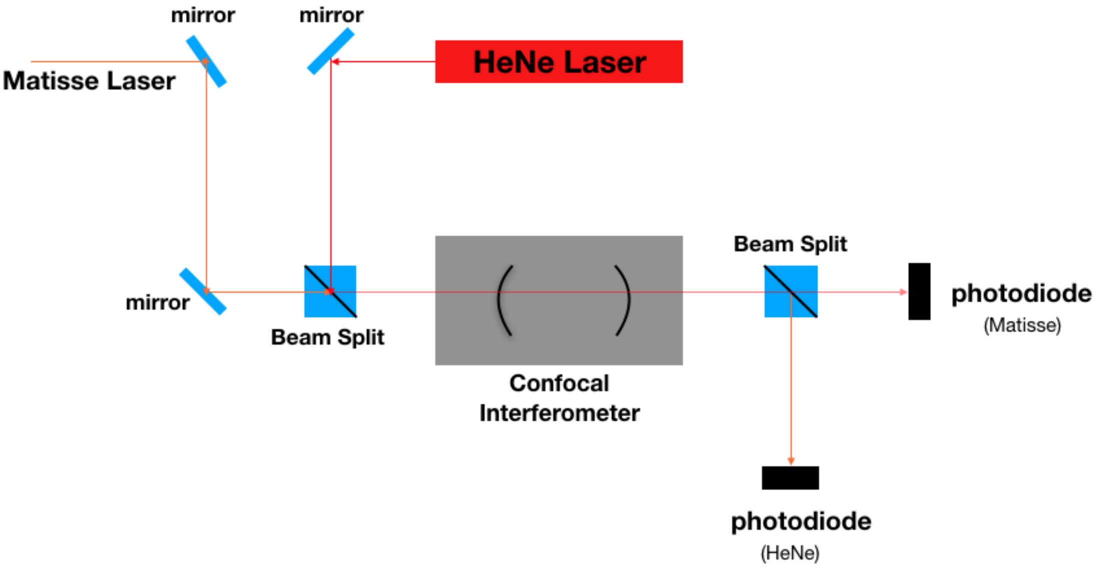

FIGURE 3.8: Setup of the external etalon stabilization.

Chapter 4

Charge Radii of Zinc Isotopes

4.1 The Atomic Transition

The choice of atomic transition should provide a probe to the nuclear moments, namely there should be a hyperfine structure to be measured. There are several points to be considered:

1. When $J_{low} = 0$ and $J_{up} = 1$, there would be three peaks for any I greater than 1/2. It is difficult to distinguish different values of I from the shape of the spectra, and a test on I of the ratio of A_{upper}/A_{lower} can not be used.
2. Transitions with large atomic factors are preferable as the splitting would be large with well-resolved peaks.
3. The lower state of the transition should be well-populated when the atomic beam passes the photon detection region to have the best fluorescence efficiency.
4. The wavelength of the transition must be producible by the lasers.

The wavelengths of ionic transitions of Zn are too short to be efficiently produced. Therefore the experiment needs to be performed on an atomic transition which involves a neutralization process. Shown in Table 4.1, if the transition is from the ground state, only the triplet ${}^3P_J$ states are the candidates with frequency which could be generated by the Matisse laser. For $J = 0$ and $J = 2$, the transitions are forbidden. For $J = 1$, the transition to the ground state is an intercombination transition with half-life about 20 μs [26]. It is too slow to for fluorescence to be produced in the light collection region.

configuration	J	level (cm^{-1})
$4s^2\ {}^1S$	0	0
$4s4p\ {}^3P$	0	32 311.350
	1	32 501.421
	2	32 890.352
$4s4p\ {}^1P$	1	46 745.413
$4s5s\ {}^3S$	1	53 672.280
⋮	⋮	⋮

Table 4.1: Relevant energy levels of the Zn atom [27].

The transition chosen for this experiment is from the lower $3d^{10}4s4p\ {}^3P_2$ at 32890.352 cm^{-1} to the upper $3d^{10}4s5s\ {}^3S_1$ at 53672.28 cm^{-1}. The wavelength is 481 nm which is comfortably in the frequency-tunable Ti:Sa Matisse system with external doubler. A confocal interferometer was used as the external frequency reference for long-term stabilization.

The hyperfine parameters of the lower state in ^{67}Zn are reported in [28]:

$$A({}^3P_2) = +531.987(5)\ \text{MHz},\ B({}^3P_2) = +35.806(5)\ \text{MHz}$$

4.2 The Experiment Setup

The target used in the Zn experiment is made of uranium carbide(UC$_x$). A surface ion source was used with a tungsten rod installed beneath the target as shown in Figure 4.1. As described in the previous chapter, the tungsten rod acted as a proton-neutron converter. In the case of Zn (Z=30), the dominant contaminations are gallium (Z=31) and rubidium (Z=37). As shown in Figure 4.2, Zn has a rather short release time curve after the proton pulse impact while the curve of gallium is quasi-constant. Therefore the data acquisition typically only covered the ion bunches within 600 ms after the proton pulse. The target was heated to above 2000 °C to increase the diffusion and effusion of Zn atoms. Due to the high ionization energy (9.3942 eV) Zn atoms could not be surface ionized. Instead a three step resonant ionization scheme (Figure 4.3) was employed, provided by RILIS. The ion source voltage was 30 keV.

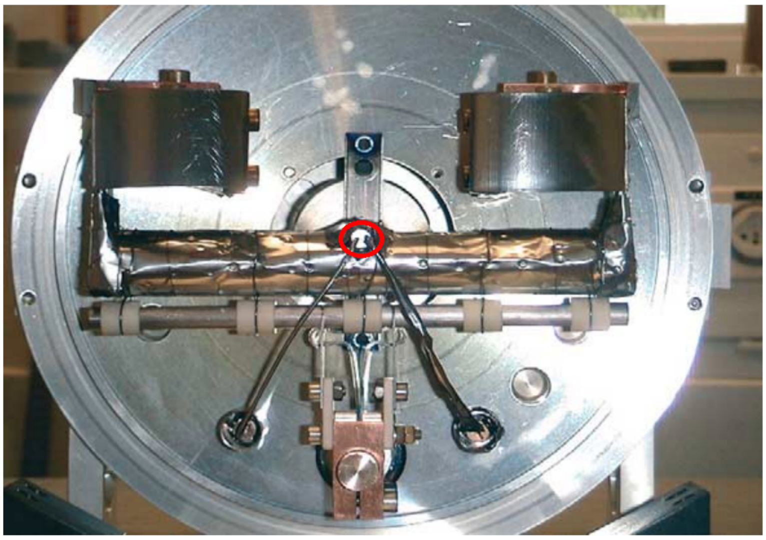

FIGURE 4.1: The UCx target. The whole structure is heated to above 2000 °C so that the diffusion and effusion rates of products are increased. Laser ionization is also applied for fast and selective extraction of the element of interest. The elongated extraction tube (marked by red circle) ensures that the pulsed lasers sufficiently interact with the products. The tungsten rod placed beneath the target is the proton-neutron converter.

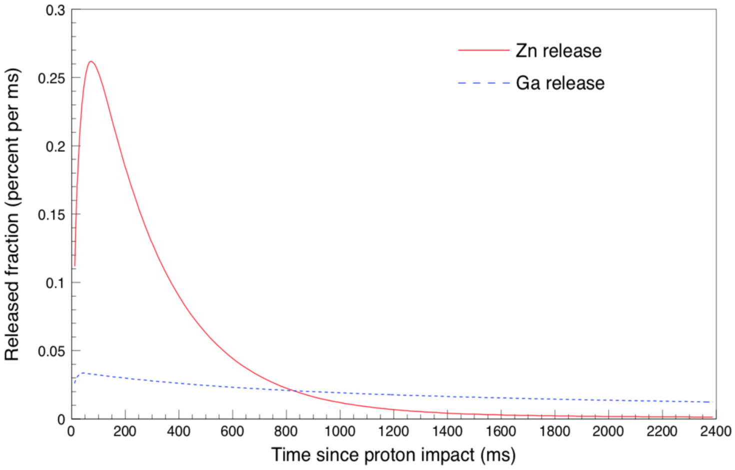

FIGURE 4.2: Typical zinc release time compared to gallium.

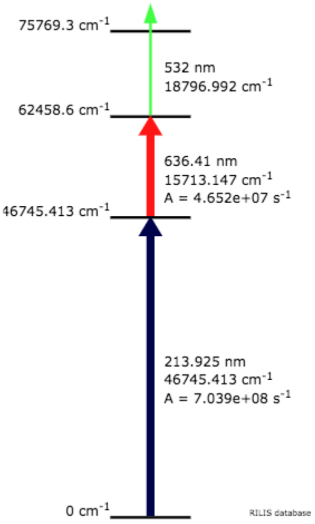

FIGURE 4.3: RILIS ionization scheme for Zn.

Sodium was used for the neutralization and approximately 50 % neutralization efficiency was achieved in the experiment. As shown in Figure 4.4, the ionization energy of sodium is close to the difference between ionization level and triplet-P states of Zn. The triplet ^3P_J should be quasi-resonantly populated. A simulation (Figure 4.5) demonstrates the relative populations of the levels of the Zn atom in the neutralization process and later at the detection region, 40 cm downstream, using the known spontaneous decay coefficients [30].

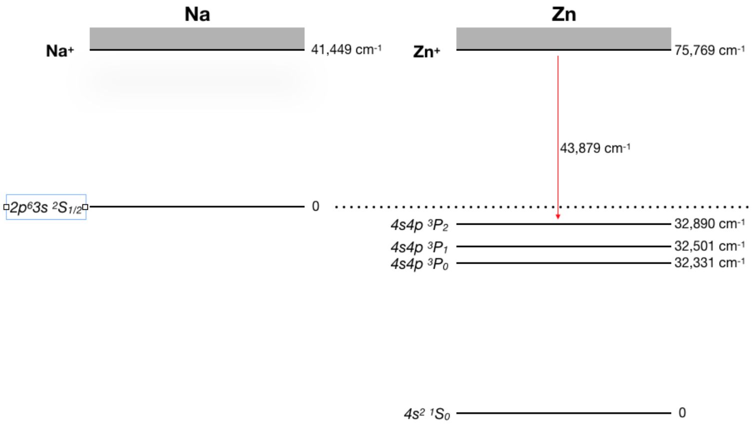

FIGURE 4.4: The triplet-P levels of Zn and Na ionization levels.

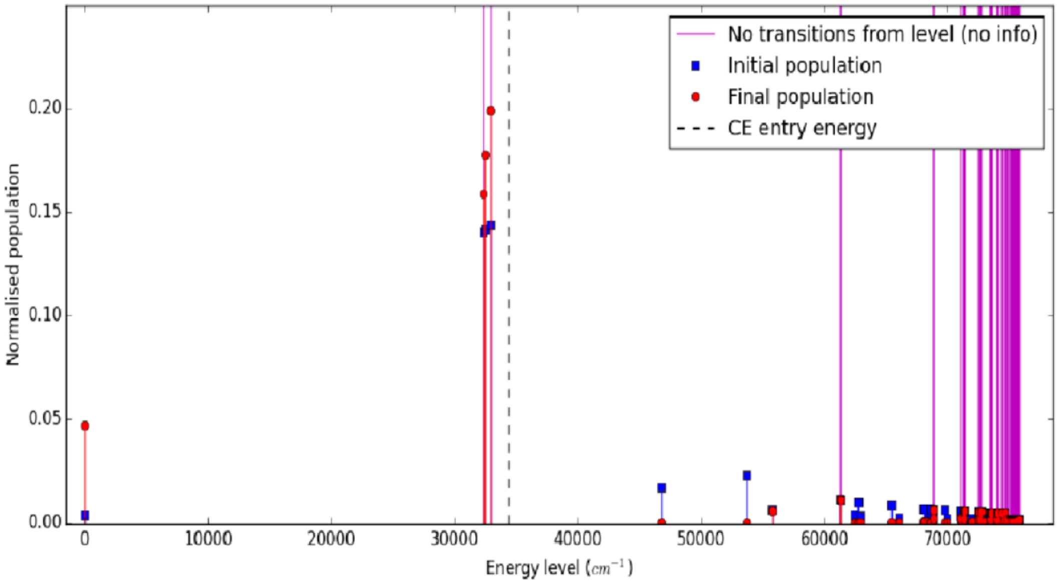

Figure 4.5: Simulation of the population of Zn atomic levels [30].

Due to the short release time, the data acquisition was set to proton triggered mode. The typical accumulation and release times in the Zn experiment were 200 ms and 100 μs respectively for radioactive isotopes with relative low yield. There were three accumulation-release cycles for each proton trigger. The logic signals sent to the cooler and data acquisition system are shown in Figure 4.6. For isotopes with high yields, the accumulation time was reduced to prevent the overfilling of the cooler. Taking the ^{68}Zn as an example, the accumulation time was 5 ms. The loading time of the cooler was reduced to 1 ms using a switchable electrostatic deflector (beamgate).

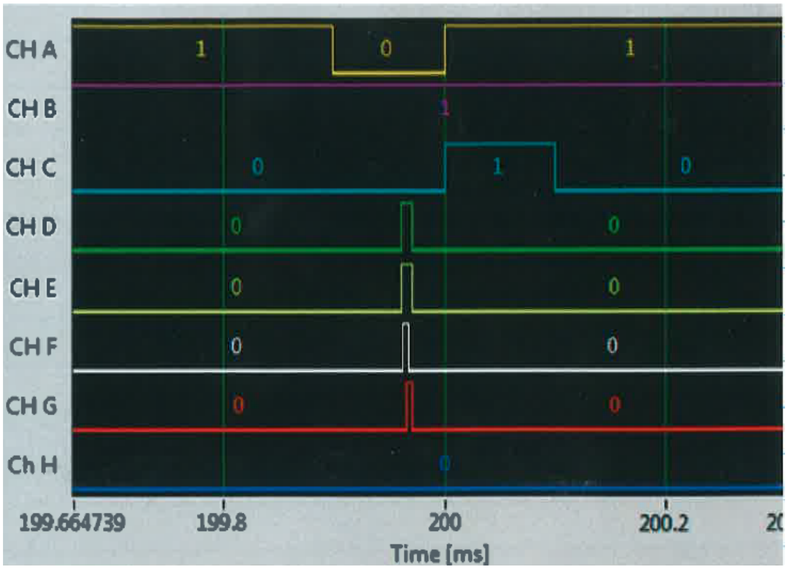

FIGURE 4.6: Oscilloscope screen shot showing the signal sent to control the ISCOOL bunch and the data acquisition.
'CH A' is the signal sent to the RFQ of ISCOOL. When the value is 0, accumulated ions are released. The typical setting in the Zn experiment is 200 ms accumulation time and 100 µs release time.
'CH B' controls the beamgate which cuts the ion accumulation to prevent overfilling the cooler.
'CH C' signals the commencement of data acquisition. The signal here is for the next proton pulse.
'CH D-G' are the time gates corresponding to the period that the bunched beam passes through photon detection region. D and E are longer time gates of 10 µs while F and G are shorter time gates of 5 µs. The delays from E to D and from G to F are 1 µs and compensate the distance (flight time) between the first and second row of PMTs.

4.3 Analysis

4.3.1 Fitting of Data

4.3.1.1 Conversion of Tuning Voltage to Frequency

Prior to the analysis of the spectra, the voltage associated with each point in the scan was converted to frequency. The total voltage is the combination of the cooler voltage, Fluke voltage and scanning voltage.

$$U_{tot} = U_{cool} - (U_{fluke} + kp * U_{kepco}) \tag{4.1}$$

where the kp is the amplification factor which can be determined by a calibration scan of actual voltage applied on the charge exchange cell against live voltage sent by the DAC. Based on the Doppler formula, the conversion is

$$\nu = \nu_0 \times (1 + \alpha \mp \sqrt{2\alpha + \alpha^2}) \tag{4.2}$$

where,

$$\alpha = \frac{eU_{tot}}{mc^2}. \tag{4.3}$$

The minus/plus sign is for collinear or anti-collinear overlap of ion/atom beam and laser. The data for atomic mass m from [31] were used in both Zn and later Ni analysis. The precision of the atomic mass is of the order of 10^{-6} u. Taken U as 30 keV and m as 60 u, the factor α is approximately 0.5×10^{-6}. Since the contribution of m towards α is of the order of 10^{-17}, the uncertainty of m was neglected in the analysis.

4.3.2 The Fitting Function

The A, B atomic factors and isotope shifts (IS) were determined using a minimum χ^2 estimation. Assuming $f(\nu; A(^3S_1), A(^3P_2)\ldots)$ is the fitting function and N_i the counts at frequency ν_i, the fitting process is to find the value of parameters to minimize the χ^2 as

$$min(\sum_i [\frac{f(\nu_i; A(^3S_1), A(^3P_2), \ldots) - N_i}{\epsilon_N}]^2) \tag{4.4}$$

where the ϵ_N is the statistical error on the number of count in channel i and is estimated using $\sqrt{N_i}$. To avoid zero in the denominator for channels of zero count, the error is made up as $\sqrt{0.5}$.

4.3.3 Parameters Related to Asymmetry

As shown in Figure 4.5, the level $4s4p\ ^1P_1$ at 46745.4 cm^{-1} and level $4s5s\ ^3S_1$ at 53672.3 cm^{-1} are populated in the neutralisation process and later decay to ground or triplet-P states. As $^1P_1 \rightarrow ^3 P_{2,1,0}$ transition is strongly hindered due to same parities (the valence electrons of both configurations occupy $4s4p$), the increased population of $^3P_2$ (lower state of resonant excitation) is mainly attributed to the decay from $4s5s\ ^3S_1$ state. The process is

$$\mathrm{Zn}^+ + \mathrm{Na} + KE \rightarrow \mathrm{Zn}(^3S_1) + \mathrm{Na}^+ \rightarrow \mathrm{Zn}(^3P_2) + \mathrm{Na}^+ + 2.6\ \mathrm{eV}$$

where KE is the kinetic energy required for energy conservation. As discussed in Section 2.3.2 the extra acceleration voltage is needed to compensate the loss of kinetic energy resulting in a satellite peak.

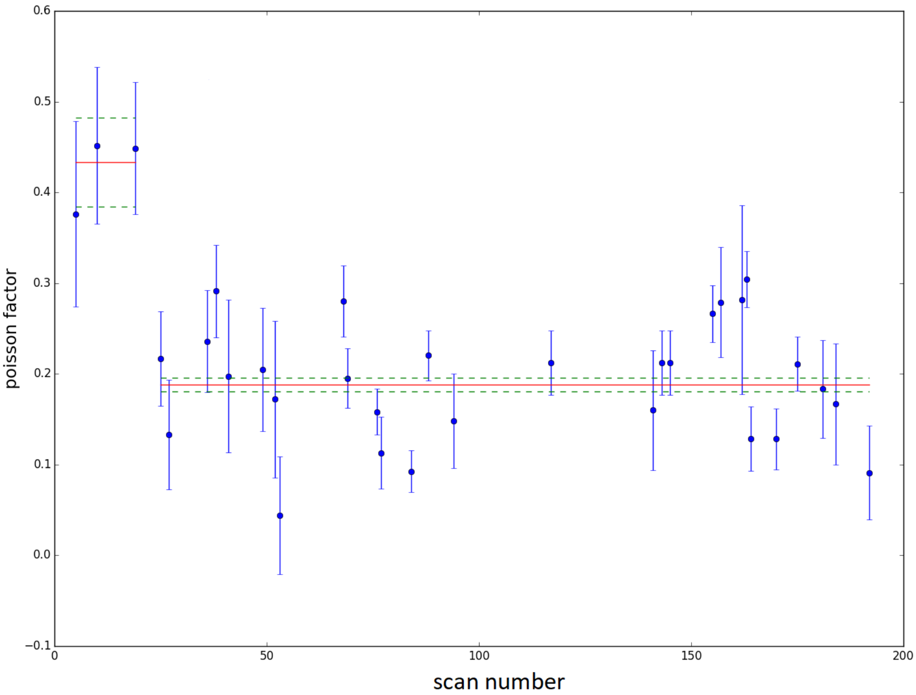

FIGURE 4.7: The average number of collisional excitations from the fitting of selected ^{68}Zn. The value is higher for the spectra of earlier scans, corresponding to a higher CEC temperature.

It was assumed that the asymmetry of the line shape would remain the same if the conditions of the experiment were kept constant. Hence the parameters related to asymmetry could be fixed to simplify the fitting process. For spectra with low statistics such an assumption is necessary. Spectra of ^{68}Zn with high statistics were selected to empirically determine the values. The selected spectra were fitted with two satellite peaks for which the intensities followed a Poisson distribution. In this model, there are two parameters defining the asymmetry: the compensation energy noted as δ, and the average number of collisional excitations λ in Equation 2.27. The δ should be constant and as discussed in the last paragraph is fixed at 2.6 eV. The λ varies if the temperature of the CEC changes. The fitting results of selected spectra are presented in Figure 4.7.

4.3.4 Fitting Processes and the Results

4.3.4.1 Even-A Isotopes

The even isotopes of Zn have 0 spin hence only a single resonance peak was observed. The isotope shifts can be easily seen as demonstrated in Figure 4.9.

There is a drift to the centroid of ^{68}Zn throughout the experiment. The drift could be caused by unnoticed shifts of laser frequency or acceleration voltage. Since only the relative frequency is of interest, the spectra of ^{68}Zn were taken as reference. The $\nu^{A,68}$ was calculated using the nearest scanning of ^{68}Zn.

The spectra of $^{70-78}$Zn had high statistics however the fitting showed that the errors calculated by $\sqrt{N}$ were utterly underestimated. The explanation is that the uncertainty caused by the fluctuations of ion beam intensity or laser power had been overlooked. The error was modified by adding an extra term which is proportional to the counts as $a * N$. The proportionality factor a is small. Therefore when N is small, the second term can be neglected with the dominance

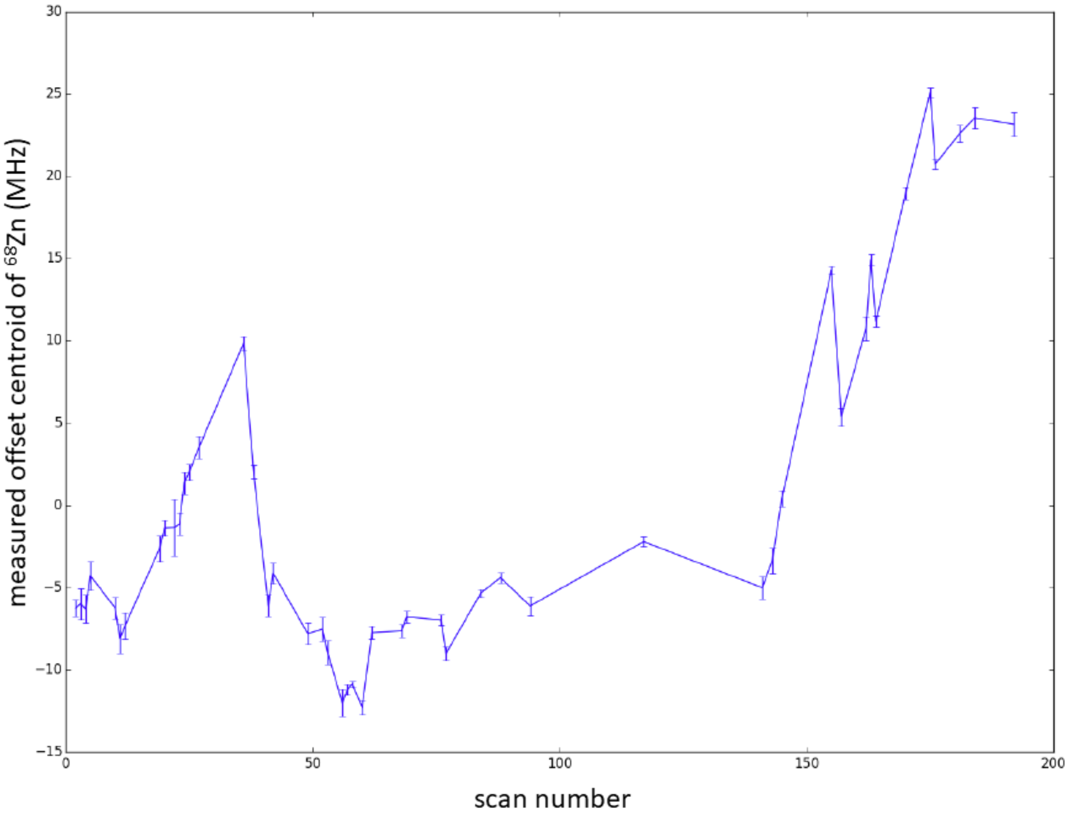

FIGURE 4.8: Measured offset centroid of ^{68}Zn throughout the experiment.

of the first term. Due to the lack of knowledge on a, a group of trial values covering the range (0,1) was tested, leading to the one with reduced χ^2 closest to 1.

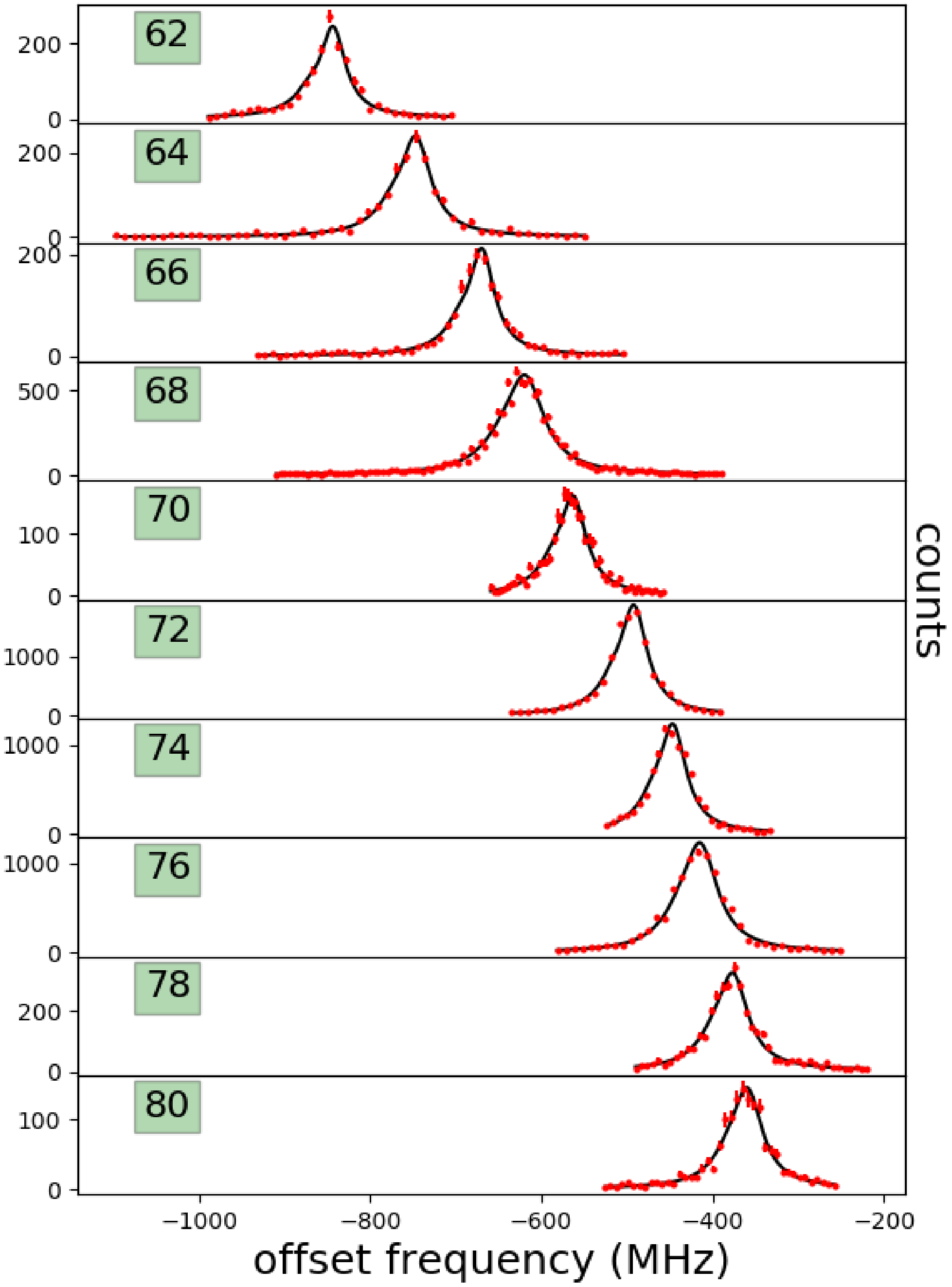

FIGURE 4.9: The spectra of the even Zn isotopes. The isotope shift is obvious as the frequency of single resonance shifts from isotope to isotope.

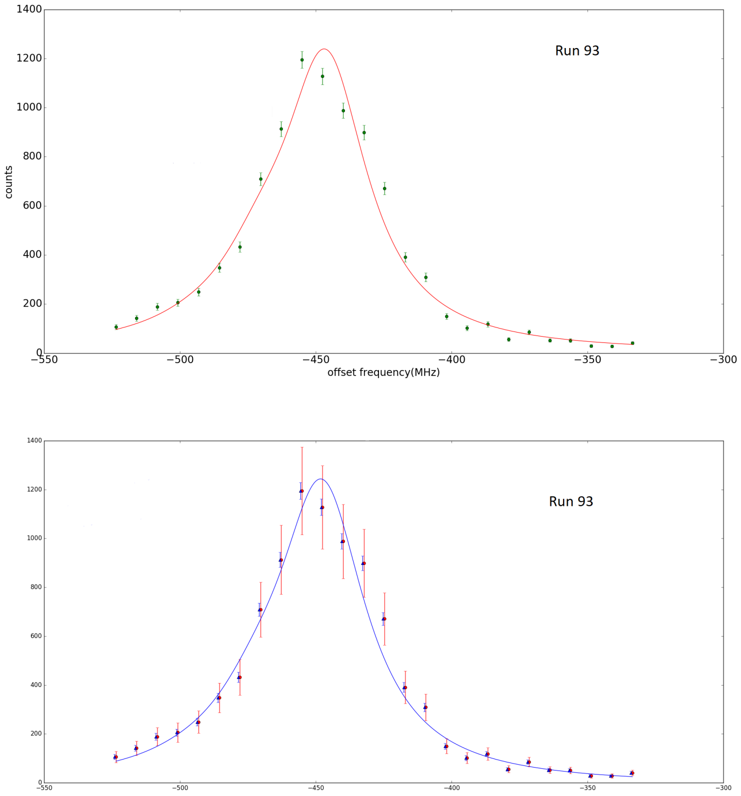

FIGURE 4.10: The spectrum of ^{74}Zn with errors calculated from $\sqrt{N}$ (top) and $\sqrt{N} + a * N$ (bottom).

4.3.4.2 Odd-A Isotopes

A	63	65	67	69	69m	71	71m	73	73m	75	75m	77	77m	79	79m
spin	3/2	5/2	5/2	1/2	9/2	1/2	9/2	(1/2)	(5/2)	(7/2)	(1/2)	(7/2)	(1/2)	(9/2)	(1/2)
	✓	✓	✓	✓	✓	✓	✓	✓	✓	✓	✓	✓	✓	✓	✓

TABLE 4.2: The spins of Zn isotopes. Values are taken from online databases such as the online nuclear chart of IAEA or NNDC. The spins with parentheses mean the value had not been verified. The ticks mean the value was confirmed by this work.

Hyperfine structure was observed in the spectrum of each odd isotope due to the non-zero spin (Figure 4.9). Possible values of the spins were taken from on-line databases such as IAEA[32] or NNDC[33]. In some cases, the spin can be simply determined by the number of peaks. For example, the the ground state of ^{73}Zn has a spin of 1/2 hence a three-peak hyperfine structure. The relative positions and relative intensities of peaks could also be used to identify the spin. Even though the relative heights do not strictly follow the prediction of the Wigner-Eckart theorem, perhaps due to laser pumping effects, the prediction is still a useful tool. Examples of observed spectra of odd Zn isotopes are shown in Figure 4.11 and 4.12.

Isomers were observed in the spectra of ^{69}Zn and heavier odd isotopes. The spectra of odd-A Zn isotopes are presented in Figure 4.11 and 4.12. The masses used in voltage-frequency conversions were modified to compensate for the very small difference in masses of the isomers. For example ^{79m}Zn has an excitation energy 1.1 MeV and the modification of mass shifts the centroid by 3 MHz.

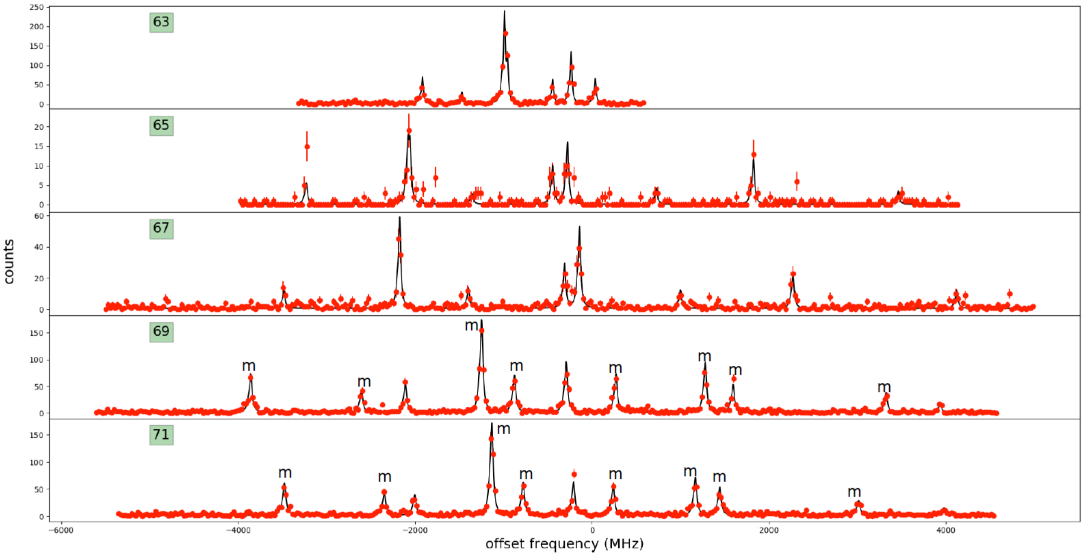

FIGURE 4.11: Hyperfine structures of ^{63,65,67,69,71}Zn. The resonant peaks of isomers are marked with 'm'.

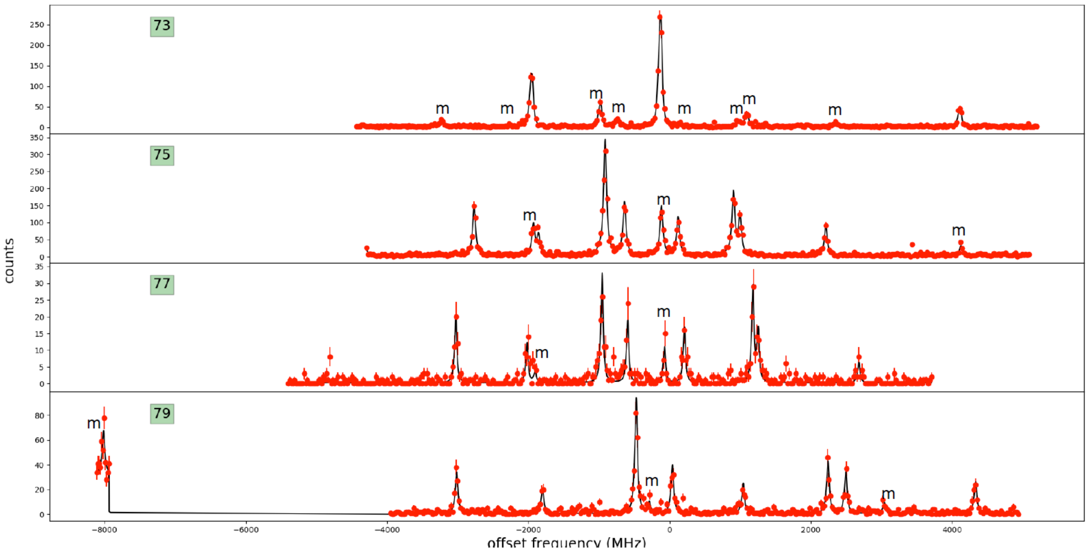

FIGURE 4.12: Hyperfine structures of ^{73,75,77,79}Zn. The resonant peaks of isomers are marked with ‘m’.

For ^{73}Zn, there were 10 accumulation periods which are 10 ms after each proton pulse. Since the half-life of the isomer of ^{73}Zn is 13 ms, the proportion of $^{73\mathrm{m}}$Zn decreases rapidly in the later accumulation periods. In order to increase the relative intensity of $^{73\mathrm{m}}$Zn, a gate (shown in Figure 4.13) was applied to select the counts only from the first two accumulation times after the proton pulse. The comparison between the result of gated and non-gated counting is shown in Figure 4.14. Strictly speaking, the set-up of this experiment can not distinguish the ground state from isomer. However in some special cases such as ^{73}Zn, the lifetime of the isomer is short enough that the intensity decay can be observed.

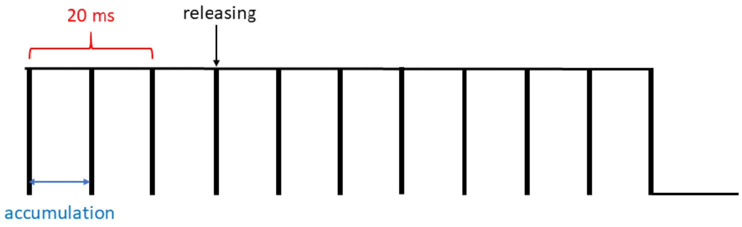

FIGURE 4.13: Gate applied on the data acquisition for ^{73}Zn. Only the first two out of the ten accumulations were recorded.

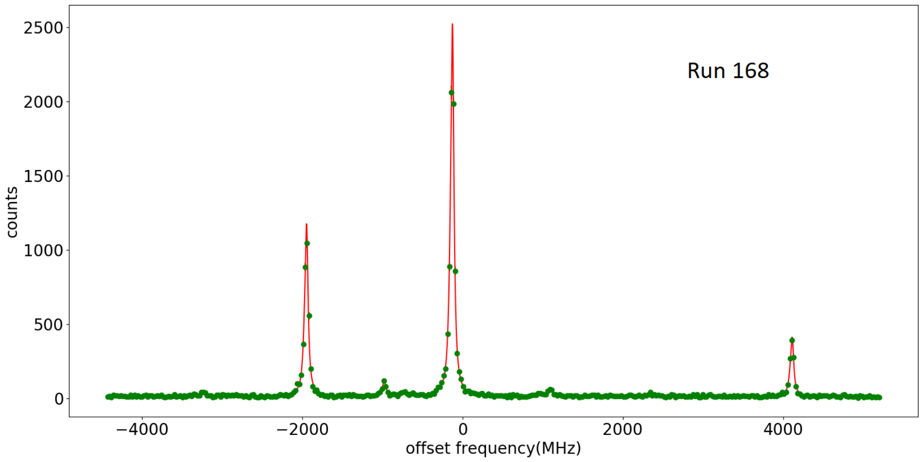

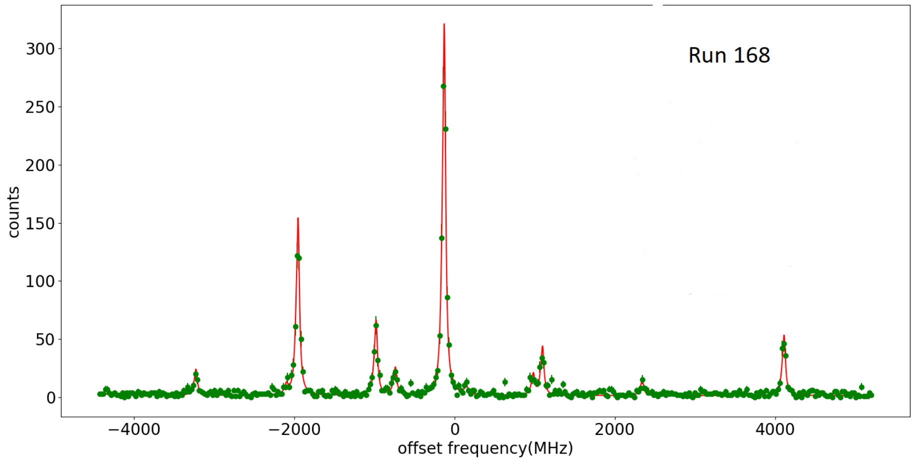

FIGURE 4.14: upper: The spectrum of ^{73}Zn without gate on the accumulation periods; lower: The spectrum of ^{73}Zn with a gate selecting only the first two accumulation periods of 10 ms.

Often in the fitting, the wrong spin would lead to a terrible fitting result as most of the hyperfine structure is missed by the fitting process. There is another way to verify the spin: based on the Equation 2.12, the ratio between the A factors of upper and lower states is

$$\frac{A_u}{A_l} = \frac{B_u J_l}{B_l J_u} \tag{4.5}$$

where B_u/B_l is the magnetic field generated by shell electrons at the position of nucleus. The ratio is constant across an isotope chain (if the small hyperfine anomaly is neglected) only when fitting with the right spin (see Figure 4.15).

The A, B factors and isotope shifts extracted from fittings are list in Table 4.3 and 4.5.

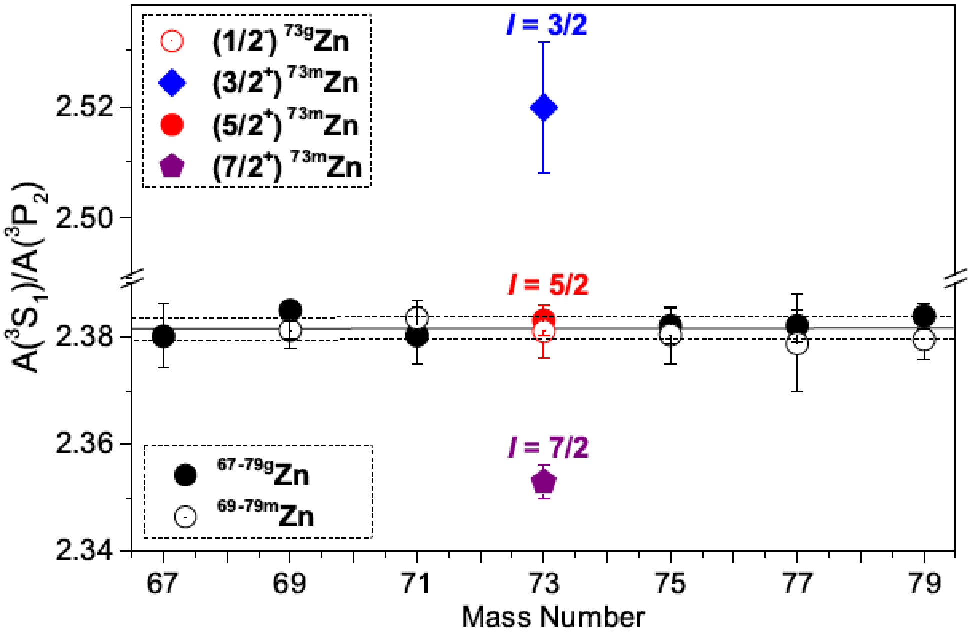

FIGURE 4.15: The A_u/A_l for Zn isotopes [11]. Different possible pins were tried on $^{73\mathrm{m}}$Zn while only $I = 5/2$ produces the ratio consistent with the average value.

mass number	$A(^3S_1)$(MHz)	$A(^3P_2)$(MHz)	$B(^3P_2)$(MHz)
63	-676.9(11)	-286.7(8)	62.3(27)
65	1115.3(47)	467.7(28)	-3.1(310)
67	1267.49(76)	530.66(46)	36.0(41)
69	4030.2(10)	1691.3(7)	
69m	-933.7(2)	-392.1(2)	-111.2(21)
71	3987.2(38)	1674.6(20)	
71m	-843.7(5)	-354.0(3)	-75.8(76)
73	4042.7(16)	1696.1(10)	
73m	-1234.2(14)	-518.2(9)	126.2(19)
75	-815.2(11)	-342.1(3)	46.9(160)
75m	4035.9(30)	1695.9(17)	
77	-937.7(4)	-393.8(4)	141.3(34)
77m	4067.2(6)	1708.5(14)	
79	-954.41(2)	-400.7(3)	115.7(50)
79m	-7370.5(31)	-3090.9(29)	

TABLE 4.3: Atomic factors of Zn isotopes.

4.3.5 The Mean Square Charge Radii Calculation

Based on Equation 2.9, the $\delta\langle r^2\rangle$ can be calculated from the measurement of the isotope shift if the atomic factors F and K are known. The atomic factors are either determined using experimental data, using a King plot method, or through some theoretical atomic calculation such as using a multi-configurational Dirac-Fock calculation.

A	$R^{\mu}_{k\alpha}$ (fm)	$\delta\langle r^2\rangle^{A,68}_{\mu e}$ (fm^2)	$\delta\langle r^2\rangle^{A,68}$ deformation modified (fm^2)
64	5.0333(7;22)	0.301(5;19)	0.287(4)
66	5.0598(7;21)	0.149(5;18)	0.129(3)
68	5.0814(5;21)	0	0
70	5.1046(15;22)	-0.159(9;19)	-0.148(8)

Table 4.4: The available Barrett radii for Zn isotopes. The data are quoted from [13]. The smaller error in the parentheses is derived from the error of the experimental transition energies in muonic atom measurements. The second error includes the effect of nuclear polarization. The $\delta\langle r^2\rangle^{A,68}_{\mu e}$ is the derived from $R^{\mu}_{k\alpha}$. The $\delta\langle r^2\rangle$ were further modified by deformation factors from Coulomb excitation [34]. The modified results are listed in the last column.

Let $\mu = \frac{m_{A'} m_A}{m_{A'-A}}$ and define

$$\mathcal{V} = \delta\nu^{A,A'} * \mu \qquad \text{and} \qquad \mathcal{R} = \delta\langle r^2\rangle^{A,A'} * \mu$$

$\mathcal{V}$ and $\mathcal{R}$ are modified isotope shifts and modified relative mean square charge radii. Hence Equation 2.9 can be transferred into a linear function as

$$\mathcal{V} = F * \mathcal{R} + K. \tag{4.6}$$

The $\delta\nu^{A,A'}$ are measured in different spectroscopy experiments while the $\delta\langle r^2\rangle^{A,A'}$ of stable isotopes usually can be derived from Barrett's equivalent radius obtained in the electron scattering and muonic atom experiments. If there are three or more available $\delta\langle r^2\rangle^{A,A'}$, then the F, K factors can be extracted from a linear fitting. The process is called the King plot method.

In an alternative King plot method, the Equation 4.6 of two transitions (indicated by subscription 1 and 2) can be combined into

$$\mathcal{V}_1 = \frac{F_1}{F_2}\mathcal{V}_2 - \frac{K_2}{F_2}F_1 + K_1. \tag{4.7}$$

$\mathcal{V}_1$ is a linear function of $\mathcal{V}_2$. If the F_2 and K_2 are known, again the value of F_1 and K_1 can be extracted from the plot of $\mathcal{V}_1$ against $\mathcal{V}_2$ through a linear fitting.

The Barrett's equivalent radii of ^{64,66,68,70}Zn have been derived from muonic atom experiments. They are transferred into $\delta\langle r^2\rangle^{A,68}_{\mu e}$ (listed in Table 4.4) using ratios of radial moments derived from electron scattering data [13]. The values are then used in the King plot shown in the upper figure of Figure 4.16. As the plot demonstrates, the values of $\delta\langle r^2\rangle^{A,68}_{\mu e}$ are so inaccurate that some refinement is necessary for a reliable King plot to be performed. Detailed in [34], a deformation modification was done on the $\delta\langle r^2\rangle$ using deformation factors from Coulomb excitation experiments. The improved King plot is shown in the lower figure of Figure 4.16. The F from this King plot is $(4.0 \pm 2.1) \times 10^2$ MHz $\cdot$ fm^{-2}. The errors on the atomic factors are too big to serve any practical purpose. The recent development in multi-configurational Dirac-Fock calculation makes the theoretical calculation of F available. The calculated value of F was used as a prior probability with 10% uncertainty. This additional restriction on F dramatically reduced the error on the extracted atomic factors as is now discussed.

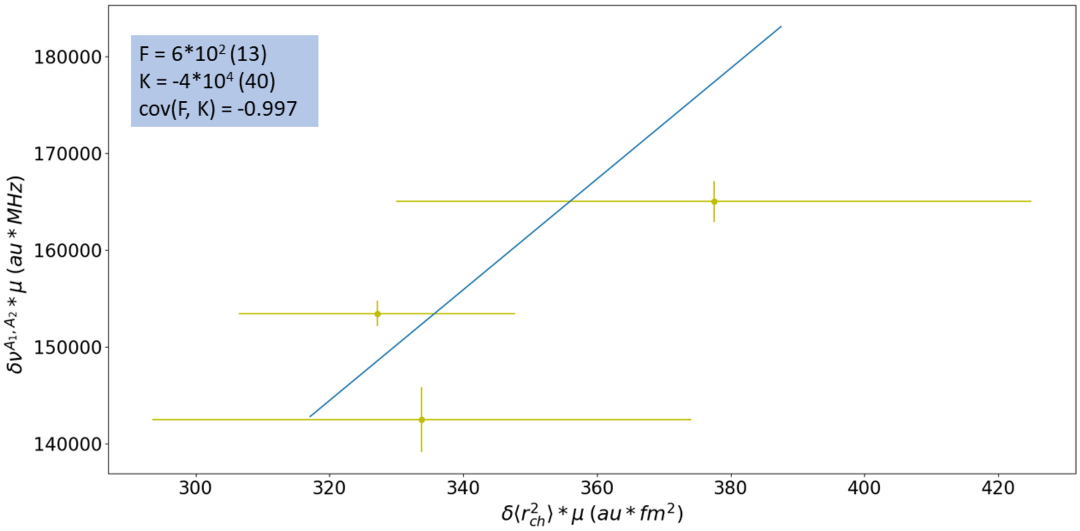

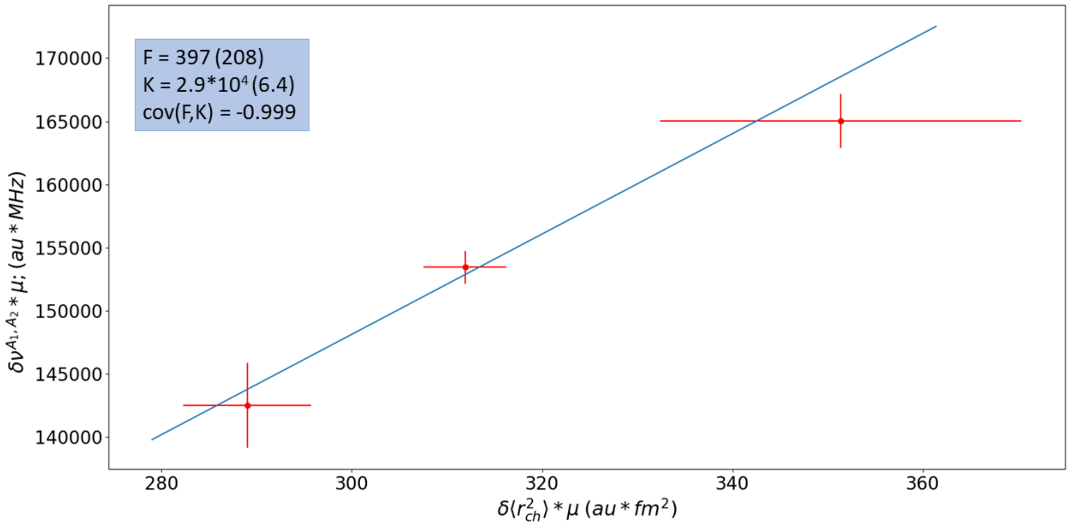

FIGURE 4.16: (top) The King plots of Zn using $\delta\langle r^2\rangle$ derived from electron scattering and muonic atom experiments (the third column of Table 4.4; (bottom) The King plots of Zn using deformation modified $\delta\langle r^2\rangle$ (the last column of Table 4.4.

4.3.5.1 The Estimation of F, M Derived from a Zn King plot

Let vector $\boldsymbol{x}$ be the observation of a group of events. The value of $\boldsymbol{x}$ is related to $\boldsymbol{\theta}$, the vector of parameters. In physics experiments, $\boldsymbol{x}$ represents the measurement, while $\boldsymbol{\theta}$ is a series of parameters intended to be determined through the measurement. The process of finding the $\boldsymbol{\theta}$ corresponding to the maximum probability with given observation $\boldsymbol{x}$ is called Maximum a Posteriori Estimation (MAP). According to Bayes' theorem of probability

$$P(\boldsymbol{\theta}|\boldsymbol{x}) = \mathcal{L}(\boldsymbol{x}|\boldsymbol{\theta}) \times \frac{P(\boldsymbol{\theta})}{P(\boldsymbol{x})}. \tag{4.8}$$

The $P(\boldsymbol{x}|\boldsymbol{\theta})$ is the probability of $\boldsymbol{x}$ given parameter $\boldsymbol{\theta}$. It is also called the likelihood of $\boldsymbol{x}$, which is a function of $\boldsymbol{\theta}$. The term $\frac{P(\boldsymbol{\theta})}{P(\boldsymbol{x})}$ is called prior probability representing the probability distribution of $\boldsymbol{x}$ and $\boldsymbol{\theta}$ known before the observation is taken. $P(\boldsymbol{x})$ is the probability of the data averaged over all possible $\boldsymbol{\theta}$. Since $P(\boldsymbol{x})$ is independent of $\boldsymbol{\theta}$, usually it is considered as a normalizing constant to ensure that the sum of probability is equal to 1. $P(\boldsymbol{\theta})$ is the probability of $\boldsymbol{\theta}$ prior to $\boldsymbol{x}$. The value could be obtained using different methods independent of the $\boldsymbol{x}$. If there is no knowledge of $P(\boldsymbol{\theta})$, it is regarded as an uniform distribution. This special case is equivalent to the maximum likelihood estimation. The maximization of a non-negative function is equivalent to the maximization of the logarithm of the function. Because it is more convenient to work with the natural logarithm of likelihood, called log-likelihood, in many applications, the Equation 4.8 is often transferred into

$$\ln P(\boldsymbol{\theta}|\boldsymbol{x}) = \ln \mathcal{L}(\boldsymbol{x}|\boldsymbol{\theta}) + \ln \frac{P(\boldsymbol{\theta})}{P(\boldsymbol{x})}. \tag{4.9}$$

The key to the maximization of Equation 4.8 or 4.9 is to find the expression of $\mathcal{L}(\boldsymbol{x}|\boldsymbol{\theta})$. The assumption is made that the measurement follows a multivariate Gaussian distribution as

$$G(\boldsymbol{x}) = \frac{exp(-\frac{1}{2}(\boldsymbol{x}-\boldsymbol{\mu})^T\boldsymbol{\Sigma}^{-1}(\boldsymbol{x}-\boldsymbol{\mu})}{\sqrt{(2\pi)^k|\boldsymbol{\Sigma}|}}. \tag{4.10}$$

Equation 4.10 is a generalization of a one-dimension normal distribution to the k dimension where $\boldsymbol{\mu}$ is the mean and $\boldsymbol{\Sigma}$ is the covariance matrix. The mean can be replaced by the prediction of some physics equation of parameters $\boldsymbol{\theta}$, as

$$\mathcal{L}(\theta|x) = G_\theta(\boldsymbol{x}) = \frac{exp\big(-\frac{1}{2}(\boldsymbol{x}-f(\boldsymbol{\theta})\big)^T\boldsymbol{\Sigma}^{-1}\big(\boldsymbol{x}-f(\boldsymbol{\theta})\big)}{\sqrt{(2\pi)^k|\boldsymbol{\Sigma}|}}. \tag{4.11}$$

Taking a one-dimension measurement as an example, the likelihood function is

$$\mathcal{L}(x|\boldsymbol{\theta}) = G_\theta(x) = \frac{1}{\sqrt{2\pi\sigma^2}} e^{-\frac{(x-f(\boldsymbol{\theta}))^2}{2\sigma^2}} \tag{4.12}$$

Hence the log-likelihood is

$$\ln \mathcal{L}(\theta|x) = -\frac{(x-f(\boldsymbol{\theta}))^2}{2\sigma^2} + \ln \frac{1}{\sqrt{2\pi\sigma^2}}. \tag{4.13}$$

The $\ln \mathcal{L}(\theta|x_1, x_2, \cdots, x_n)$ for n independent measurements is simply

$$\ln \mathcal{L}(\theta|x) = -\frac{1}{2}\sum_i^n \frac{(x_i - f(\boldsymbol{\theta}))^2}{\sigma^2} + C. \tag{4.14}$$

Since C is a constant term playing no role in the maximization process, the maximum likelihood estimation is in fact equivalent to a least χ^2 estimation.

In the case of the King plot function Equation 4.6, that observations are the variables $\mathcal{V}$ and $\mathcal{R}$. $\mathcal{R}$ is a function of $\mathcal{V}$ with atomic factors F and K as parameters. The log-likelihood of F and K is

$$-\frac{1}{2}\left[\frac{(\mathcal{R}-\mathcal{R}_0)^2}{\sigma_{\mathcal{R}}^2} + \frac{\big(\mathcal{V}-(F\mathcal{R}_0+K)\big)^2}{\sigma_{\mathcal{V}}^2}\right] + C \tag{4.15}$$

where $\mathcal{R}_0$ is the 'real' value and the first part is the residual on both $\mathcal{R}$ and $\mathcal{V}$ directions. Since only the measured value $\mathcal{R}$ is available, the unknown $\mathcal{R}_0$ adds an extra parameter to be evaluated. In order to simplify the regression process, more constraints are needed. From a geometric point of view, if the error on both $\mathcal{V}$ and $\mathcal{R}$ are the same, the residual is the square of the scaled length between the measured point to a point on the line of function. The least length occurs when the residual line is perpendicular to the line of function. Therefore, the method is also called orthogonal distance regression. Because the errors on $\mathcal{R}$ and $\mathcal{V}$ are different, the distance is weighted according to the errors.

A Gaussian distribution was used as prior probability on field factor F. The mean value $F_0 = 346$ MHz/fm^2 of the Gaussian distribution was from a multiconfiguration Hartree-Fock calculation [35]. A 10% error was assumed empirically The

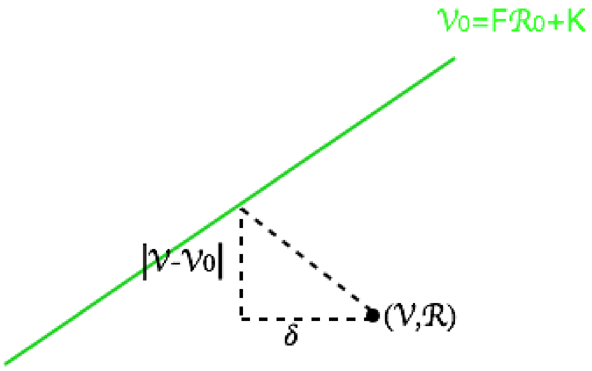

FIGURE 4.17: The figure describes the ‘residual line’ as the vector sum of horizontal residual(δ) and vertical residual.

King plot is shown in Figure 4.18 and the result is

$$F = +348 \pm 34 \text{ MHz/fm}^2, \; K = +44 \pm 11 \text{ GHz} * \text{u}$$

with correlation efficient of $\rho_{(\text{F,K})} = -0.974$.

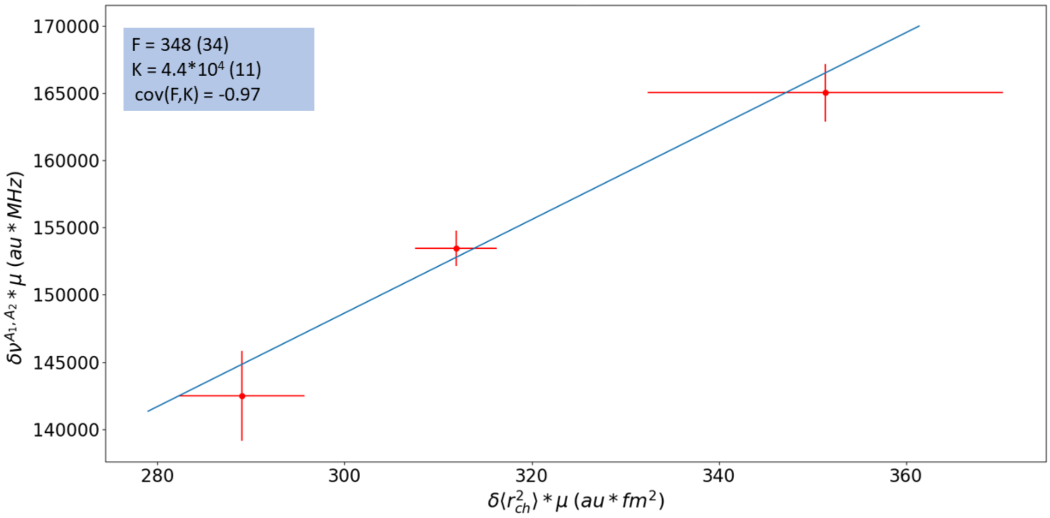

FIGURE 4.18: The King plot of Zn with prior probability on field factor F calculated from multiconfiguration Hartree-Fock method.

4.3.5.2 The Error Analysis of $\delta\langle r^2\rangle$

The statistical errors of isotope shifts are the error from the fitting process. The statistical error of $\delta\langle r^2\rangle$ was derived from the statistical error of the isotope shift using simple error propagation $\sigma^2_{sta(\delta\langle r^2\rangle)} = F^2\sigma^2_{sta(IS)}$.

The major contribution to the systematic error of the isotope shift is the uncertainty of the cooler voltage. Based on previous experience, the uncertainty is within ±10 V. The effect of the ±10 V cooler voltage on an isotope shift is demonstrated in Figure 4.19 and the corresponding systematic errors on the isotope shifts are listed in Table 4.5. The systematic error of the isotope shift causes the variation of F and K (dominated by K) in the King plot. Because both the King plot and the calculation of $\delta\langle r^2\rangle$ in fact use the same Equation 2.9, the variation of atomic factors cancels the variation of isotope shift due to an uncertain cooler voltage in the calculation of $\delta\langle r^2\rangle$. Therefore, the systematic error of the isotope shift does not contribute significantly to the systematic error of $\delta\langle r^2\rangle$ (see Figure 4.19).

The systematic error of $\delta\langle r^2\rangle$ is derived from the errors of F and K obtained from King plot method using

$$\sigma^2_{\delta\langle r^2\rangle} = \big(\frac{\partial f}{\partial F}\big)^2\sigma_F^2 + \big(\frac{\partial f}{\partial K}\big)^2\sigma_K^2 + 2\frac{\partial f}{\partial F}\frac{\partial f}{\partial K}\sigma_{FK}. \tag{4.16}$$

Because the extracted values of F and K are correlated, the covariance σ_{FK} is calculated by $\sigma_{FK} = \sigma_F\sigma_K\rho_{FK}$ where ρ_{FK} is the correlation coefficient which can be obtained from the regression process of the King plot method.

The calculated $\delta\langle r^2\rangle^{68,A}$ of Zn isotopes are listed in Table 4.5. To be noted, M.L. Bissell (University of Manchester), the co-supervisor of the author, suggested the errors of deformation corrected $\delta\langle r^2_{\mu e}\rangle$ from [34] are underestimated since only statistical errors are included. In the Zn charge radii paper which is in preparation the King plot uses the $\delta\langle r^2_{\mu e}\rangle$ without deformation correction. Therefore, the values of $\delta\langle r^2\rangle^{68,A}$ in that paper are different from those listed in Table 4.5.

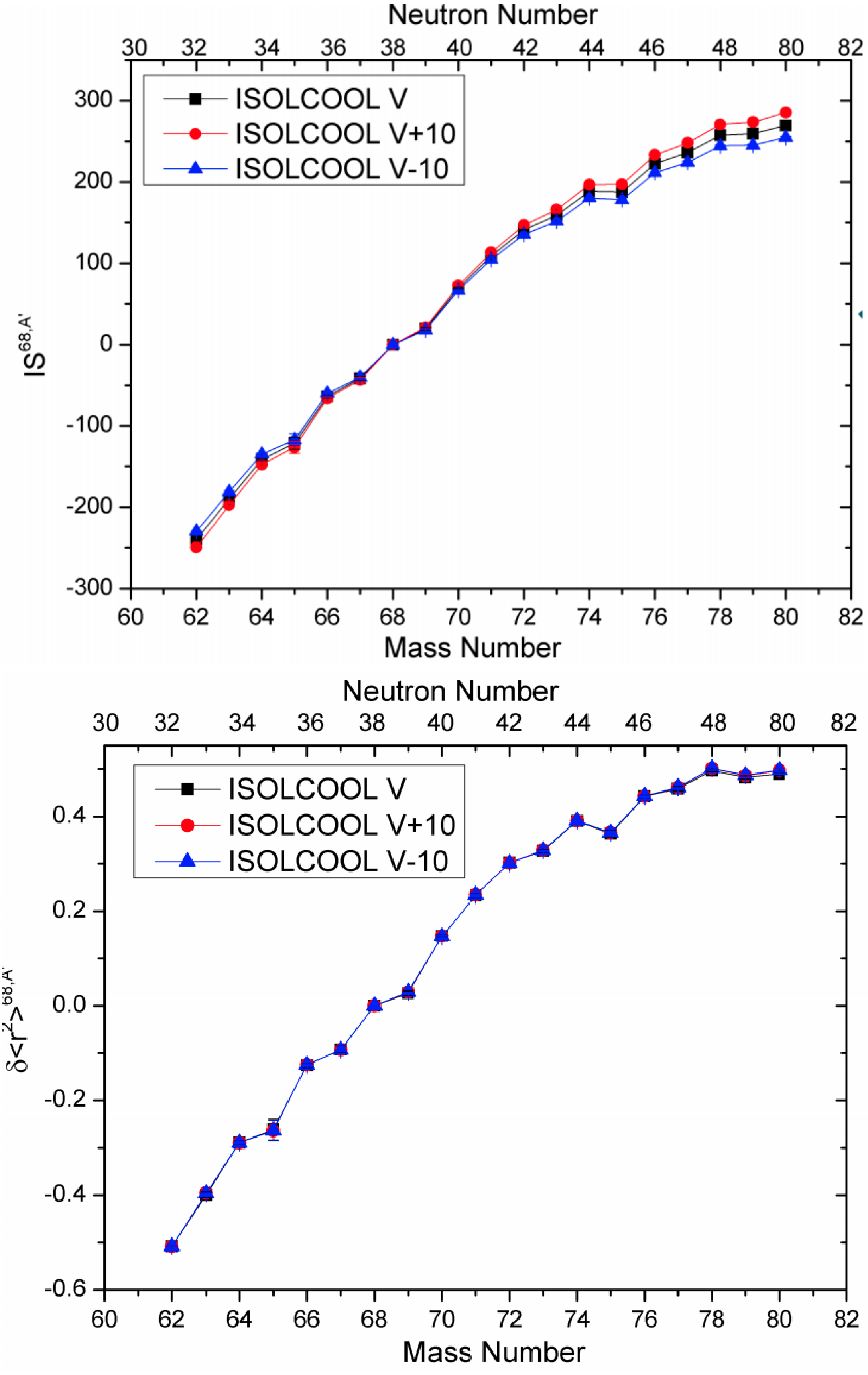

FIGURE 4.19: Top: The variation of isotope shift caused by ±10V cooler voltage; Bottom: The uncertainty of cooler voltage barely has any effect on the $\delta\langle r^2\rangle$ as the atomic factors ‘adjust’ the calculation of $\delta\langle r^2\rangle$.

mass number	isotope shift (MHz)	$\delta\langle r^2\rangle^{68,A}$(fm^2)
62	-239.5(11)[99]	-0.507(3)[12]
63	-192.4(32)[87]	-0.401(9)[9]
64	-140.9(8)[66]	-0.289(3)[7]
65	-121.3(23)[51]	-0.264(7)[7]
66	-63.4(13)[38]	-0.126(4)[3]
67	-41.9(21)[16]	-0.091(6)[3]
68	0	0
69	19.5(18)[15]	0.0288(6)[4]
69m	35.7(10)[15]	0.075(3)[2]
70	69.2(9)[29]	0.146(3)[3]
71	109.0(19)[44]	0.234(7)[6]
71m	96.5(10)[43]	0.198(3)[4]
72	140.1(10)[57]	0.300(3)[7]
73	158.9(12)[71]	0.328(3)[7]
73m	160.7(19)[71]	0.333(5)[7]
74	187.2(13)[83]	0.388(4)[9]
75	187.7(10)[96]	0.364(3)[11]
75m	195.8(21)[96]	0.388(6)[10]
76	220.2(14)[108]	0.439(4)[12]
77	235.9(11)[120]	0.459(5)[14]
77m	241.2(34)[120]	0.474(11)[14]
78	253.8(11)[131]	0.494(3)[16]
79	259.3(7)[142]	0.484(3)[21]
79m	318.4(20)[142]	0.660(8)[15]
80	268.4(12)[161]	0.490(3)[25]

TABLE 4.5: The isotope shift and $\delta\langle r^2\rangle^{68,A}$ for Zn isotopes and isomer. The errors in parentheses are statistical errors. Those in square brackets are systematic errors.

The remainder of this page was intentionally left blank.

Chapter 5

Charge Radii of Nickel Isotopes

5.1 Experiment Setup

The collinear laser spectroscopy experiment on the Ni isotopes was also divided into two runs in 2016 and 2017. The target of the first run was designed specifically to provide higher yield than a standard UC$_x$ target, but it was not up to expectation. Suspecting there was a malfunction in the design, a standard UC$_x$ target was used in the second run. As shown in Table 5.1, the actual yields measured during the both runs were two orders of magnitude lower than expectation. The cooler acceleration voltages were 30 kV and 40 kV in the first and second runs respectively.

A	expected yield (ions/μC)	yield measured during experiment (ions/μC)
66	1×10^8	several $\times 10^5$ (2017 experiment)
69	2×10^4	3.9×10^2 (2016 experiment)

Table 5.1: The expected Ni isotopes yields and the values measured during the two runs. Both expected yields are provided by the target group at ISOLDE from previous measurements of a UC$_x$ target [36]. The target used in the 2016 run was a specially designed for Ni isotopes.

The magnetic dipole and electric quadrupole moments of Ni isotopes from previously published moments are listed in Table 5.2. The $\delta\langle r^2\rangle_{e\mu}$ evaluated from muonic atom and electron scattering experiments (Table 5.3) will be used in a King plot to extract the atomic factors.

isotope	μ(nm)	Q(b)
57	-0.7975(14)	
61	-0.75002(4)	+0.162(15)
65	0.69(6)	
67	+0.601(5)	

TABLE 5.2: The magnetic dipole and electric quadrupole moments of Ni isotopes from the literature [37]. The sign of the ^{65}Ni magnetic moment was not known.

pair	$\delta\langle r^2\rangle^{60,A}_{e\mu}$(fm^2)
58-60	-0.2709(58)
61-60	0.0834(63)
62-60	0.2243(59
64-60	0.3597(59)

TABLE 5.3: The $\delta\langle r^2\rangle^{60,A}_{e\mu}$(fm^2) from muonic atom and electron scattering experiments [13].

The transition studied in this experiment is from the metastable $3d^94s\ ^3D_3$ lower level to $3d^94p\ ^3P_2$ upper level as demonstrated in Figure 5.1. According to [38], the lifetime of the upper state ($^3P_2$) is 13.2 ns. The branching ratio to the $^3D_3$ is 88% leading to a transition probability of 6.6×10^7 s^{-1}. The large transition probability is necessary for a good fluorescence efficiency. Because it is an s state to p state transition, it is sensitive to the charge radii changes of the nuclei (large field shift factor F). The atomic factors of the level $3d^94s^1\ ^3D_3$ of ^{61}Ni have been published [39]:

$$A = \text{-455 MHz},\ B = \text{-103 MHz}$$

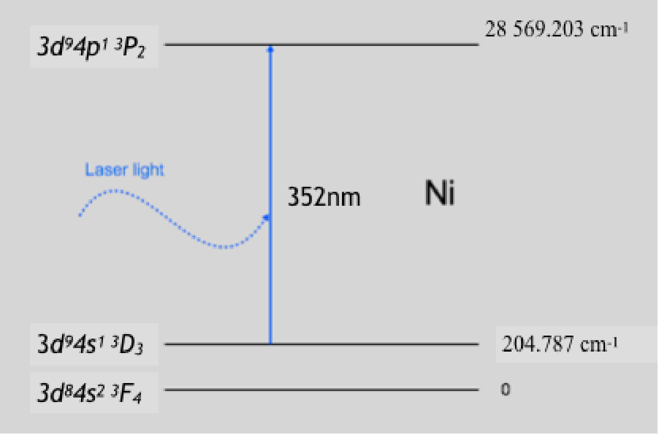

FIGURE 5.1: The transition studied in the collinear laser spectroscopy of Ni.

Sodium was used as the charge exchange material. Ryder *et al* [40] studied the neutralization reaction of 29.85 keV Ni^+ impinging on Na vapour and their simulation demonstrated the population distribution (Figure 5.2). The entry energy is defined by the Na ionization energy. If the difference between the energy level of the Ni atom and the entry energy is ΔE (such as in the Zn neutralisation process in Figure 4.4), then energy levels with small ΔE should be well-populated immediately following the charge exchange reaction. The low-lying states including the lower state in the transition $3d^9 4s\ ^3D_3 - 3d^9 4p\ ^3P_2$ are populated from the subsequent decay from states around 30,000 cm^{-1}.

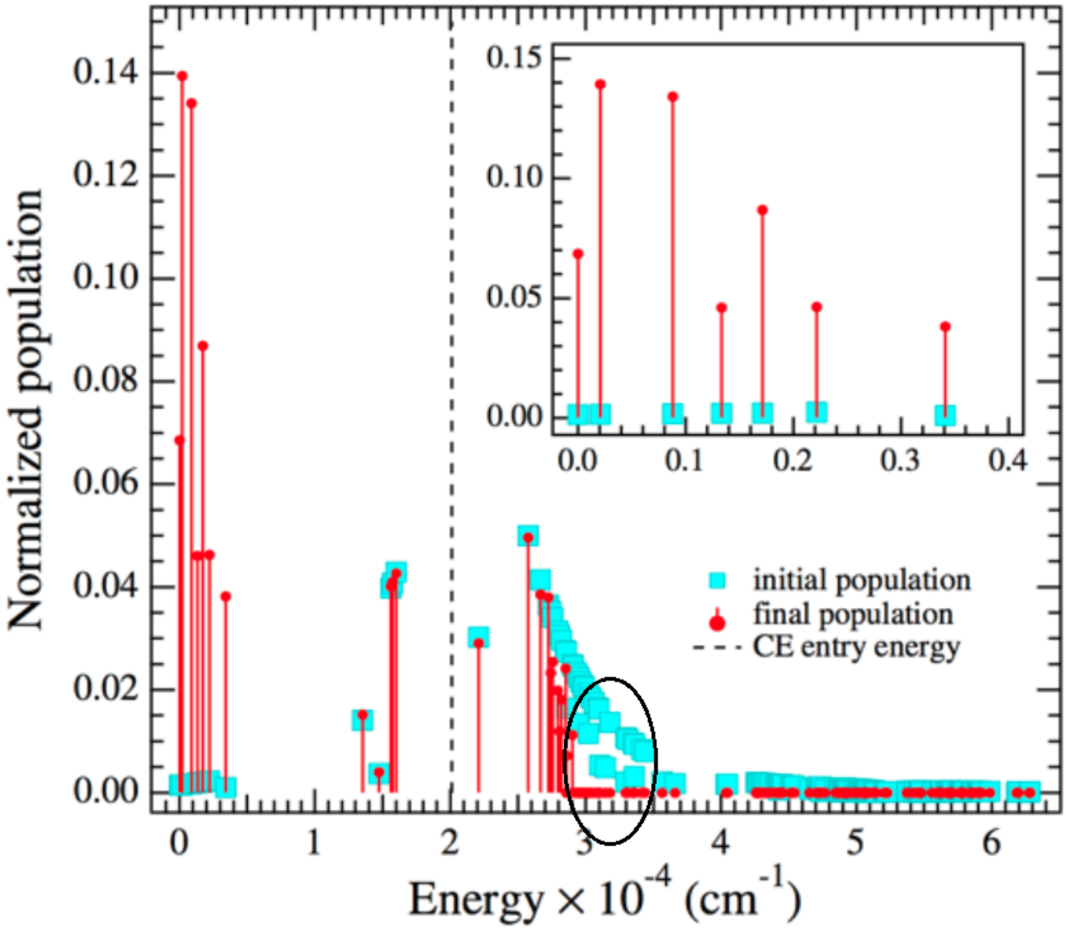

FIGURE 5.2: Simulated population of Ni after neutralization by sodium vapour. The states encircled are those responsible for most of the population of the lower level (204 cm^{-1}) used in the experiment [40].

The resonant radiation at 352 nm was provided by a Matisse laser with a Titanium-doped Sapphire (Ti:Sa) crystal installed. The frequency of the laser was doubled by a WaveTrain cavity. The wavenumber of the laser was different in the two runs, 14,196.5 cm^{-1} in the first run and 14198.6 cm^{1} in the second because of the different cooler voltages. A HeNe laser and a CoSy (mentioned in Section 3.6.3.2) were used as external frequency reference for long-term stabilization in first and second runs respectively .

A new data acquisition system called TILDA had been developed by one of the students in the collaboration, Simon Kaufmann (Mainz University). In addition to recording the scanning voltage, TILDA also recorded the time between the release of the bunched beam and the detection of each photon. The time profile of the bunched beam could be used to check whether the cooler was overfilled. Moreover it provided more freedom to set the time gate or to refine it in off-line analysis. Figure 5.3 demonstrates the structure of the TILDA data. The projection of the counting to the time axis gives the time profile of bunched beam. Figure 5.4 is an example of the time profile of a ‘normal’ bunched beam and one with overfilled cooler.

TILDA was tested in the first run of the Ni experiment by working in parallel with the old measurement control program (MCP) system. It was used without MCP backup in the second run.

The rest of the setup of the beamline was the same as the Zn experiment.

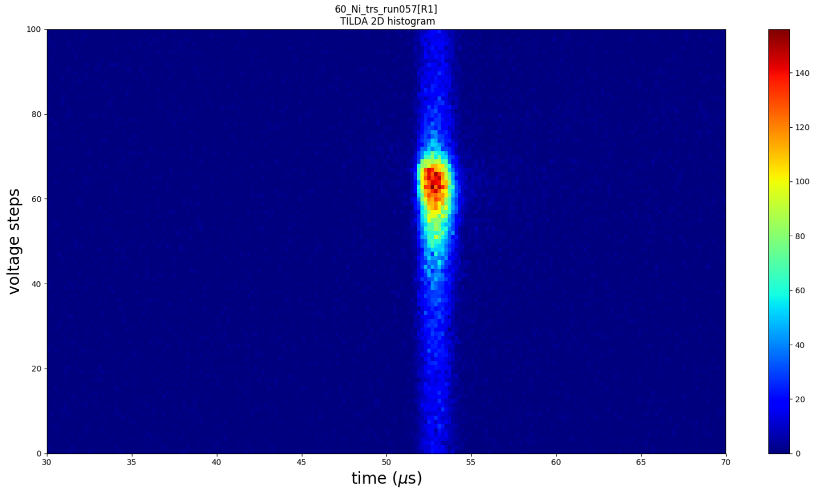

FIGURE 5.3: Example of TILDA data structure.

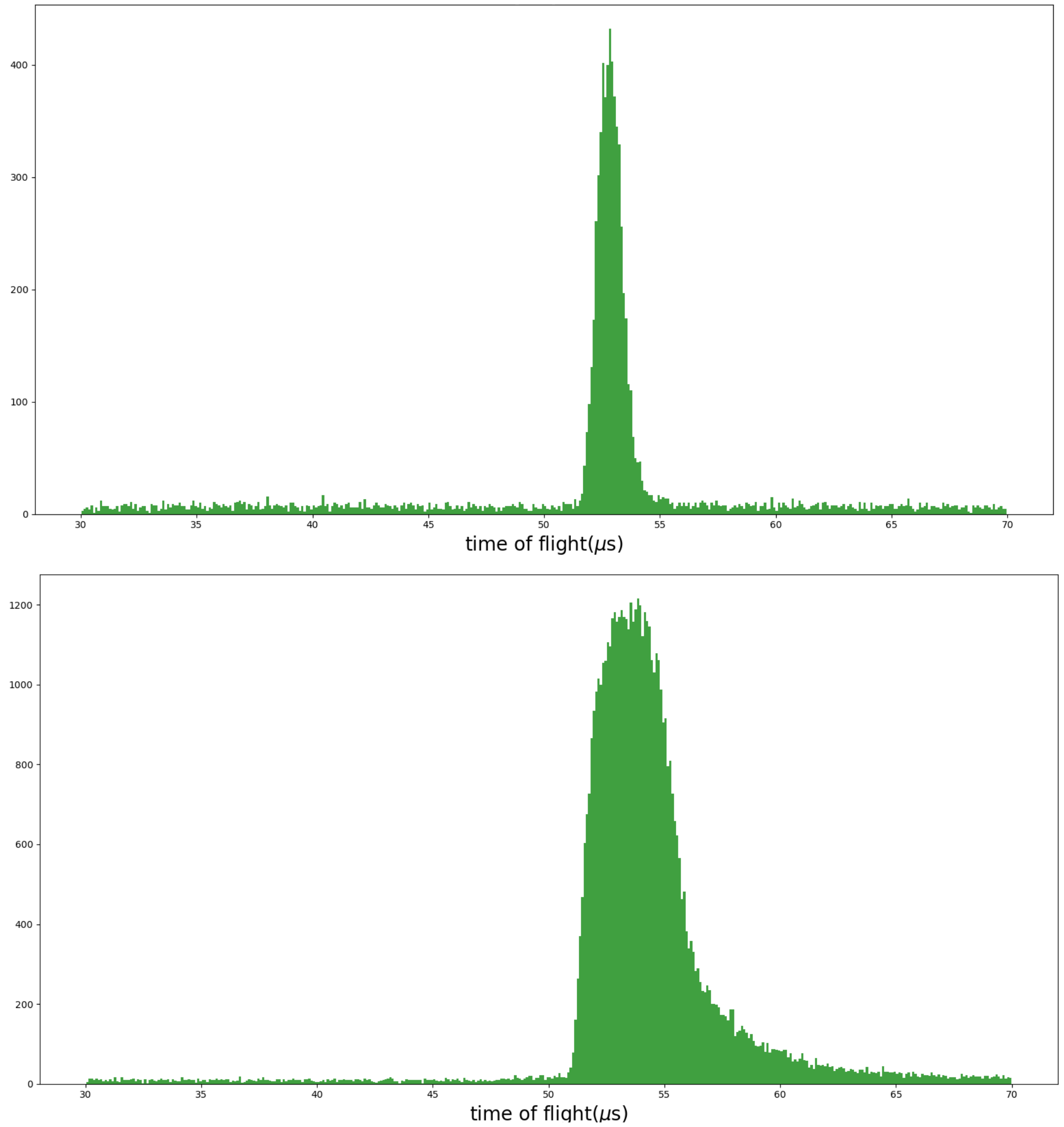

FIGURE 5.4: upper: The time profile of a normal bunched beam recorded by TILDA; lower: the time profile of an overfilled bunched beam recorded by TILDA.

5.2 Analysis

The time profile extracted from the data of TILDA was used to rule out the measurements with an overfilled cooler. Single-peak spectra of even isotopes with good statistics were selected to explore the lineshapes of the peaks. The peaks were found to be asymmetric. As explained in the previous chapter, the asymmetry can only be described empirically. Different models were tested. The optimum parameters describing the asymmetry were fixed or given constraints.

This simplified the fitting process and became necessary for measurements with low statistics.

The King plots were made separately for each run due to the uncertainty of the cooler voltages. The value of factors F and particularly K extracted from the King plots are specific to each experiment and correct for the unknown cooler voltage offset.

Resonant peaks were found for isotopes $^{58-68,70}$Ni in the first run. Except for ^{61}Ni and ^{63}Ni the resonant structures of other isotopes were confirmed in the second run.

5.2.1 Analysis of the First Run

5.2.1.1 Asymmetric Lineshape

As figure 5.2 shows the population of the $^3D_3$ state is fed by the decays from states intensively lying within the range between 2.9 and 3.5 $\times 10^4$cm^{-1}. The different ΔE for each decay transition would result in different kinetic energy leading to a group of individual peaks for one resonant excitation ($3d^94s\ ^3D_3 \rightarrow 3d^94p\ ^3P_2$). Because the energy differences among those contributing states are small compared to the experimental resolution, a collective feature is expected. An asymmetric Voigt profile whose FWHM is a function of the frequency was tested to describe the asymmetry. The function for FWHM Γ is

$$\Gamma(\nu) = \frac{\Gamma_0}{1 + \exp[a(\nu - \nu_0)]} \tag{5.1}$$

where ν_0 is the centroid of the peak, Γ_0 the FWHM of the symmetric Voigt profile and a the asymmetry factor.

Including the asymmetric Voigt profile, three models were tested on the sampled single-peak spectrum:

(i) Symmetric pseudo-Voigt profile (SYM). It was set as a reference.

(ii) Satellite peak added on the lower energy side (SP). Because the asymmetry is small, only one satellite peak was added. The satellite peak corresponds to a collisional excitation which would reduce the kinetic energy by the excitation energy. It was label as δ and in units of eV. The other parameter defining the asymmetry is the relative height of the satellite peak to the major peak given by λ,

(iii) Asymmetric Voigt profile (EXPO). As defined in Equation 5.1, where a is the asymmetry factor.

Figure 5.5 shows the comparison of reduced χ^2 between asymmetric models SP, EXPO and symmetric model SYM. In most cases the reduced χ^2 of the model EXPO is smaller than that of the symmetric model, while the model SP does not always decrease the reduced χ^2 compared to the symmetric model.

Figure 5.6 demonstrates the shift of centroid (of the major peak) when the fitting model was changed from the asymmetric models SP, EXPO to the symmetric profile. The shift using model SP varies dramatically for different spectra while it is much more consistent for the model EXPO. Based on the two comparisons, it was considered preferable to use the model EXPO.

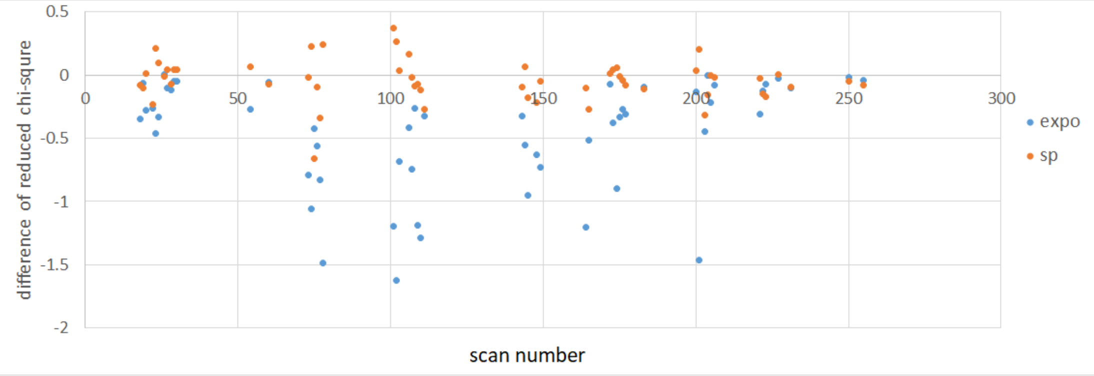

FIGURE 5.5: Orange: χ^2_{red}(SYM) - χ^2_{red}(SP); Blue: χ^2_{red}(EXPO) - χ^2_{red}(SYM).

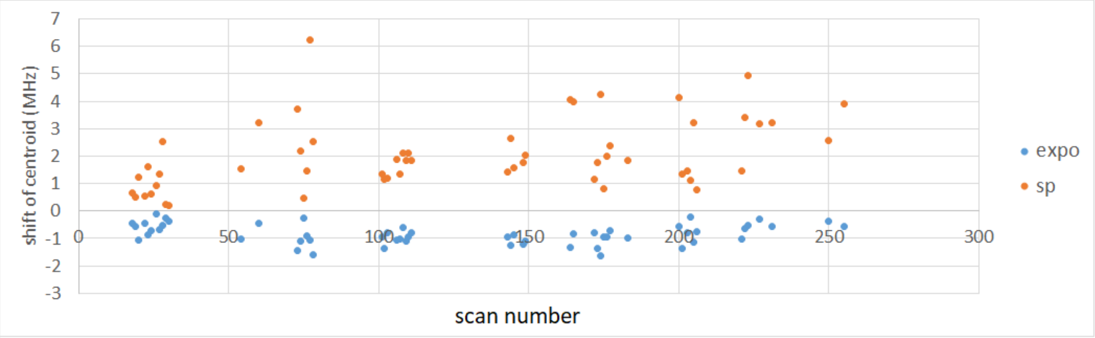

FIGURE 5.6: Orange: centroid(SYM) - centroid(SP); Blue: centroid(EXPO) - centroid(SYM).

Although the asymmetry factor a (shown in Figure 5.7) displays a degree of scatter, the influence on the centroid is small as demonstrated in Figure 5.6. Hence parameter a was fixed at the value of the average to simplify the analysis.

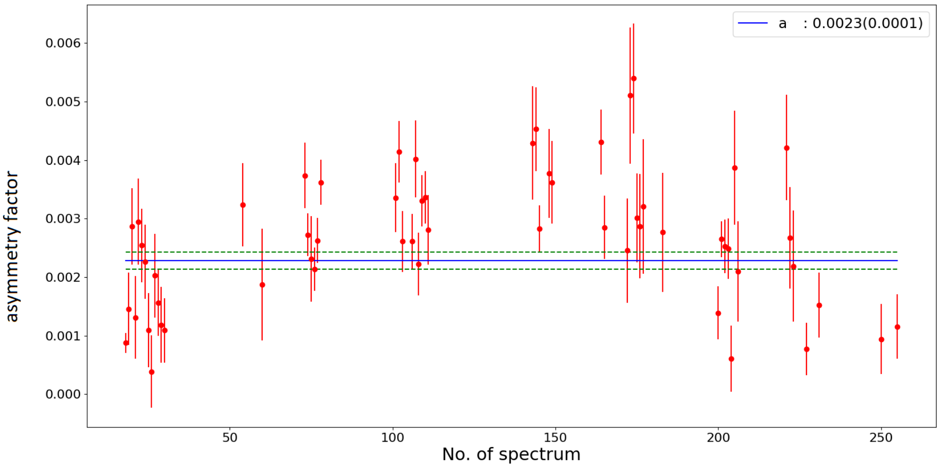

FIGURE 5.7: The asymmetry factor a of the sampled spectra in the first run of the Ni experiment. The weighted average was used as the fixed value of a.

5.2.1.2 Results and King Plot

The spectra of Ni isotopes measured in the 2016 experiment are shown in Figure 5.8. Figure 5.9 demonstrates the fitting details of one ^{65}Ni spectrum. The atomic factors A and B and isotope shifts compared to ^{60}Ni are listed in Table 5.4.

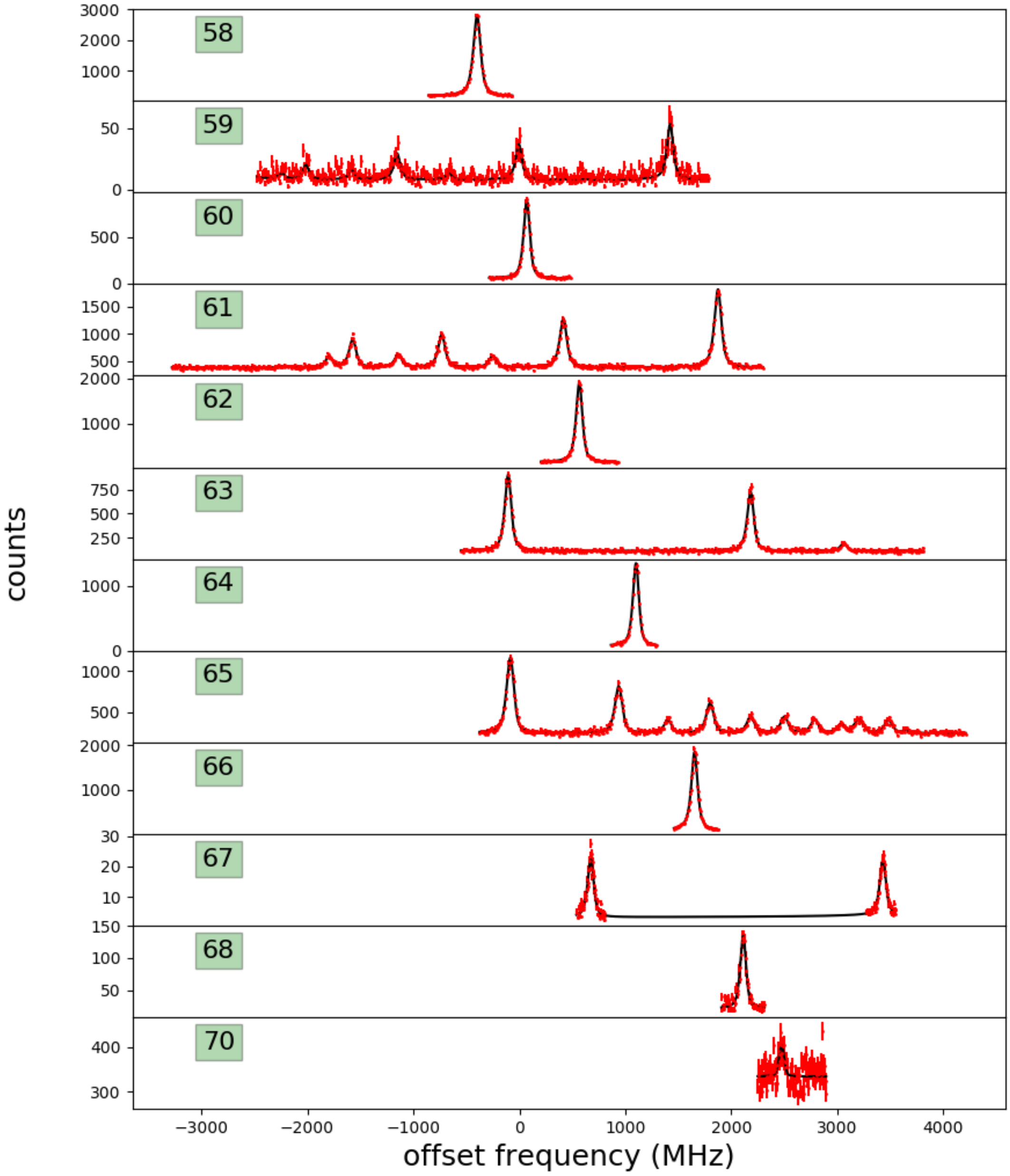

FIGURE 5.8: Spectra of $^{58-68,70}$Ni measured in the 2016 experiment. The black lines are the evaluated resonant peaks using the fitting result.

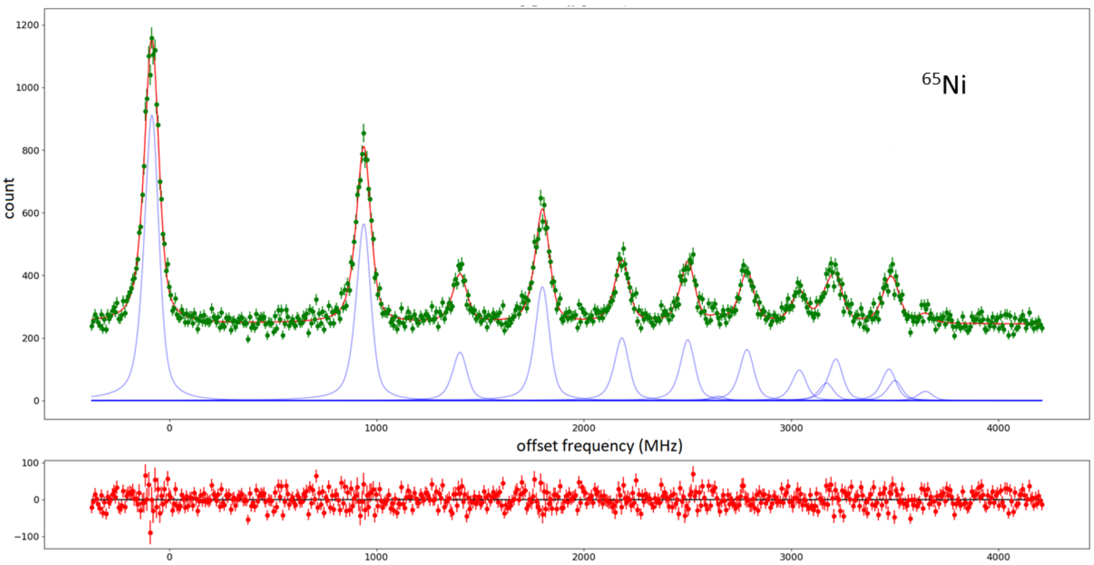

Figure 5.9: Example of fitting the ^{65}Ni spectrum.

isotope	$A(^3D_3)$	$A(^3P_2)$	$B(^3D_3)$	$B(^3P_2)$	isotope shift
58 (6 scans)					-509.9(20)[44]
59 (3 scans)	-453.5(11)	-176.9(14)	-53.3(74)	-28.2(58)	-214.7(28)[21]
60(reference)					0
61 (4 scans)	-455.0(2)	-177.2(3)	-103.0(17)	-50.5(13)	283.0(22)[21]
62 (4 scans)					504.3(20)[41]
63 (3 scans)	+904.3(7)	+351.8(12)			785.7(17)[61]
64 (6 scans)					1028.7(16)[80]
65 (4 scans)	+276.7(2)	+108.0(3)	-60.5(27)	-30.3(20)	1324.2(29)[98]
66 (6 scans)					1532.2(15)[117]
67 (2 scans)	+1095.4(9)	[+431.6(3)]*			1796.7(20)[135]
68 (3 scans)					1994.1(20)[152]
70 (3 scans)					2383.8(54)[184]

Table 5.4: Atomic factors and isotopes shifts in MHz obtained from the analysis of the first run of the Ni experiment.
*$A(^3P_2)/A(^3D_3)$ was fixed at the weighted mean +0.3897 obtained from the ^{59,61,63,65}Ni isotopes (Figure 5.10).

In the 2017 run, the spin of ^{67}Ni was confirmed to be 1/2 and the hyperfine structure has three peaks. Because there was no convincing observation of the smallest peak in the first run, the ratio of A factors between upper and lower states was fixed at the average of the other odd isotopes ($A(^3P_2)/A(^3D_3)$=+0.3897(5)). Figure 5.10 shows the ratios are consistent with a constant value.

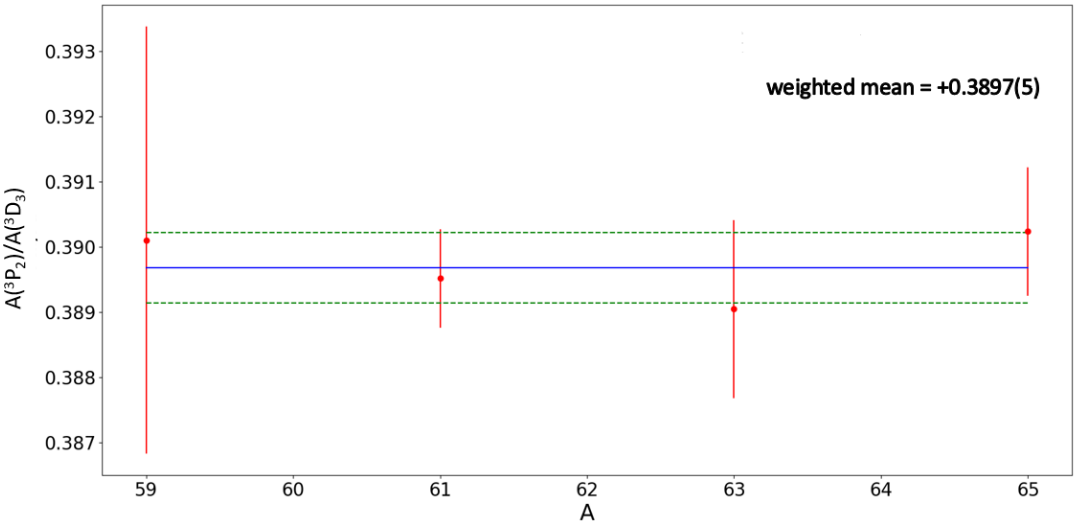

FIGURE 5.10: The ratio $A(^3P_2)/A(^3D_3)$ of ^{59,61,63,65}Ni in the 2016 Ni experiment.

The $\delta\langle r^2\rangle_{\mu e}$ used in the King plot were taken from [13] and shown in Table 5.3. The result is demonstrated in Figure 5.11

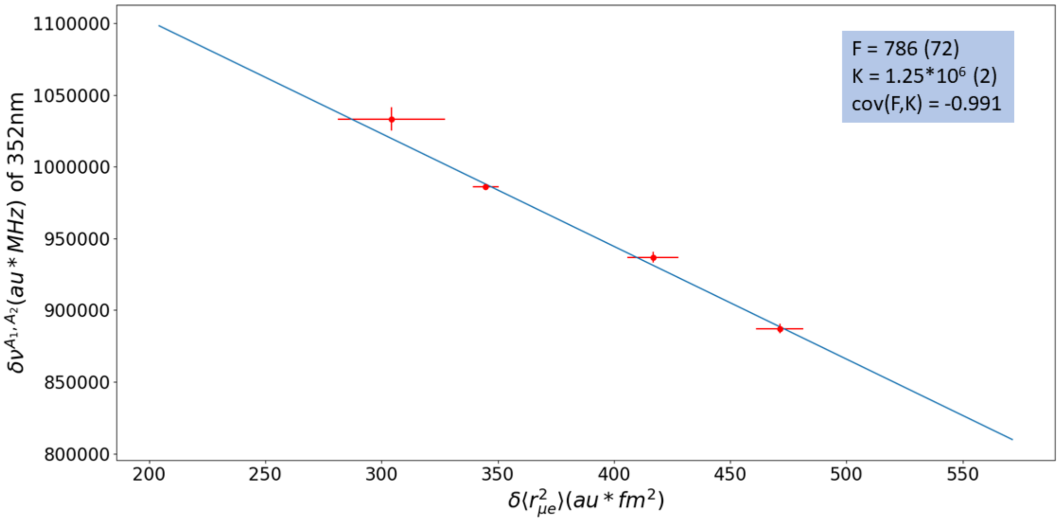

FIGURE 5.11: The King plot of the first run of the Ni experiment.

5.2.2 Analysis of Second Run

5.2.2.1 Asymmetry

The spectrum of the early scans (scan number < 81) in the 2017 experiment showed significant asymmetry. It was probably due to the high temperature of the charge exchange cell. The dense sodium vapour led to a high probability of collisional excitation. Two satellite peaks were added to the EXPO model mentioned previously. The temperature of the charge exchange cell was turned down after No. 81 scan and the lineshape of later spectra became less asymmetric. The fitting profile was reduced to a simple EXPO model.

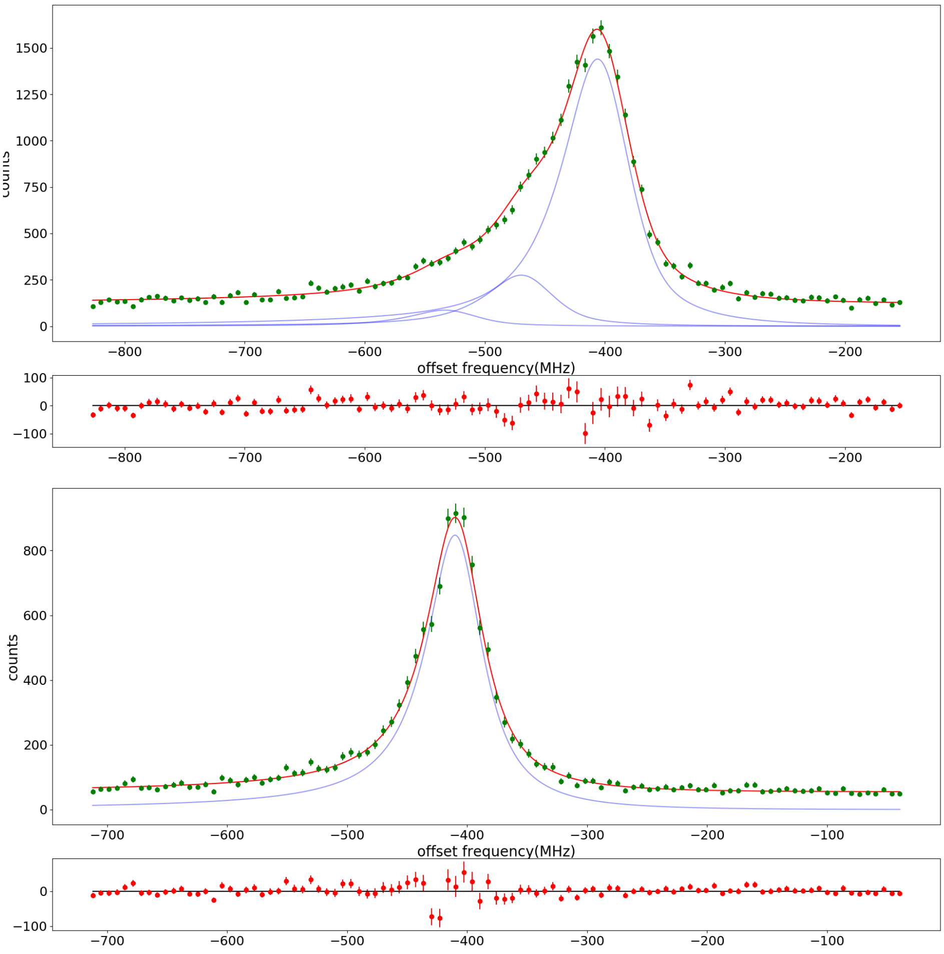

FIGURE 5.12: Examples of ^{58}Ni spectra. Top: Spectrum of ^{58}Ni with a dense charge exchange vapour. Two satellite peaks were added and all peaks were in the shape described by Equation 5.1. Bottom: Spectrum of ^{58}Ni with moderate density charge exchange vapour. The peak was described by Equation 5.1 without any satellite peak.

The parameters defined the asymmetry are listed as:

1. δ the collisional excitation energy in unit of eV;
2. λ_1 and λ_2 determining the relative heights of the first and second satellite peaks to the major peak. The value does not follow the Poisson distribution.
3. a the asymmetry factor defined in Equation 5.1

The values of those parameters were fixed at the average of the sampled single-peak spectra (Figure 5.13).

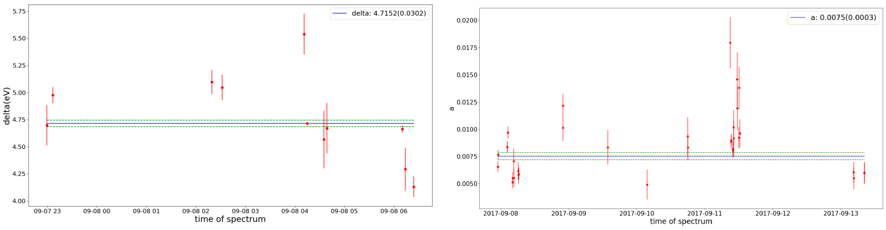

(A) δ (B) a

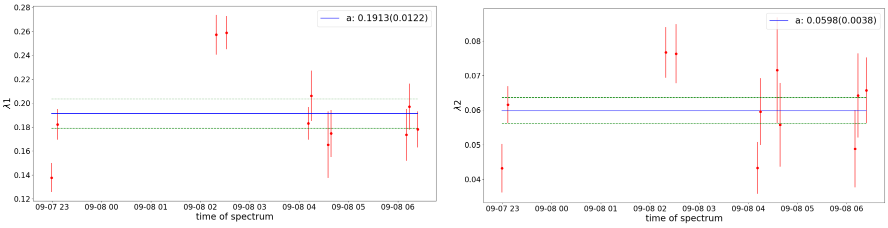

(C) λ_1 (D) λ_2

FIGURE 5.13: Asymmetric parameters of sampled single-peak spectrum of the 2017 Ni experiment. The average values of δ, λ_1 and λ_2 were used to fix the early runs up to scan number 81.

Taking a rude estimate that the distance between CEC and detection region is 1 m. The kinetic energy of the ion/atom beam is about 40 keV. Taking the mass of Ni atom as 60 au (1au = 931.494 MeV/C^2) and using the basic kinetic energy equation $K = 1/2mv^2$ and $d = vt$, the time of flight is approximately 2.8 μs. The transition responsible for the satellite peaks should have a life-time comparable to this value. Yet no such transition was found nearby the fixed value (4.8 eV). Therefore, the value of parameter δ was determined entirely empirically.

5.2.2.2 Result and King Plot

The atomic factors and isotopes shifts extracted from the second run are presented in Table 5.5. ^{59,63}Ni were not measured in the second run as the spectra from the first run were considered sufficient. The third peak of ^{67}Ni which was missed in the first run was observed by scanning the predicted region repeatedly. The complete spectrum of ^{67}Ni is shown in Figure 5.14 and the ratio $A(^3P_2)/A(^3D_3)$ in 2017 experiment is $+0.3892(7)$, consistent with the value from the previous run. A separate King plot (shown in Figure 5.16) was performed using the measurements of the 2017 experiment.

isotope	A($^3D_3$)	$A(^3P_2)$	$B(^3D_3)$	$B(^3P_2)$	isotope shift
58 (7 scans)					-508.1(14)[44]
60 (reference)					0
61 (4 scans)	-454.4(3)	-176.9(3)	-103.4(16)	-51.5(1)	279.1(15)[21]
62 (4 scans)					502.2(14)[41]
64 (4 scans)					1025.3(15)[80]
65 (2 scans)	+276.5(3)	+107.6(4)	-63.5(36)	-28.9(27)	1311.1(21)[99]
66 (4 scans)					1521.3(16)[117]
67 (2 scans)	+1088.0(20)	+422.0(29)			1795.2(32)[135]
68 (3 scans)					1987.6(21)[151]

TABLE 5.5: Atomic factors and isotopes shifts in MHz obtained from the analysis of the second run of the Ni experiment.

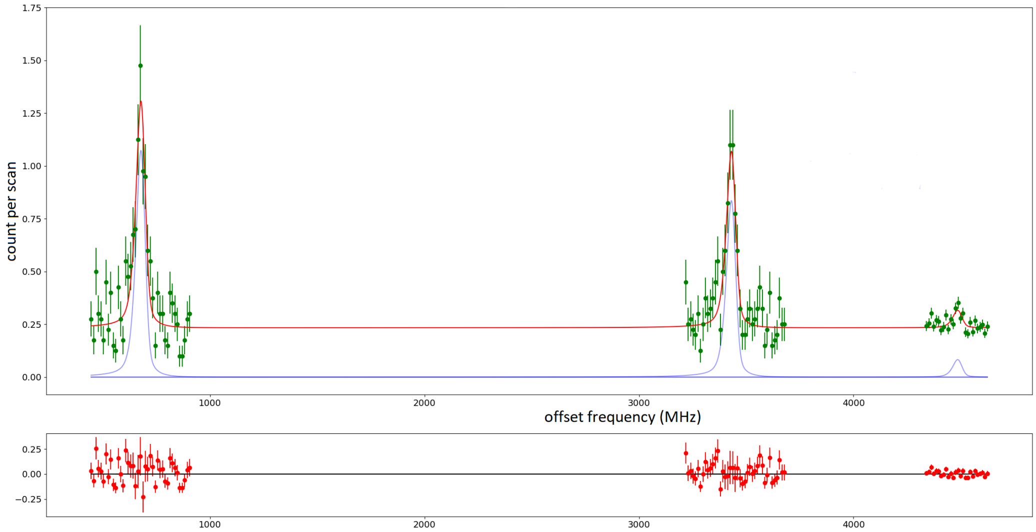

FIGURE 5.14: Spectra of ^{67}Ni obtained in the 2017 Ni experiment. The two major peaks and the smallest peak were recorded in separate scans.

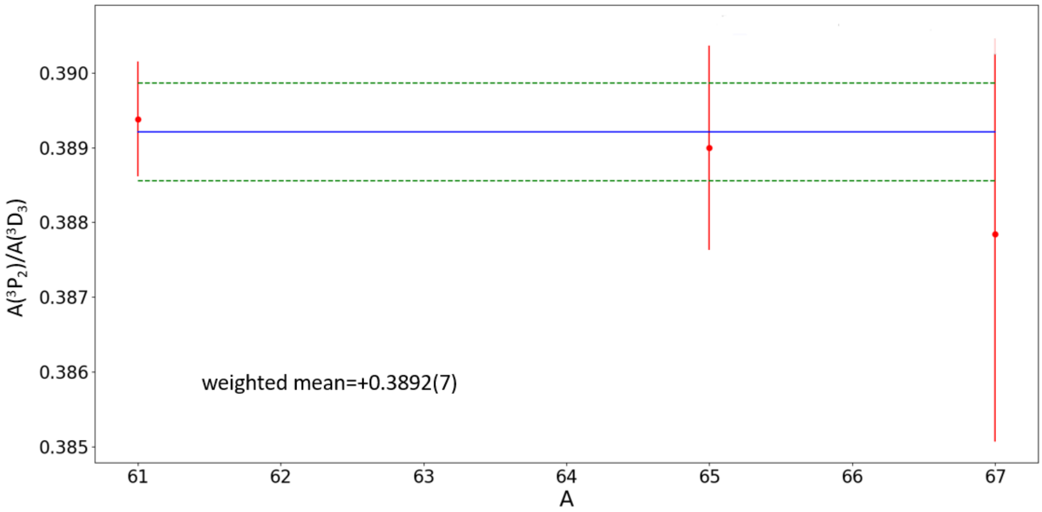

FIGURE 5.15: The ratio $A(^3P_2)/A(^3D_3)$ of ^{61,65,67}Ni in the 2017 Ni experiment.

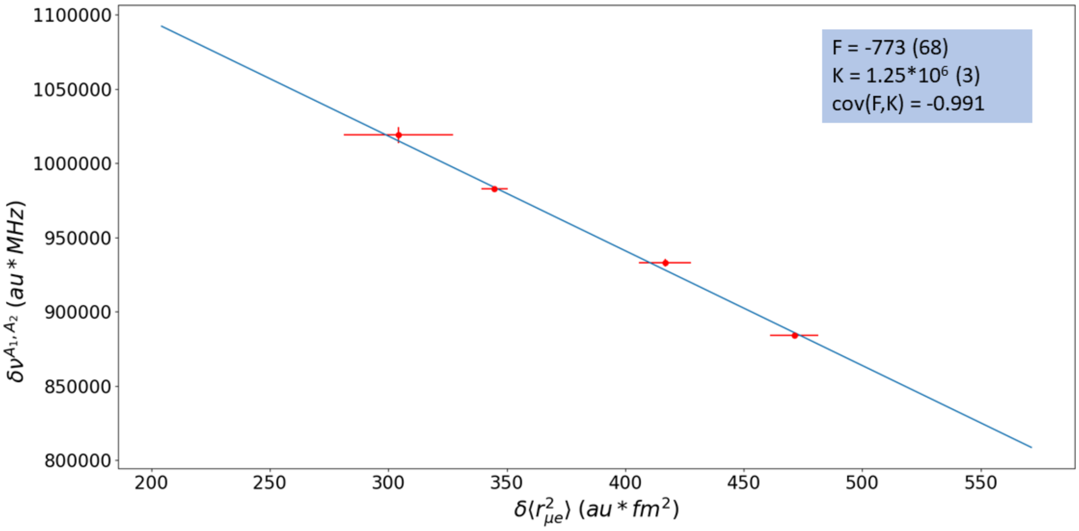

FIGURE 5.16: King plot of the second run of the Ni experiment.

5.2.3 Comparisons of IS and $\delta\langle r^2\rangle$ Obtained from the 2016 and 2017 Experiments

Due to the uncertainty of the ISCOOL voltage, the isotope shifts of the second run are slightly different from those of the first. The two King plots linking observed isotopes shifts to the $\delta\langle r^2\rangle_{e\mu}^{60,A}$ values in Table 5.3 give two sets of $\delta\langle r^2\rangle^{60,A}$ which are directly comparable, independent of the actual ISCOOL voltages used in the two runs. The $\delta\langle r^2\rangle^{60,A}$ of both runs are listed in Table 5.6 and the averaged values were used to obtain Figure 5.17

A	$\delta\langle r^2\rangle^{60,A}$ (2016)	$\delta\langle r^2\rangle^{60,A}$ (2017)	average
58	-0.272(2)[6]	-0.272(2)[5]	-0.272(2)[6]
59	-0.179(4)[7]		-0.179(4)[7]
61	0.079(3)[3]	0.082(2)[2]	0.081(2)[3]
62	0.220(3)[3]	0.221(2)[3]	0.221(2)[3]
63	0.274(2)[4]		0.274(2)[4]
64	0.362(2)[6]	0.361(2)[6]	0.361(2)[6]
65	0.373(4)[12]	0.382(3)[11]	0.378(3)[12]
66	0.482(2)[11]	0.487(2)[10]	0.485(2)[11]
67	0.509(3)[16]	0.500(4)[16]	0.504(3)[16]
68	0.610(3)[15]	0.607(3)[15]	0.608(2)[15]
70	0.790(7)[15]		0.790(7)[15]

TABLE 5.6: $\delta\langle r^2\rangle^{60,A}$ from two runs of the Ni experiments. The final systematic error took the larger one of two runs because the $\delta\langle r^2\rangle^{60,A}$ of two runs are correlated by using the same $\delta\langle r^2_{\mu e}\rangle$ in King plot.

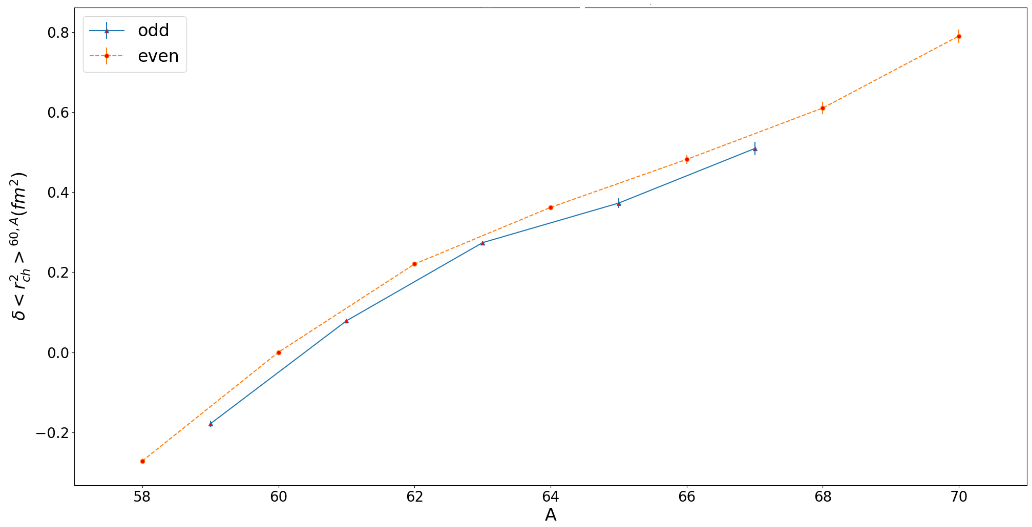

FIGURE 5.17: The $\delta\langle r^2\rangle^{60,A}$ of Ni isotopes in unit of fm^2 compared to ^{60}Ni.

Chapter 6

Conclusion

The mean square charge radii of Ni ($Z = 28$) and Zn ($Z = 30$) isotopes extracted from the experiments of this thesis are plotted in Figure 6.1 with Cu ($Z = 29$) [41] and Ga ($Z = 31$) [42, 43] isotopes. The similarity in the general trends of mean square charge radii indicate the similarity in the nuclear structure. It should be noted that the systematic errors of Zn and Ni isotopes are much smaller than that of Ga and Cu. Covariance coefficients of atomic factors F and K obtained from the King plots are about -0.9 meaning large a contribution from the atomic factors were cancelled due to this correlation. For Ga and Cu, the atomic factors were obtained from theoretical estimation. Although the F used in all elements have similar percentage errors, without subtraction of the correlation term, the calculated systematic errors of Ga and Cu should be much larger than that of Ni and Zn.

The charge radius is a fundamental property of the nucleus and determined by the protons' distribution within the nucleus. There have been many studies [8, 9] searching for a systematic understanding of the relationship between the charge radius and the nuclear structure.

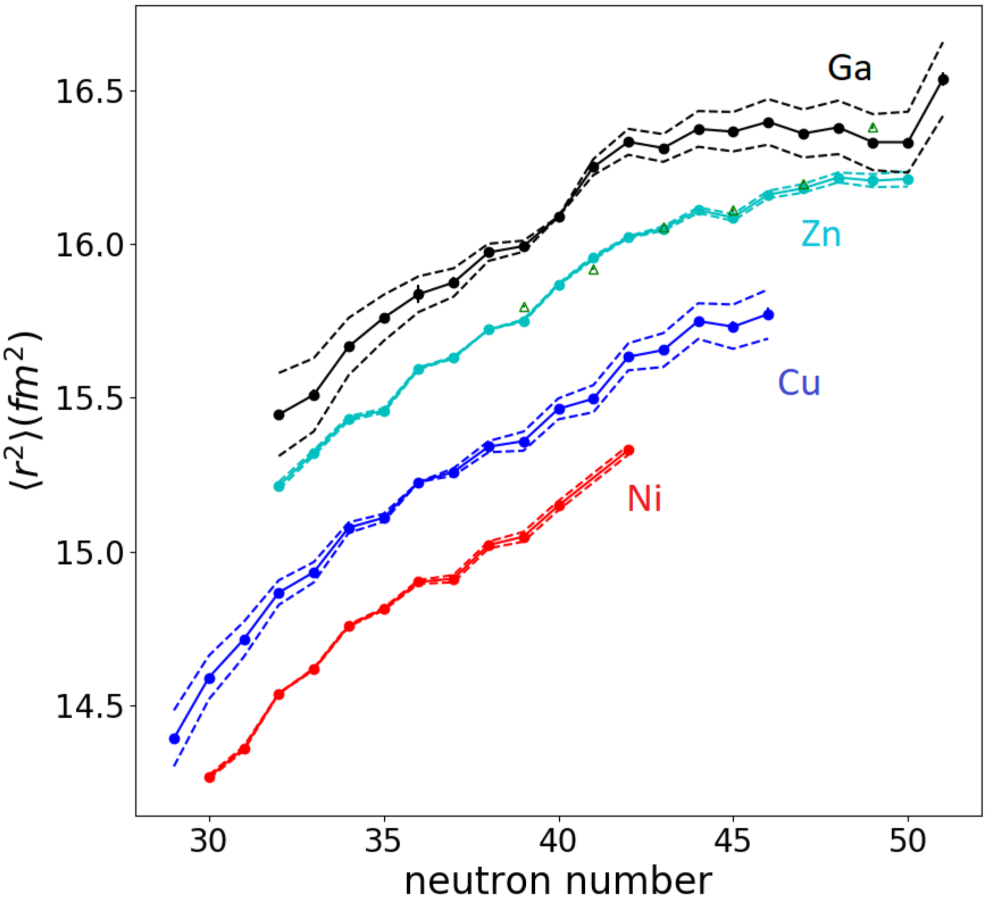

FIGURE 6.1: Experimental mean square charge radii of the Ni, Cu, Zn and Ga isotopes. The green triangles are the isomers observed in Zn experiment. The dashed lines represent the systematic errors originating from the uncertainty of atomic factors obtained from King plots.

Although there are many contributing factors, the general trend of the charge radii along isotope or isotonic chains can be well described in a collective point of view. The droplet model which calculates the spherical volume produces a good description of the general trend of the charge radii along isotope or isotonic chains in many cases [15]. The charge radii calculated by the droplet model can be regarded as the volume contribution as it was derived from the collective properties such as the average proton density, skin thickness *etc.* The prediction of the droplet model is a smooth trend with neutron number.

The droplet model can be modified by adding the deformation correction (both dynamic and static). Deformation parameters β_2 and β_4 can be introduced into the calculations of the droplet model [44]. As a good example, the clear effect of deformation on charge radii can be seen on the Cs isotopes (Figure 6.2). Although there are still discrepancies between the droplet model calculation and the experimental results beyond $N = 82$, the deformation corrections made great improvements compared to the spherical droplet model. The effect of deformation on the charge radii of the Zn isotopes will be discussed in detail in Section 6.2.1.

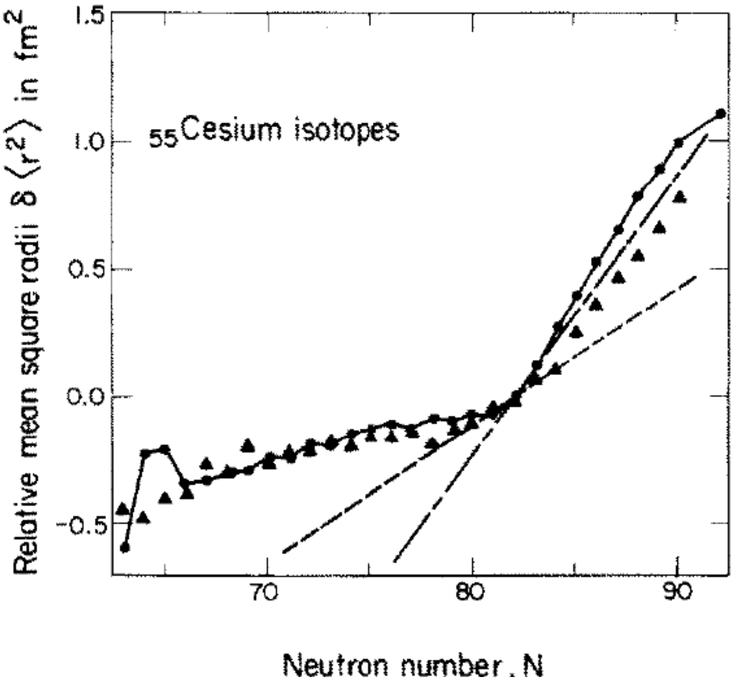

FIGURE 6.2: The dots connected by solid lines are experimental measurement of mean square charge radii (relative to $N = 82$) [45] of the caesium isotopes. The triangles are the droplet-model predictions with deformation correction. The dashed line and dot-dashed line are the predictions of the spherical droplet model and the liquid drop model [45]. The charge radius of ^{118}Cs (the lightest) shown in the plot was incorrect. A correction was presented in [20].

The model can be further modified by adding the shell effects. As the nucleons are bonded more tightly near the shell gap, both the correlations and deformation decrease. The charge radii of isotopes between two shell gaps would form a parabolic curve. A kink such as that seen in ^{82}Ga immediately above $N = 50$ [42] (shown in Figure 6.1) is an indication of a shell gap.

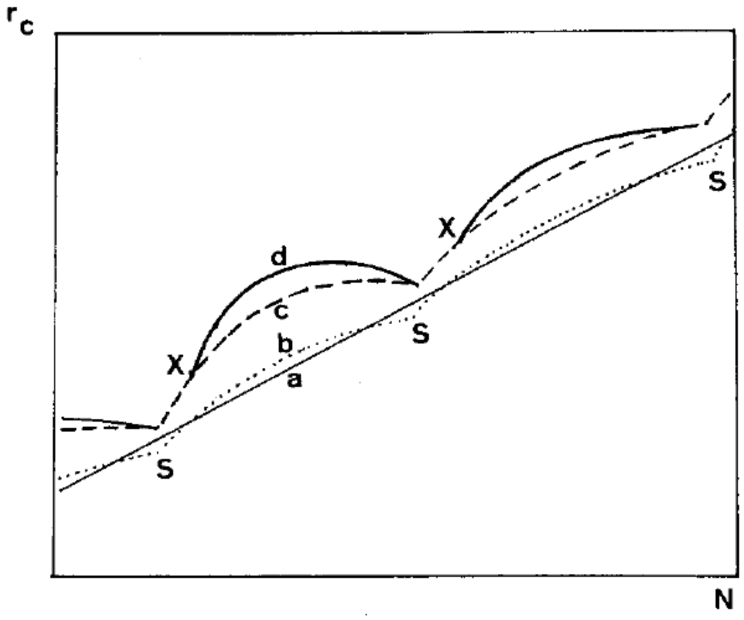

FIGURE 6.3: Demonstration of different contributions to the nuclear charge radii along the isotopic chain [44].
(a) smooth part for spherical shapes
(b) spherical shapes with shell effects,
(c) "spherical" nuclei with dynamical deformation,
(d) statically deformed nuclei.
X: onset of static deformation, S: shell closure

All the factors in the above discussion are demonstrated in Figure 6.3, leading to a smooth curve along the isotopic chain except at a closed shell. The result is a good description of the general trend. Local variations such as the odd-even staggering (the radius of the odd-N isotope is usually smaller than the average of the adjacent even-N isotopes) can be related to the proton scattering into higher states, or proton-neutron correlations.

6.1 The Effect of $N = 40$ Sub-shell

The closed shells minimize both deformation and pairing or higher order correlations so local minima in charge radii indicate the closed shell nuclei. Since the spherical droplet model only describes the volume contribution, for a better view of the local minimum, the volume contribution $\langle r^2 \rangle_{volume}$ may be subtracted from the experimental $\langle r^2 \rangle$ [41]. The result is plotted in Figure 6.4. The odd-and even-N isotopes are connected by separate lines to emphasize the effects of odd-even staggering.

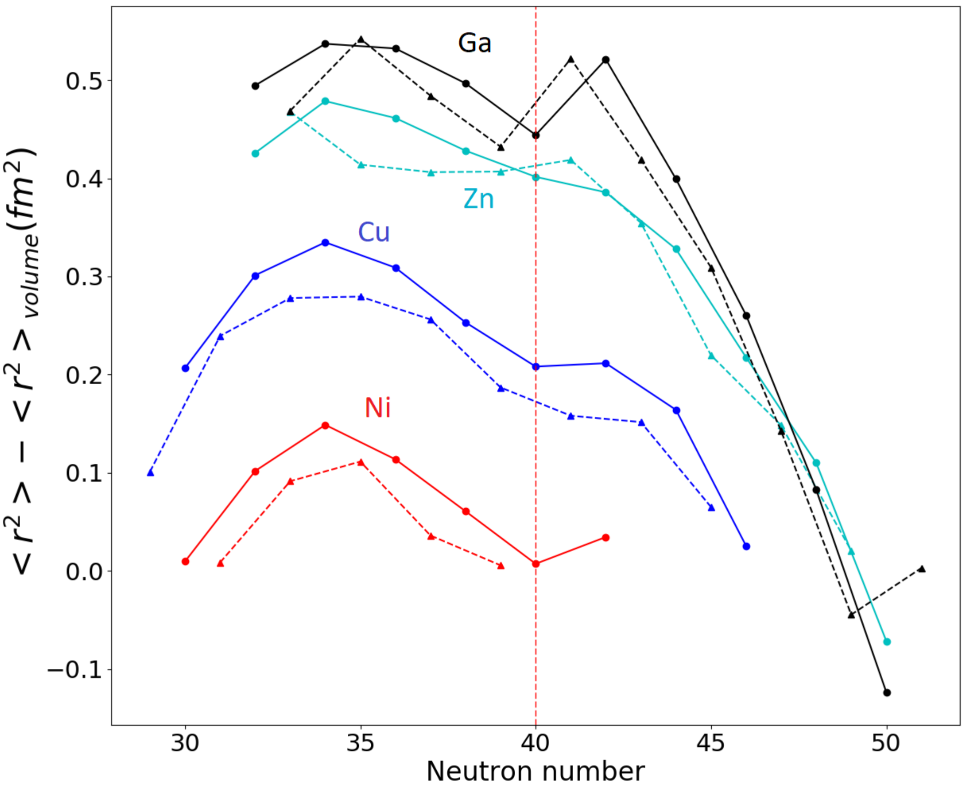

FIGURE 6.4: The experimental $\langle r^2 \rangle$ with the volume term $\langle r^2 \rangle_{volume}$ of the spherical droplet model subtracted. Even-N isotopes are connected by solid lines while odd-N isotopes by dashed lines.

As shown in Figure 6.4 there is a clear local minimum at $N = 40$ for the Ni isotopic chain. The minimum is weaker in Cu and almost disappears in Zn and Ga. It demonstrates that the sub-shell effect of $N = 40$ diminishes quickly as the proton number moves away from $Z = 28$. The inversion of odd-even staggering is observed at $N = 40$ for Ga and Zn isotopic chains. This may be due to the residual sub-shell effect or to the onset of static deformation in the $N \approx 40$ region as revealed in the study of Kr ($Z = 36$) and Sr ($Z = 38$) [46].

6.2 The Zn Isotopes

6.2.1 Effect of Deformation

The intrinsic quadrupole moments Q_0 of even Zn isotopes were calculated using

$$Q_0 = \sqrt{\frac{16\pi B(E2; 0_1^+ \rightarrow 2_1^+)}{5}} \tag{6.1}$$

where $B(E2; 0_1^+ \rightarrow 2_1^+)$ is the $E2$ transition probability from the ground state (0^+) to the first 2^+ state. The values were taken from [47] and listed in Table 6.1. For odd isotopes, Q_0 was calculated using

$$Q_0 = \frac{(I+1)(2I+3)}{3K^2 - I(I+1)} Q_s \tag{6.2}$$

where Q_s is the spectroscopic quadrupole moment extracted from the measured B hyperfine factors in the Zn experiments [10] and K is the projection of I on the deformation axis. If the nucleus has a well deformed ground state, K is approximately equivalent to I but the assumption may not be valid for the perhaps weakly-deformed Zn nuclei. Such an assumption was made in the calculation of Q_0 and the results listed in Table 6.2 are therefore the lowest possible deformations.

In the droplet model [48], Q_0 can be calculated using β_2. Thus with an initial input of β_2, a Q_0 was predicted. The value of β_2 was changed until the corresponding Q_0 equal to the Q_0 listed in Table 6.1 and 6.2 was reached. Since Equation 6.2 does not apply for $I = 1/2$ states, for ^{69,71,73}Zn the β_2 of the Q_0 values of the isomer were used to calculate β instead. The extracted β_2 can be used to evaluate the effect of deformed shapes on the charge radius by

$$\langle r^2 \rangle \approx \langle r^2 \rangle_0 \Big(1 + \frac{5}{4\pi} \langle \beta_2^2 \rangle\Big) \tag{6.3}$$

where $\langle r^2\rangle_0$ is the mean square charge radius of a spherical nucleus with identical volume. The equation is an approximation of

$$\langle r^2\rangle = \langle r^2\rangle_0\Big(1+\frac{5}{4\pi}\sum_{i=2}^{\infty}\langle\beta_i^2\rangle\Big) \tag{6.4}$$

as deformations of higher order (> 2) are neglected [9]. The calculation assumed $\langle\beta_2^2\rangle = \langle\beta_2\rangle^2$ i.e. only static deformation contributes. The spherical droplet model was used to calculate $\langle r^2\rangle_0$. The contribution of deformation estimated from β_2 is $\Delta\langle r^2\rangle_{\beta_2} = \langle r^2\rangle_0\frac{5}{4\pi}\beta_2^2$ as shown in the lower panel of Figure 6.5.

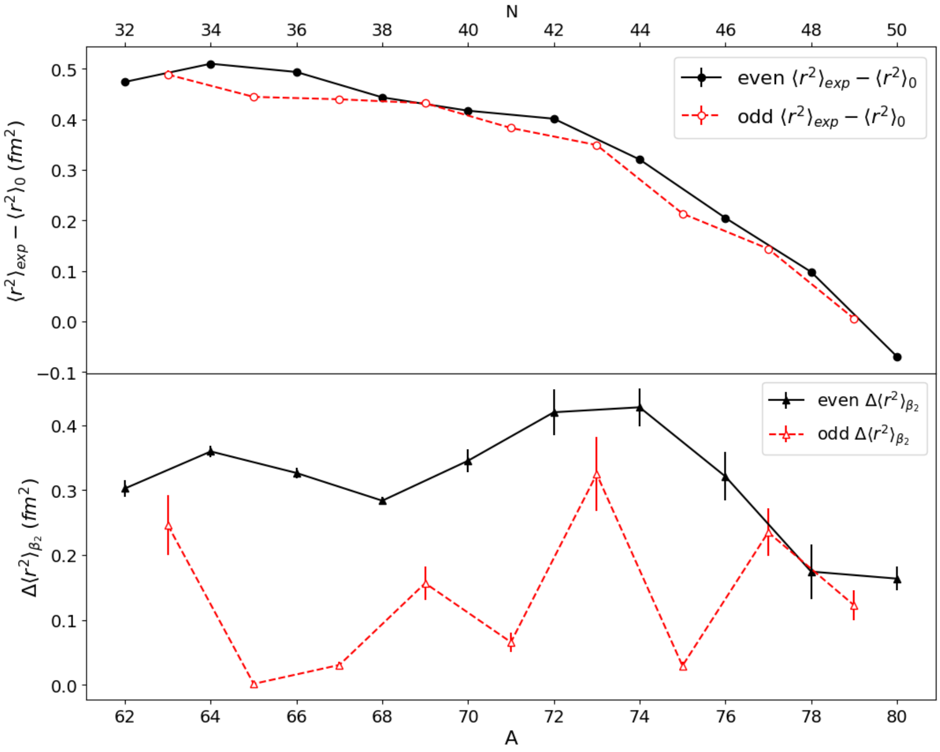

FIGURE 6.5: Top: Mean square charge radii with volume contribution subtracted. The plot is not exactly the same as the plot of the Zn isotopes in Figure 6.1 as for ^{69,71,73}Zn, the values of isomers were used instead.
bottom: Contribution of deformation estimated from the β_2 using Equation 6.3.

Top panel of Figure 6.5 presents the mean square charge radii with the volume contribution of the spherical droplet model subtracted. The effect of the calculated β_2 was compared with these experimental results. The $\langle r^2\rangle_{exp} - \langle r^2\rangle_0$ in the top panel of Figure 6.5 follow an approximately parabolic curve which is not observed in $\Delta\langle r^2\rangle_{\beta_2}$. As mentioned earlier, the parabolic curve is the result of the shell effect expected at N=50 which includes both the reduction in deformation and proton-neutron correlations. The fact that the $\Delta\langle r^2\rangle_{\beta_2}$ fails to reproduce the parabolic pattern demonstrates the correlations also play an important role in the understanding of charge radii. Although it is not perfectly convincing, there are still some visible connections between the $\langle r^2\rangle_{exp} - \langle r^2\rangle_0$ and the $\Delta\langle r^2\rangle_{\beta_2}$. For instance, the evolution pattern of the light even isotopes ^{62,64,66,68}Zn. Also the large drops of $^{65,71\mathrm{m},75}$Zn compared to the adjacent even isotopes also reflect as a dipping in $\Delta\langle r^2\rangle_{\beta_2}$. The fact that the odd-even staggering in $\Delta\langle r^2\rangle_{\beta_2}$ is much larger than the experimental results reveals the $\langle\beta_2^2\rangle$ were underestimated because the assumptions $K = I$ and $\langle\beta_2^2\rangle = \langle\beta_2\rangle^2$ are inappropriate. The larger $\langle\beta_2^2\rangle$ observed for the even isotopes may be attributed to the dynamic deformation.

A	B(E2) (e^2b^2)	$\lvert\beta_2\rvert$
62	0.1224 (59)	0.227 (5)
64	0.1494 (4)	0.246 (3)
66	0.137 (33)	0.233 (3)
68	0.1199 (21)	0.216 (2)
70	0.151 (8)	0.237 (6)
72	0.188 (17)	0.260 (11)
74	0.195 (15)	0.261 (9)
76	0.145 (18)	0.225 (13)
78	0.077 (19)	0.165 (20)
80	0.073 (9)	0.159 (9)

Table 6.1: The $B(E2)$ and the corresponding β_2 calculated using Equation.

A	Q_s	Q_0	β_2
63	+0.20 (2)	+1.0 (1)	+0.204 (19)
65	-0.024 (15)	-0.07 (4)	-0.015 (9)
67	+0.122 (10)	+0.34 (3)	+0.071 (6)
69$^\mathrm{m}$	-0.39 (3)	-0.72 (6)	-0.160 (13)
71$^\mathrm{m}$	-0.26 (3)	+1.27 (1)	-0.103 (12)
73$^\mathrm{m}$	+0.43 (4)	-0.48 (6)	+0.228 (20)
75	+0.16 (2)	+0.34 (4)	+0.068 (8)
77	+0.48 (4)	+1.03 (9)	+0.192 (15)
79	+0.40 (4)	+0.73 (7)	+0.138 (13)

Table 6.2: Spectroscopic quadrupole moment, intrinsic quadrupole moment and corresponding β_2 factor deduced using the droplet model.

6.2.2 Proton Occupation Number

In a naive shell model, the number of protons occupying the orbital above the $Z = 28$ major shell closure for Zn isotopes is 2. In reality, protons do not occupy a single orbital but are distributed over multiple single particle states. As the occupation of the neutron states varies along the isotopic chain, the proton-neutron interaction changes the proton distribution. Assuming the higher energy states have larger mean square charge radii, increased occupation of the high energy state above Z=28 leads to larger charge radii.

The proton occupation numbers of Zn isotopes above Z=28 were calculated using the advanced Monte Carlo shell model (MCSM) with the A3DA-m interaction in a full $fpg_{9/2}d_{5/2}$ model space illustrated in Figure 6.6. The A3DA-m interaction has been used to calculate the moments of nuclei in Zn isotopes [10, 11] and Cu isotopes [49] with good success. The sensitivity of the proton occupation numbers on the charge radii can be shown in the relative charge radii between the ground states and the isomers observed in this experiment. In Figure 6.7, the $\langle r^2 \rangle_{exp}$ of ^{69,71,73,75,77}Zn with different spins are plotted alongside their calculated proton occupation number in Figure 6.7 (lower panel). The isomer of ^{79}Zn is not presented because its neutron configuration has a large contribution from the $s_{1/2}$ orbit which is outside of the model space used here [12]. In each case, the nuclear state with larger proton occupation number above the Z=28 is found to have larger mean square charge radius than the other state measured for that isotope.

The qualitative connection between the proton occupation number and the charge radius can also been seen in the odd-even staggering. As shown in Figure 6.8 (a), the local fluctuations of the proton occupation numbers above Z=28 in the Zn isotopes resemble the pattern of the odd-even staggering. This is clearly visible at N=45 where a significant reduction is seen both in the proton occupation number and the mean square charge radius. The odd-even staggering of the charge radii can be visualized by the difference between the $\delta\langle r^2 \rangle$ with N and the mean $\delta\langle r^2 \rangle$

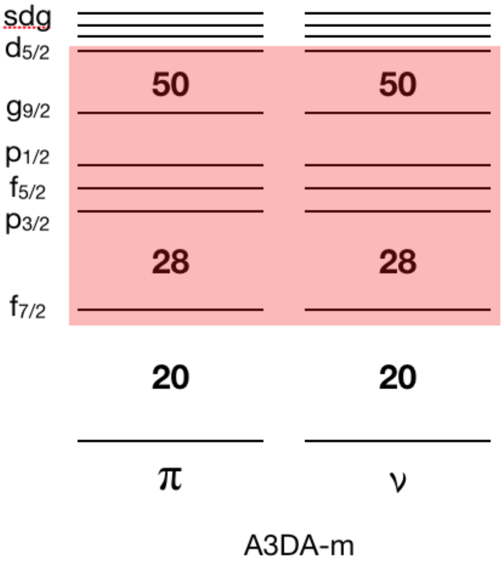

FIGURE 6.6: The model space used in A3DA-m calculation. The shaded states are included within the active model space. The A3DA-m uses the ^{40}Ca (Z=20, N=20) core.

of neighbouring isotope with the N-1 and N+1 as the following equation [50].

$$D(\delta\langle r^2\rangle, N) = \delta\langle r^2\rangle(N) - \frac{1}{2}(\delta\langle r^2\rangle(N-1) + \delta\langle r^2\rangle(N+1)) \tag{6.5}$$

For a normal odd-even staggering $D(\delta\langle r^2\rangle, N) > 0$ for even-N and $D(\delta\langle r^2\rangle, N) < 0$ for odd-N while for the inversion of odd-even staggering the inequalities reverse. The same calculation is applied to the proton occupation number. Because differences of the radii of the proton orbits $pf_{5/2}g_{9/2}d_{5/2}$ above Z=28 are small compared to the difference cross the Z=28 shell gap, the radii of these orbits are assumed to be identical. Upon such assumption, the proton occupation number is regarded proportional to its contribution to charge radii. The ratio can be calculated from the differences of charge radii and proton occupation between isomeric and ground states as shown in Figure 6.7. The result is used to scale the visualized odd-even staggering of proton occupation number calculated by Equation 6.5. As shown in Figure 6.8, the two quantities demonstrate a proportional relationship for most of isotopes. One of the exceptions is ^{63}Zn. The ground state of ^{63}Zn is a mixed configuration from $f_{5/2}$ and $p_{3/2}$ based on the magnetic dipole moment [10]. Here the A3DA-m interaction failed to reproduce

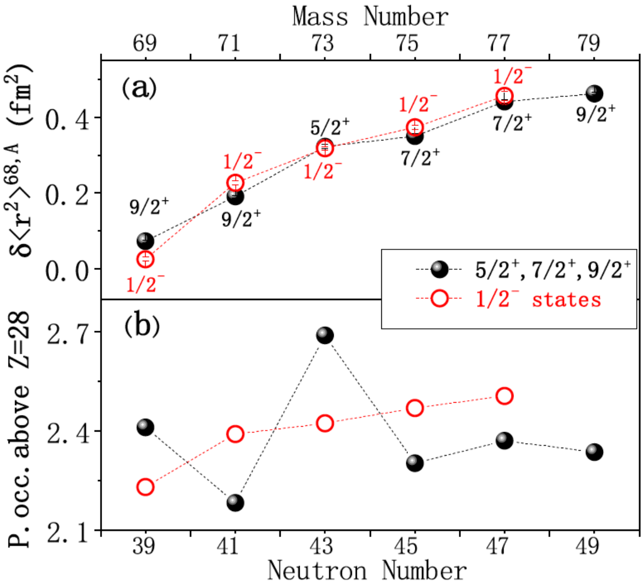

FIGURE 6.7: The relative mean square charge radii (a) and the proton occupation number (b) for heavy odd Zn isotopes. The red circles are the values of 1/2 spin while the black ones are the values of higher spins. The figure is taken from the Zn charge radii paper which is prepared by the author and his colleague X. F. Yang (Peking University).

the magnetic moment ($\mu_{expt} = -0.282\ \mu_N$ compared to $\mu_{\mathrm{A3DA-m}} = +0.11\ \mu_N$). Hence the calculated proton occupation number may not be valid. The inversion of odd-even staggering at N=41 is the result of decreased $\langle r^2 \rangle$ at N=40 caused by the decrease of proton occupation number. The largest odd-even staggering is observed at N=35 and N=45, the mid-shell of $f_{5/2}$ and $g_{9/2}$. This is visible in both proton occupation number and experimental $\delta\langle r^2 \rangle$. As N approaches the closed shell N=50, the scale of odd-even staggering decreases in the charge radii and in proton occupation number.

6.2.3 Isomer Shift of the $1/2^+$ State in ^{79}Zn

An unusual isomer was observed in ^{79}Zn with a large isomer shift of $\langle r^2 \rangle(^{79\mathrm{m}}\mathrm{Zn}) - \langle r^2 \rangle(^{79}\mathrm{Zn}) = +0.176(9)\ \mathrm{fm}^2$. The spin and negative magnetic moment from this work confirms the tentative spin-parity assignment of $1/2^+$ by Orlandi *et al* [51]. The lighter odd Zn isotopes have a $1/2^-$ state (ground state in A = 69, 71, 73; isomer in A = 75, 77) which all have magnetic moments of around $+0.56\ \mu_N$ expected for the $\nu p_{1/2}$ configuration. This isomer disappears in ^{79}Zn presumably

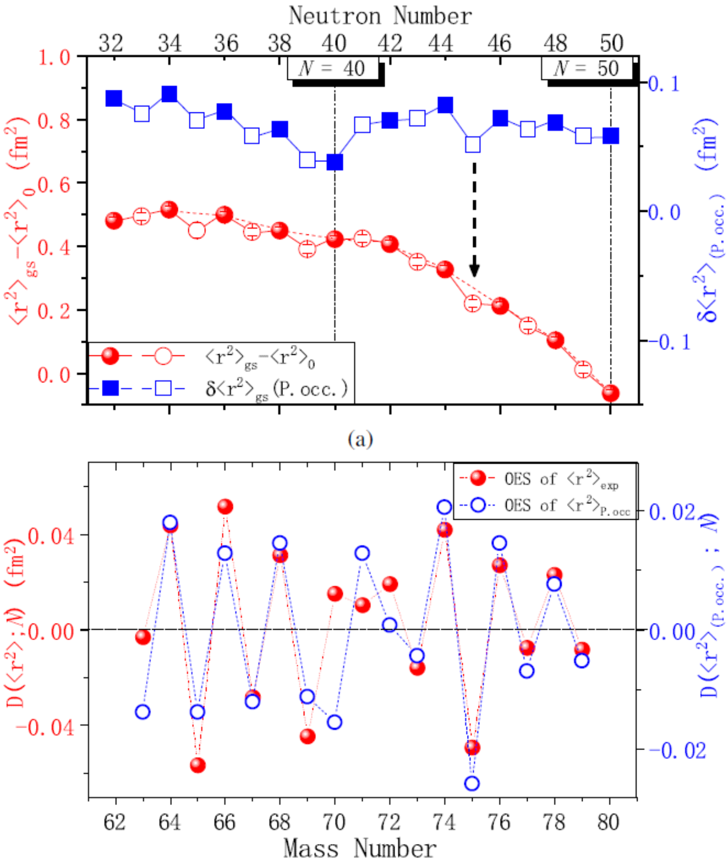

(a)

(b)

FIGURE 6.8: (a) The open and solid circles are the experimental mean square charge radii after the subtraction of the predictions of a spherical droplet model for odd and even Zn isotopes respectively. The open and solid squares are the proton occupation number above Z=28 for odd and even Zn isotopes respectively. (b) The visualization of odd-even staggering using Equation 6.5 for proton occupation numbers (blue) and mean square charge radii (red). The figure is taken from the Zn charge radii paper which is prepared by the author and his colleague X. F. Yang (Peking University).

because there is now a lower state of $1/2^+$ which the $1/2^-$ state can easily decay to and is therefore no longer isomeric. A similar situation is seen in the N=49 isotones where ^{81}Ge has a long-lived $1/2^+$ isomer but in the heavier isotones (^{83}Se, ^{85}Kr, ^{87}Sr) the isomer is $1/2^-$ of the $\nu p_{1/2}$ configuration.

The positive parity assignment for the ^{79m}Zn isomer is deduced from the large, negative magnetic moment measured in the Zn experiment (μ = -1.0180(12) μ_{N} [12]). This is consistent with the interpretation that the state is a $2h$-$1p$ neutron excitation across the N=50 shell gap with the un-paired neutron in the $\nu 3s_{1/2}$ orbital. The large positive isomer shift is an indication of an increased deformation for the isomer. From Tables 6.1 and 6.2 it is seen that the β_2 deformations for the ^{78,79,80}Zn ground states are 0.16, 0.14 and 0.16 respectively. The larger rms radius of the $^{79\text{m}}$Zn isomer corresponds to an increased deformation of ~ 0.22. This result provides the first evidence for shape coexistence in the vicinity of doubly-magic ^{78}Zn.

6.2.4 The Ni Isotopes

Due to its closed proton shell at Z=28 there is much theoretical interest in the nickel charge radii. Figure 6.4 shows a clear indication of a shell effect at the suggested subshell N=40. The result is consistent with the higher energy of first 2^+ state [52] and lower $B(E2)$ [53]. As discussed earlier, the N=40 subshell is preserved when the Z=28 closed shell reduces the proton-neutron correlations. The effect of reduced proton-neutron correlations can also be seen in the odd-even staggering shown in Figure 6.9. Compared to the Zn isotopes, the odd-even staggering of Ni isotopes is more 'regular' although the average values are similar. The effect of the proton occupation number on charge radii and odd-even staggering is expected but not yet testable since the Monte Carlo Shell Model calculation employed for the Zn isotopes is still in process.

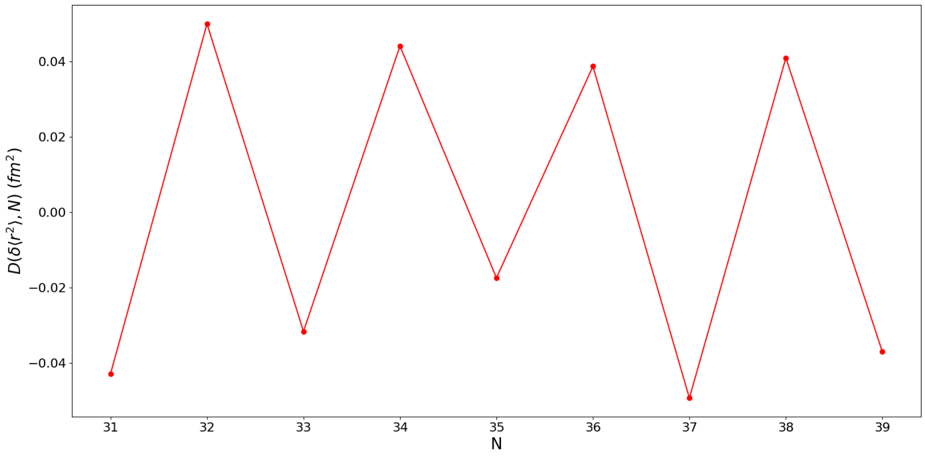

FIGURE 6.9: Demonstration of odd-even staggering along Ni isotopic chain using $D(\delta\langle r^2\rangle, N)$ calculated from Equation 6.5.

These charge radii of Ni isotopes are also critical to test theoretical calculations of nuclear charge radii. As an example of empirical formulae, Wang and Li [54] introduced a description combining the deformations and shell corrections of nuclei obtained from the Weizsäker-Skyme mass model. It generated a good overall prediction of the trend of the charge radii of stable Ni isotopes. As to the *ab initio* methods, there are at least seven sets of recent predictions, as yet unpublished and not presented here. Examples of the methods used are coupled-cluster [55], in-medium similarity renormalization group [56], Gorkov-Green functions [57]. Some only consider the even isotopes, so there is sometimes no attempt to describe the odd-even staggering. The predictions are widely spread about the experimental results by up to $\pm 0.2\ fm^2$ for ^{66}Ni when using ^{60}Ni as the reference. The data from this thesis is essential in guiding this theoretical effort.

6.2.5 Future Work

The paper discussing the mean square radii of Zn isotopes is in preparation. Collinear laser spectroscopy measurement on germanium (Z=32) isotopes were performed in the past year (attended by the author). The analysis will provide more information on the evolution of the N=40 subshell.

It may be possible to correlate nuclear ground-state observables such as the rms charge radius with other properties of nuclear matter. For example in [54] it is shown that if the slope parameter of the nuclear symmetry energy is plotted against the rms charge radii differences between the mirror pair ^{30}S -^{30}Si for 62 different Skyrme forces there is a strong correlation. Thus if the radii difference is known, it can fix the value of the slope parameter within certain limits. Similar correlations have been reported [58] between the electric dipole polarizability α_D and the proton radius of ^{48}Ca. Work is underway to use the charge radii difference between a pair of Ni isotopes measured in this work to constrain the value of the electric dipole polarizability.

Appendix A

droplet model

Here is the python code used for droplet model calculation:

```
import numpy as np
def Droplet_Model(Z, A, b2):

N = A - Z
I = (N-Z)/A
b4 = 0
A2 = np.sqrt(5/(4*np.pi))*b2
A4 = np.sqrt(9/(4*np.pi))*b4
Bs = 1 + (2/5.)*A2**2 - (4/105.)*A2**3 - (66/175.)*A2**4 - (4/35.)*A2**2*A4+A4**2
# ratio of surface area of a deformed nucleus to that of a sphere with equal volume
Bc = 1 - (1/5.)*A2**2 - (4/105.)*A2**3 + (51/245.)*A2**4 - (6/35.)*A2**2*A4-(5/27.)*A4**2     # analogous term for Coulomb energy
Bv = 1 - (1/5.)*A2**2 - (2/105.)*A2**3 - (253/1225.)*A2**4 - (4/105.)*A2**4*A4 + (4/9.)*A4**2     # associated with variations in Coulomb potential over surface when a nucleus is deformed
b = 0.99     # nuclear diffuseness
r0 = 1.145     # nuclear radius constant
```

```
J = 29.5      # symmetry energy coefficient
Q = 45.      # effective surface stiffness
K = 240.      # compressibility coefficient
L = -5.      # density symmetry coefficient
a2 = 18.      # surface energy coefficient
e = 1.199985      # electron charge in unit of MeV*fm
c1 = .7322      # Coulomb energy coefficient
delta_avg = (I+(3/16.)*(c1/Q)*Z*A**(-2/3.)*Bv)/(1+(9/4.)*(J/Q)*A**(-1/3.)*Bs)
# neutron proton asymmetry
epsilon_avg = (-2*a2*A**(-1/3.)*Bs + L*delta_avg**2 + c1*Z**2*A**(-4/3.)*Bc)/K
#deviation of density
R = r0*A**(1/3.)*(1+epsilon_avg)      # average radius of nuclear matter
t = (2/3.)*R*(I-delta_avg)/Bs)      # thickness of nuclear surface
Rn = R + Z*t/A      # average radius of neutrons
Rz = R - N*t/A      # average radius of protons
C_prime = (1/2.)*(9/(2.*K)+1/(4.*J))*(Z*e**2/Rz)
r2_u = (3/5.)*Rz**2*(1+A2**2+(10/21.)*A2**3-(27/35.)*A2**4+(10/7.)*A2**2*A4+(5/9.)*A4**2)
# contribution from the size of the uniform distribution and its shape
r2_r = (12/175.)*C_prime*(Rz**2)*(1+(14/5.)*A2**2+(28/15.)*A2**3-(29/5.)*A2**4+(116/15.)*A2*
# contribution from the redistribution, and its shape dependence
r2_d = 3*b**2      # diffuseness
r2 = r2_u + r2_r + r2_d      # mean square charge radius
Qu_2 = 6/5.*Z*Rz**2*(A2 + 4/7.*A2**2-1/7.*A2**3-94/231.*A2**4+8/7.*A2*A4+72/77.*A2**2*A4
Qr_2 = 48/175.*C_prime*Z*Rz**2*(A2 + 6/7.*A2**2-4/5.*A2**3-1984/1155.*A2**4+50/21.*A2*A4+
Q_2 = (Qu_2+Qr_2)/100      # intrinsic quadrupole moment
DM = {’r2’:r2, ’Q_2’:Q_2}
return DM
```

Bibliography

[1] A. Michelson. Philosophical Magazine, 34 (1892) 280–299. URL `https://www.tandfonline.com/doi/abs/10.1080/14786449208620318`.

[2] W. Pauli. Naturwissenschaften, 12 (1924) 741.

[3] H. Schüler. Zeitschrift für Physik, 70 (1931) 1.

[4] A. Russell and R. Rossi. Proceedings of the Royal Society A, 87 (1912) 478.

[5] N. Bohr. Philosophical Magazine, 26 (1913) 1.

[6] L. Aronberg. Astrophysical Journal, 47 (1918) 96–102.

[7] J. Rosenthal and G. Breit. Physical Review Journals, 41 (1932) 459. URL `https://journals.aps.org/pr/abstract/10.1103/PhysRev.41.459`.

[8] P. Campbell, I. D. Moore, and M. R. Pearson. Progress in Particle and Nuclear Physics, 86 (2016) 127–180. URL `https://www.sciencedirect.com/science/article/pii/S0146641015000915`.

[9] J. Billowes and P. Campbell. Journal of Physics G: Nuclear and Particle Physics, 21 (1995) 707–739. URL `http://iopscience.iop.org/article/10.1088/0954-3899/21/6/003`.

[10] C. Wraith, *et al.* Physics Letters B, 771 (2017) 385–391. URL `https://www.sciencedirect.com/science/article/pii/S0370269317304483`.

[11] X. F. Yang, *et al.* Physical Review C, 97 (2018) 044324. URL `https://journals.aps.org/prc/abstract/10.1103/PhysRevC.97.044324`.

[12] X. F. Yang, *et al.* Physical Review Letters, 116 (2016) 219901. URL `https://journals.aps.org/prl/abstract/10.1103/PhysRevLett.116.182502`.

[13] G. Fricke and K. Heilig. *Nuclear Charge Radii*, (Springer-Verlag Berlin Heidelberg2004). URL `https://www.springer.com/gb/book/9783540428299`.

[14] G. Drake. *Handbook of Atomic Molecules and Optical Physics*, (Springer New York2006).

[15] W. D. Myers. Atomic Data and Nuclear Data Tables, 17 (1976) 411–417. URL `https://www.sciencedirect.com/science/article/pii/0092640X76900309`.

[16] N. Bendali, *et al.* Journal of Physics B: Atomic and Molecular Physics, 19 (1986) 233–238. URL `http://iopscience.iop.org/article/10.1088/0022-3700/19/2/012`.

[17] M. G. Mayer. Physical Review Journals, 75 (1949) 1969. URL `https://journals.aps.org/pr/abstract/10.1103/PhysRev.75.1969`.

[18] O. Haxel, J. H. D. Jensen, and H. E. Suess. Physical Review Journals, 75 (1949) 1766. URL `https://journals.aps.org/pr/abstract/10.1103/PhysRev.75.1766.2`.

[19] E. Caurier, *et al.* Reviews of Modern Physics, 77 (2005) 427. URL `https://journals.aps.org/rmp/abstract/10.1103/RevModPhys.77.427`.

[20] H. L. Ravn and B. W. Allardyce. In: *Treatise on Heavy-Ion Science*, edited by D. A. Bromley, volume 8: Nuclei Far From Stability, chapter 5, pp. 363–439, (Plenum Press1989).

[21] U. Köster, *et al.* AIP Conference Proceedings, 798 (2005) 315. URL `https://doi.org/10.1063/1.2137262`.

[22] E. Mané, *et al.* The European Physical Journal A, 42 (2009) 503–507. URL `https://link.springer.com/article/10.1140%2Fepja%2Fi2009-10828-0`.

[23] T. J. Procter. Ph.D. thesis, University of Manchester (2013).

[24] Sirah Lasertechnik, Heinrich-Hertz-Straße 11, 41516 Grevenbroich, Germany. *Matisse User's Guide*, 2nd edition.

[25] D. W. Preston. American Journal of Physics, 64 (1996) 1432–1436.

[26] D. C. Morton. the Astrophysical Journal Supplement Series, 149 (2003) 205–238. URL `http://iopscience.iop.org/article/10.1086/377639/pdf`.

[27] *NIST Atomic Spectra Database Levels.* `https://physics.nist.gov/PhysRefData/ASD/levels_form.html`. Accessed:2018-05-30.

[28] A. Lurio. Physical Review, 126 (1962) 1768. URL `https://journals.aps.org/pr/abstract/10.1103/PhysRev.126.1768`.

[29] N. Frömmgen. The European Physical Journal D, 69 (2015) 164. URL `https://epjd.epj.org/articles/epjd/abs/2015/06/d150219/d150219.html`.

[30] A. Vernon. private communication, paper may be published in 2019.

[31] M. Wang, *et al.* Chinese Physics C, 36 (2012) 1603. URL `http://iopscience.iop.org/article/10.1088/1674-1137/36/12/002/pdf`.

[32] *IAEA online nuclear chart.* `https://www-nds.iaea.org/relnsd/vcharthtml/VChartHTML.html`. Accessed:2018-05-30.

[33] *NNDC online nuclear chart.* `https://www.nndc.bnl.gov/chart/`. Accessed:2018-05-30.

[34] C. J. Foot, *et al.* Proceedings of the Royal Society of London. Series A, Mathematical and Physical Sciences, 354 (1982) 205–216. URL `https://www.jstor.org/stable/2397439?seq=1#page_scan_tab_contents`.

[35] L. Filippin, *et al.* Physical Review A, 96 (2017) 042502.

[36] U. Koester. Ph.D. thesis, Technische Universität München (2000).

[37] N. J. Stone. Atomic Data and Nuclear Data Tables, 90 (2005) 75–176. URL `https://www.sciencedirect.com/science/article/pii/S0092640X05000239`.

[38] W. N. Lennard, *et al.* Nuclear Instruments and Methods, 110 (1973) 385–390. URL `https://www.sciencedirect.com/science/article/pii/0029554X73907167`.

[39] W. J. Childs and L. S. Goodman. Physical Review, 170 (1968) 136. URL `https://journals.aps.org/pr/issues/170/1`.

[40] C. A. Ryder, *et al.* Spectrochimica Acta Part B, 113 (2015) 16–21. URL `https://ac.els-cdn.com/S0584854715001962/1-s2.0-S0584854715001962-main.pdf?_tid=b0c020f6-671e-444c-9252-07eee272079b&acdnat=1531075418_f45e639735d37954f32cecbd067025f6`.

[41] M. L. Bissell, *et al.* Physical Review C, 93 (2016) 064318. URL `https://journals.aps.org/prc/pdf/10.1103/PhysRevC.93.064318`.

[42] T. J. Procter, *et al.* Physical Review C, 86 (2012) 034329. URL `https://journals.aps.org/prc/abstract/10.1103/PhysRevC.86.034329`.

[43] G. J. Farooq-Smith, *et al.* Physical Review C, 96 (2017) 044324. URL `https://journals.aps.org/prc/abstract/10.1103/PhysRevC.96.044324`.

[44] D. Berdichevsky and F. Tondeur. Zeltschrift für Physik A-Atoms and Nuclei, 322 (1985) 141–147. URL `https://link.springer.com/article/10.1007/BF01412027`.

[45] C. Thibault, *et al.* Nuclear Physics A, 367 (1981) 1–12. URL `https://www.sciencedirect.com/science/article/abs/pii/0375947481902748`.

[46] P. Lievens, *et al.* Europhysics Letters, 33 (1996) 11. URL `http://iopscience.iop.org/article/10.1209/epl/i1996-00296-0/pdf`.

[47] B. Pritychenko, *et al.* Atomic Data and Nuclear Data Tables, 107 (2015) 1–139. URL `https://www.sciencedirect.com/science/article/pii/S0092640X15000406`.

[48] W. D. Myers and K. Schmidt. Nuclear Physics, A410 (1983) 61–73. URL `https://www.sciencedirect.com/science/article/abs/pii/0375947483904013`.

[49] R. P. de Groote, *et al.* Physical Review C, 96 (2017) 041302(R).

[50] K. M. Lynch, *et al.* Physical Review C, 97 (2018) 024309. URL `https://journals.aps.org/prc/pdf/10.1103/PhysRevC.97.024309`.

[51] R. Orlandi, *et al.* Physics Letters B, 740 (2015) 298–302.

[52] R. Broda, *et al.* Physical Review Letters, 74 (1995) 868–871. URL `https://journals.aps.org/prl/abstract/10.1103/PhysRevLett.74.868`.

[53] O. Sorlin, *et al.* Physical Review Letters, 88 (2002) 092501. URL `https://journals.aps.org/prl/abstract/10.1103/PhysRevLett.88.092501`.

[54] N. Wang and T. Li. Physical Review C, 88 (2013) 011301. URL `https://journals.aps.org/prc/abstract/10.1103/PhysRevC.88.011301`.

[55] G. Hagen, G. Jansen, and T. Papenbrock. Physical Review Letters, 117 (2016) 172501. URL `https://journals.aps.org/prl/abstract/10.1103/PhysRevLett.117.172501`.

[56] S. Stroberg, *et al.* Physical Reveiw Letter, 118 (2017) 032502.

[57] V. Lapoux, *et al.* Physical Review Letters, 117 (2016) 052501. URL `https://journals.aps.org/prl/abstract/10.1103/PhysRevLett.117.052501`.

[58] G. Hagen, *et al.* Nature Physics, 12 (2016) 186–190. URL `https://www.nature.com/articles/nphys3529`.